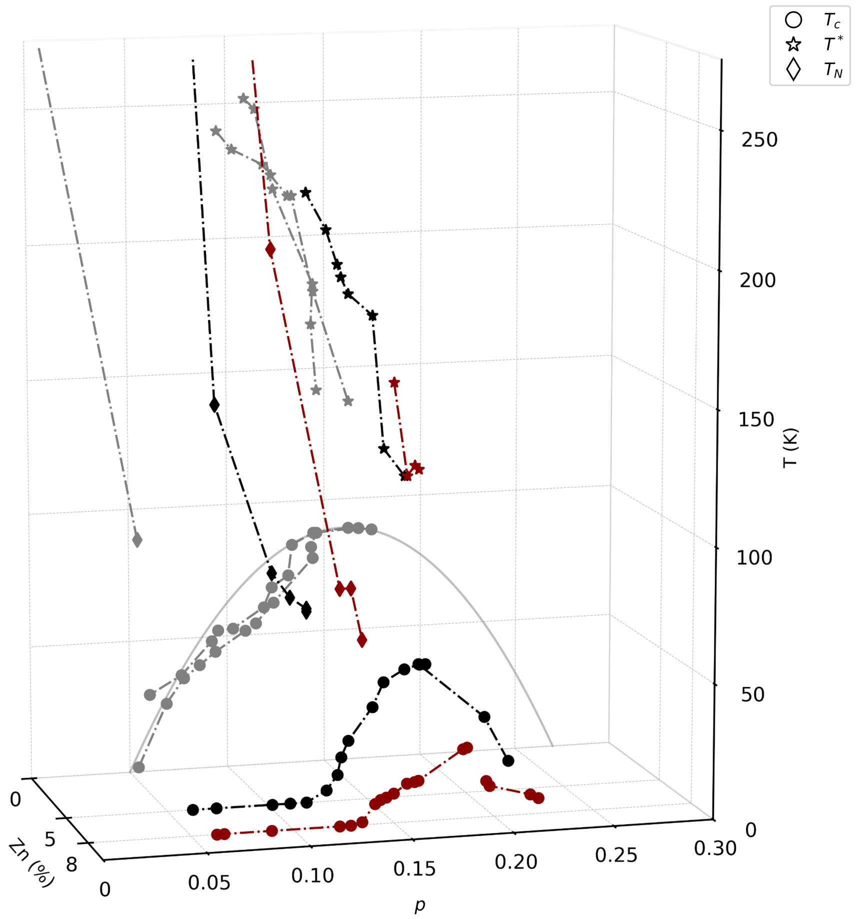

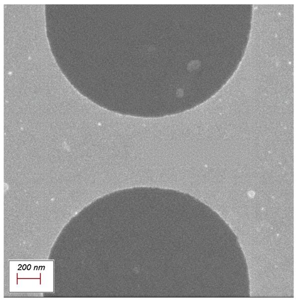

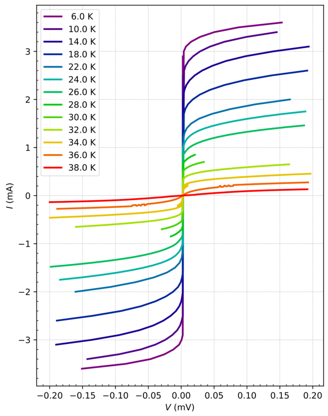

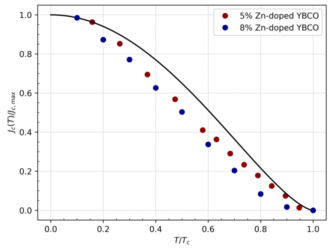

Impact of Ionic Doping on the Normal and Superconducting Properties of YBCO Thin Films and Nanowires

ANGELO BALISTRERI

Department of Microtechnology and Nanoscience
Chalmers University of Technology
Göteborg, Sweden 2025
www.chalmers.se

Master's thesis

Impact of Ionic Doping on the Normal and Superconducting Properties of YBCO Thin Films and Nanowires

ANGELO BALISTRERI

CHALMERS
UNIVERSITY OF TECHNOLOGY

Department of Microtechnology and Nanoscience
Division of Quantum Device Physics
Quantum Materials and Nanodevices (QManD)
Chalmers University of Technology
Göteborg, Sweden 2025

Impact of Ionic Doping on the Normal and Superconducting Properties of YBCO Thin Films and Nanowires

ANGELO BALISTRERI
Göteborg, Sweden 2025

Supervisor: Riccardo Arpaia, Ca' Foscari University of Venice
Examiner: Floriana Lombardi, Department of Microtechnology and Nanoscience, Chalmers University of Technology

Master's Thesis 2025
Department of Microtechnology and Nanoscience
Division of Quantum Device Physics
Quantum Materials and Nanodevices (QManD)
Chalmers University of Technology
SE-412 96 Göteborg
Telephone +46 31 772 1000

Cover: 3D visualization of the Zn-doped YBCO phase diagram (see Section 4.4) and transport characterization of Zn-doped YBCO nanowires, fabricated for the first time ever in this work (see Chapter 5).

Typeset in LaTeX
Printed by Chalmers Reproservice
Göteborg, Sweden 2025

Impact of Ionic Doping on the Normal and Superconducting Properties of YBCO Thin Films and Nanowires

ANGELO BALISTRERI
Department of Microtechnology and Nanoscience
Chalmers University of Technology, 2025

Abstract

Despite almost 40 years of intense research, high-temperature superconductivity in cuprates remains one of the most intriguing unsolved problems in condensed matter physics. The phase diagram of these materials, which describes how their properties vary with temperature and doping, is extremely complex: even the normal state above the superconducting critical temperature is characterized by multiple regions and symmetry-breaking orders associated with charge, magnetic, lattice, and orbital excitations. The interplay and competition among these orders, which may be at the origin of the pairing mechanism, are still far from being fully understood.

In this thesis, to shed light on these phenomena and gain a clearer picture of normal-state orders and of their competition with superconductivity, we focus on $YBa_2Cu_3O_{7-\delta}$ (YBCO), where doping is controlled by oxygen content, and we introduce a small fraction of Zn atoms substituting Cu. This chemical substitution modifies the CuO_2 planes, which constitute the core of both the superconducting and normal-state properties of this family of materials. In particular, I optimized the growth of Zn-doped YBCO thin films on STO substrates via pulsed laser deposition. The partial substitution of Cu with non-magnetic Zn atoms effectively suppresses superconductivity, revealing the underlying normal-state properties hidden beneath the superconducting dome.

To explore different regions of the phase diagram and understand the effect of Zn, films were grown across a range of oxygen dopings, from underdoped to strongly overdoped regimes, and for two different Zn concentrations. The structure, morphology, and transport properties of these films were characterized: these measurements allowed me to precisely determine the doping and build the complete phase diagrams for both Zn levels. Our results reveal a clear suppression of Tc, an expansion of the insulating region, and a relative invariance of the pseudogap temperature. Finally, the films were patterned into Hall bars and nanowires to investigate transport properties via current-voltage characterization and transport measurements down to the nanoscale, providing information about material homogeneity at the nanodomain level.

This work contributes to the broader effort of disentangling the mechanisms behind unconventional superconductivity by accessing the normal state through chemical doping. Moreover, it establishes a new material platform that paves the way for future investigations in both transport and spectroscopic experiments.

Keywords: YBCO Thin Films, Zn-doped, Phase diagram, Normal state, Nanowires.

A Ercole 🐾

List of symbols and abbreviations

List of symbols

$a,\ b,\ c$	YBCO crystallographic lattice parameters
$a_{s,c}$	Substrate and film in-plane lattice parameters
A_w	Nanowire cross-sectional area, $A_w = w \cdot t$
d	Target-to-substrate distance
$d_{hk\ell}$	Interplanar spacing for Miller indices (h, k, ℓ)
Δ	Superconducting energy gap
ΔT_c	Superconducting transition width
δ	Oxygen deficiency in $YBa_2Cu_3O_{7-\delta}$
δ_m	Film/substrate lattice mismatch, $\delta_m = (a_s - a_c)/a_s$
e^*	Effective charge of superconducting carriers
E	Laser fluence
ϵ	Energy barrier for vortex crossing
f	Laser repetition rate
$h,\ k,\ \ell$	Miller indices
H_{c2}	Upper critical magnetic field
I_c	Critical current
J_c	Critical current density
J_s	Supercurrent density
κ	Ginzburg–Landau parameter, $\kappa = \lambda_L/\xi$
l	Nanowire length
λ	X-ray wavelength
λ_L	London penetration depth
λ_0	Zero-temperature London penetration depth
m^*	Effective mass of superconducting carriers

μ_0	Vacuum permeability
n_s	Superconducting carrier density
N	Number of laser pulses
p	Hole concentration per planar Cu atom
p_{opt}	Optimal hole doping
P_{ann}	Annealing pressure
P_{base}	Base pressure
P_{dep}	Deposition pressure
Φ_0	Magnetic flux quantum, $\Phi_0 = h/2e$
Ψ	Superconducting order parameter
R_N	Normal-state resistance
$R_\square$	Sheet resistance
R_v	Resistance contribution from thermally activated vortex entry
ρ_{ab}	In-plane resistivity
t	Film thickness
t_{eff}	Effective thickness
T_{ann}	Annealing temperature
T_c	Superconducting critical temperature
$T_{c,0}$	Zero-resistance critical temperature
T_c^{max}	Maximum critical temperature (at optimal doping)
T_{coh}	Coherence temperature
T_{dep}	Deposition temperature
T_N	Néel temperature
T^*	Pseudogap temperature
w	Nanowire width
w_{eff}	Effective nanowire width
x	Zn substitution fraction
ξ	Coherence length
ξ_0	zero-temperature coherence length
y	Ca substitution fraction

List of abbreviations

AF	Antiferromagnetic
AFM	Atomic force microscopy
ARPES	Angle-resolved photoemission spectroscopy
BCS	Bardeen–Cooper–Schrieffer theory
CaYBCO	$Y_{1-y}Ca_yBa_2Cu_3O_{7-\delta}$ (Ca-doped YBCO)
CDW	Charge density wave
EBL	Electron-beam lithography
FWHM	Full width at half maximum
GL	Ginzburg–Landau theory
HTS	High-temperature superconductor
IBE	Ion-beam etching
IVC	Current–voltage characteristics
LN_2	Liquid nitrogen
NMR	Nuclear magnetic resonance
NS	Normal state
PLD	Pulsed laser deposition
PPMS	Physical property measurement system
RIE	Reactive ion etching
RIXS	Resonant inelastic X-ray scattering
SC	Superconducting/superconductivity
SDW	Spin density wave
SEM	Scanning electron microscopy
SIMS	Secondary-ion mass spectrometry
STM	Scanning tunneling microscopy
STO	$SrTiO_3$ strontium titanate
XRD	X-ray diffraction
YBCO	$YBa_2Cu_3O_{7-\delta}$
Zn-YBCO	$YBa_2(Cu_{1-x}Zn_x)_3O_{7-\delta}$ (Zn-doped YBCO)

Contents

Introduction

The main focus of this thesis is a systematic study of zinc-doped $YBa_2Cu_3O_{7-\delta}$ (Zn-YBCO) as a function of both oxygen doping and Zn concentration, investigating this material in thin-film form as well as in nanodevices.

$YBa_2Cu_3O_{7-\delta}$ (YBCO), discovered in 1986, was the first superconductor with a critical temperature above 77 K, the boiling point of liquid nitrogen. Its discovery paved the way to a new field in condensed matter physics called High critical Temperature Superconductivity (HTS) which is still an active and evolving field. The discovery of this class of materials was so fundamental that it led to the Nobel prize award in 1987. In the following years, several other materials were discovered that exhibited the same behavior as YBCO. These materials have as common factor the presence of copper oxide planes in the lattice, and as a result, they form the class of HTS called cuprates. The Bardeen–Cooper–Schrieffer (BCS) theory, which is the most successful theory in the field of superconductivity, fails to describe superconductivity above 30 K; therefore, is not able to describe these kind of superconductors.

Despite almost four decades of intense research in the field, a microscopic theory for the description of HTS is still missing. The perovskite-layered structure, together with a very sensitive dependence in oxygen doping and a strong electron-electron correlation, make this task difficult. The complexity of HTS arises from the interplay of multiple competing orders that coexist and interact in a rich and intricate phase diagram. The direct study of superconductivity has led to a qualitative understanding of HTS, but a complete theory remains elusive. In the last two decades, the focus has shifted to the non-superconducting normal state, which hosts several symmetry-breaking orders, some of them directly competing with superconductivity. This competition makes it challenging to determine how these orders intrinsically behave across a broad temperature range. By suppressing superconductivity, this rivalry is eliminated, enabling the observation of normal-state properties over a wider temperature range. Therefore, investigating the normal state has become a key strategy for uncovering the origin of high-temperature superconductivity.

Thus, the idea of this thesis is to simplify this complex system and observe how the other phases evolve when superconductivity is suppressed. This approach will reveal the behavior of the normal state in the region of the phase diagram where is usually hidden by the superconducting dome, giving clues about the origin of HTS. The material under investigation is YBCO which is still the most studied compound in the cuprate family.

How is it possible to suppress superconductivity and uncover the dome? One approach is to apply a magnetic field higher than the critical one. However, such fields exceed 100 T, are only available in specialized facilities, and pose technical challenges. A more viable path is chemical substitution. Via the introduction of non-magnetic impurities in the lattice, such as zinc, it is possible to disrupt the cooper pairs, suppress the superconducting transition, and progressively uncover the underlying NS.

In the '90s several studies addressed Zn-doped YBCO but only a minority focused on the normal state, and none of them produced a systematic map of the entire phase diagram. Over the last decade, the Quantum Device Physics group at Chalmers has been at the forefront of YBCO thin-film development. Their dedicated optimization efforts, spanning systematic variations in thickness, doping, and strain, have resulted in systems recognized as state-of-the-art. So, the goal of this work is to revisit this problem with a modern and comprehensive approach.

The thesis is structured as follows. In Chapter 1, after a brief historical overview of superconductivity, we introduce YBCO and its key superconducting properties. In Chapter 2 we then present the growth of high-quality Zn-doped YBCO thin films and their structural and transport characterization, which are the basis for the construction of the phase diagram discussed in Chapter 4. After this fundamental step, we further study the system by the fabrication of Zn-YBCO based nanowires (Chapter 3) and by its characterization (Chapter 5).

1

Background

In this chapter, the reader is first introduced to conventional superconductivity through a historical overview of the key discoveries in the field, and then to unconventional superconductivity, with a focus on high-temperature superconductors (HTS). We then present the structure and superconducting properties of YBCO and finally the chemical doping and the realization of Zn-doped YBCO.

1.1 Historic review of superconductivity

The root of superconductivity can be found in the late nineteenth century, as experimentalists began to push measurements toward lower temperatures - thanks to the liquefaction of nitrogen, hydrogen and helium - two opposing views emerged regard the behavior of the electrical conduction in metals:

1. Perfect insulator (Lord Kelvin) [1]
   "[...]The first thing that we remark is that every solid would, at zero of absolute temperature (that is to say all its atoms and electrions at rest), be a perfect insulator of electricity[...]"

2. Perfect conductor (James Dewar and J.A.Fleming) [2]
   "These observations are specially interesting as giving additional proof that in the case of a metal of know purity the variation of resistivity, as the metal is continuously cooled, is such as to indicate that it would in all probability vanish at the absolute zero of temperature"

In 1911 H. Kamerlingh Onnes measured the resistance of mercury and observed a sudden, discontinuous drop to an undetectable level at 4.20 K within the experimental resolution: "[...] at very low temperature such as could be obtained by helium evaporating under reduced pressure the resistance would, within the limits of experimental accuracy, become zero.” [3] The very first superconductive transition was observed! This is the first distinctive property of superconductivity: the perfect conductor.

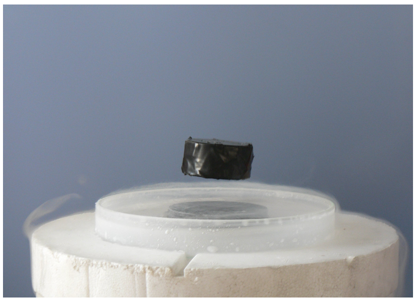

Figure 1.1: HTS, floating above a magnet due to the Meissner effect.

Fast forward to 1933: Meissner and Ochsenfeld discover that a material in the superconductive state, expels from the bulk the magnetic flux [4]. This effect is called “Meissner effect” and this property is known as the perfect diamagnetism. These two distinctive properties together completely define a superconductor. In 1935 Fritz and Heinz London developed a phenomenological model [5], derived from the classical electromagnetism, which is the simplest meaningful description of superconducting phenomena, relating the superconducting current to the electromagnetic fields:

$$\frac{\partial \vec{J_s}}{\partial t} = \frac{n_s e^{*2}}{m^*}\vec{E} \tag{1.1}$$

$$\vec{\nabla} \times \vec{J_s} = -\frac{n_s e^{*2}}{m^*}\vec{B} \tag{1.2}$$

$\vec{J_s}$ is the superconducting current density, n_s m^* and e^* are respectively the density, effective mass and effective electric charge of the superconducting electrons while $\vec{E}$ and $\vec{B}$ are respectively the electric and magnetic fields within the superconductor. Equation (1.1) describes the perfect conductor: since $\vec{J_s}$ is directly dependent on $\vec{v_s}$ (the speed of superconducting electrons), the electric field accelerates them indefinitely. Looking closely at the second London equation (Eq. 1.2), by combining it with the curl of Ampere’s law it is possible to write the Helmholtz equation for the magnetic field which holds in the bulk of the material and describes the Meissner effect:

$$\nabla^2 \vec{B} = \frac{1}{{\lambda_L}^2}\vec{B} \qquad \lambda_L \equiv \sqrt{\frac{m^*}{\mu_0 n_s e^{*2}}} \tag{1.3}$$

μ_0 is the vacuum permeability. This differential equation tells us that the magnetic field is expelled from the bulk of the superconductor thanks to a screening current that flows over a length λ_L from the edge of the material. λ_L is called the London penetration depth and is the characteristic length scale over which a field penetrates the superconductor.

We have to wait until 1950 to see superconductivity related to quantum mechanics for the first time. Vitaly Ginzburg and Lev Landau develop a phenomenological theory based on the theory of second-order phase transition made up previously by Landau himself [6]. To do so, they assume that the order parameter has to be a complex number (i.e. wave function-like) of the form:

$$\Psi(\vec{r}) = |\Psi(\vec{r})| e^{i\theta(\vec{r})} \tag{1.4}$$

which is then related to the density of superconducting electrons by:

$$n_s(\vec{r}) = |\Psi(\vec{r})|^2 \tag{1.5}$$

Since the superconducting phase is the one ordered, the order parameter Ψ is non-zero below the critical temperature T_c while it is zero in the state of thermodynamic equilibrium. Looking at the quantum-mechanical nature of the order parameter, the symmetry-breaking associated with superconductivity is the breaking of $U(1)$ phase symmetry of quantum mechanics. Following the theory of second-order phase transition, the Ginzburg-Landau (GL) theory holds at a temperature close to T_c and the order parameter Ψ has to be small and slowing varying with $\vec{r}$. The free energy of a superconductive system reads as follow[1]:

$$F = F_N + \alpha|\Psi|^2 + \frac{\beta}{2}|\Psi|^4 + \frac{1}{2m^*}\left|\left(-i\hbar\vec{\nabla} - e^*\vec{A}\right)\Psi\right|^2 + \frac{B^2}{2\mu_0} \tag{1.6}$$

where F_N is the energy of the normal state, $\hbar$ is the reduced Planck's constant, $\vec{A}$ is the vector potential of the field and α and β are respectively the first and the second derivative of F with respect of $|\Psi|^2$. From here, by taking the variation both in the order parameter and in the field, one can retrieve the GL equation:

$$\left[\alpha + \beta|\Psi|^2 + \frac{1}{2m^*}\left(-i\hbar\vec{\nabla} - e^*\vec{A}\right)^2\right]\Psi = 0 \tag{1.7}$$

$$\vec{J}_s = \frac{\hbar e^*}{2im^*}(\Psi^*\vec{\nabla}\Psi - \Psi\vec{\nabla}\Psi^*) - \frac{e^{*2}}{m^*}\vec{A}|\Psi|^2 \tag{1.8}$$

These equations are valid under the assumption of two boundary conditions:

$$\hat{n}_\perp \cdot \left(-i\hbar\vec{\nabla} - e^*\vec{A}\right)\Psi = 0 \tag{1.9}$$

$$\hat{n}_\perp \times \vec{B} = 0 \tag{1.10}$$

---

[1] The dependence on the space coordinates $\vec{r}$ in the order parameter is removed for simplicity.

which ensure that the component of the current perpendicular to the surface and the component of the magnetic field parallel to the surface vanishes. The GL-theory predicts and describes a number of phenomena:

(i) In addition to the London penetration depth another characteristic length scale emerges from the theory, ξ the coherence length:

$$\xi \equiv \sqrt{-\frac{\hbar^2}{4m^*\alpha}} \tag{1.11}$$

ξ represents the distance over which $\Psi(\vec{r})$ exponentially decays.

(ii) Flux quantization: the flux enclosed by a path going around a hole in a superconductor is quantized in units of $\Phi_0 \equiv h/e^*$ called flux quantum

(iii) The distinction between type I and type II superconductor. Combining the two characteristic length in the so-called Ginzburg-Landau parameter κ, defined as $\kappa \equiv \lambda_L/\xi$, we have:

- Type I ($\kappa < 1/\sqrt{2}$): complete Meissner expulsion
- Type II ($\kappa > 1/\sqrt{2}$): magnetic field is allowed to partially penetrate in the bulk of the material through quantized flux lines Φ_0 (called vortices) leading to a mixed state, the Abrikosov lattice [7].

Still in 1950, as the GL theory was developed, Emanuel Maxwell observed experimentally the so called "Isotope effect" of Mercury: the critical temperature is a function of the isotopic mass [8]. This suggests that the microscopic origin of superconductivity must be related to the electron-phonon coupling.

We have to wait seven more years to finally have the first microscopic theory of superconductivity. In 1957 Bardeen, Cooper and Schriffer (BCS) proposed that under a certain temperature two electrons close to the Fermi surface, with opposite spin and momentum could overcome the Coulomb repulsion due to a weak attraction mediated by the ions lattice through the electron-phonon coupling [9]. The two electrons, by means of the interaction, form a singlet spin pair, called Cooper pair. Following the BCS theory, Cooper pairs form a condensate by fixing the phase, building a coherent superposition of states with different number of Cooper pairs. The ground state reads[2]:

$$|\Psi_{BCS}\rangle = \prod_{\mathbf{k}} \left(u_{\mathbf{k}} + v_{\mathbf{k}} \hat{c}^{\dagger}_{\mathbf{k}\uparrow} \hat{c}^{\dagger}_{-\mathbf{k}\downarrow} \right) |0\rangle \tag{1.12}$$

here $v_{\mathbf{k}}$ and $u_{\mathbf{k}}$ are the probability amplitudes for the momentum state $\mathbf{k}$ to be occupied or unoccupied, respectively, by a Cooper pair formed by two electrons with opposite momenta and spins; $\hat{c}^{\dagger}_{\mathbf{k}\uparrow}$ and $\hat{c}^{\dagger}_{-\mathbf{k}\downarrow}$ are the creation operators for the Cooper pair's electrons. The appearance of this state spontaneously breaks the $U(1)$ gauge symmetry of quantum mechanics as hypothesised in the GL theory. In quantum mechanics for every symmetry-breaking mechanism a gap must be opened. Indeed, this is one of the greatest results of BCS theory: Δ is the energy gap in the excitation spectrum of the superconductor and from a microscopic point of view is half of the energy needed to break a Cooper pair. This theory retrieves all the results given by the GL theory, providing a microscopic vision of all the phenomenological quantities predicted by the latter. For instance, the coherence length ξ is the length scale of the pair interaction. Another fundamental result of the theory is the prediction of the critical temperature:

$$k_B T_c = \frac{1}{2} A \Delta_0 \tag{1.13}$$

A is a dimensionless constant, Δ_0 is the energy gap at zero temperature. The maximum T_c predicted by the BCS theory is $25 - 30\,\mathrm{K}$. Equation (1.13) tell us something more: since $\Delta_0 \propto \hbar w_D$ (w_D is the Debay frequency) and $w_D \propto M^{-\frac{1}{2}}$ (M is the mass of the ions of the lattice) it follows that $M^{\frac{1}{2}} T_c \propto const.$ which is the Isotope Effect! Inspecting equation (1.12) is clear that the theory is a mean-field theory: the superposition of states is made up without any mixing of states with different momenta. Moreover, one of the key assumptions needed for the development of the theory is the week coupling limit, which reads $\Delta << \hbar w_D << E_F$. In this limit the coherence length

$$\xi = \frac{\hbar^2 k_F}{\pi m^* \Delta}$$

is large and since $n^{1/3} \propto k_F$ we have

$$n^{1/3} \xi \propto \frac{\hbar^2 k_F^2}{m^*} \frac{1}{\Delta} \propto \frac{E_F}{\Delta} >> 1$$

---

[2] for the sake of readability we switch from the usual arrow vector notation to the bold notation $\vec{k} \equiv \mathbf{k}$ for quantum mechanic's equation

The electrons density n is related to the gas parameter r_s through $r_s \propto n^{-1/3}$ so,

$$\xi >> r_s$$

This means that Cooper pairs are spatially extended and strongly overlapping. As a consequence, one electron in a Cooper pair interact with another electron far away in the crystal. This picture is only self-consistent in a weakly interacting electron system, where long-range coherence is not disrupted by strong repulsive correlations. In contrast, in strongly correlated electron systems, where short-range Coulomb repulsion is significant, this condition no longer holds: the coherence length becomes comparable to the inter-electron distance $\xi \sim r_s$ and the mean-field BCS approach becomes inadequate. Therefore, the BCS theory is not able by construction to describe system where electrons are highly correlated.

1.2 High temperature superconductors: the cuprate family

The discovery of HTS in cuprate compounds by Bednorz and Müller in 1986 revolutionized the field [10]. The existence of material with T_c above 30 K triggered a huge amount of scientific investigation. The first compound to be discovered was barium-doped lanthanum copper oxide (LBCO) with a $T_c \sim 35\,\mathrm{K}$. The same year YBCO was discovered with a $T_c \sim 92\,\mathrm{K}$ that exceeded by three times the BCS limit set at $25 - 30\,\mathrm{K}$. The rapid escalation in T_c gave rise to the so-called High-$\mathrm{T_c}$ era, in which several other cuprates with a high critical temperature were discovered (see Figure 1.2). All cuprates share a layered perovskite-based structure featuring copper oxide (CuO_2) planes separated by layers made up by a different oxide or a single atomic element. The CuO_2 planes play a central role in their electronic properties, making them a quasi-two-dimensional systems: electrical conduction is strongly confined to the CuO_2 planes, with weak interlayer coupling. Due to a poor Coulomb screening by the surroundings, electrons here are strongly correlated. Superconductivity emerges in these planes when the material, typically a Mott insulator with antiferromagnetic order, is doped with either electrons or holes. This is achieved through the substitution or insertion of ions (typically oxygen) in the layers surrounding the CuO_2 planes, which acts as a charge reservoir.

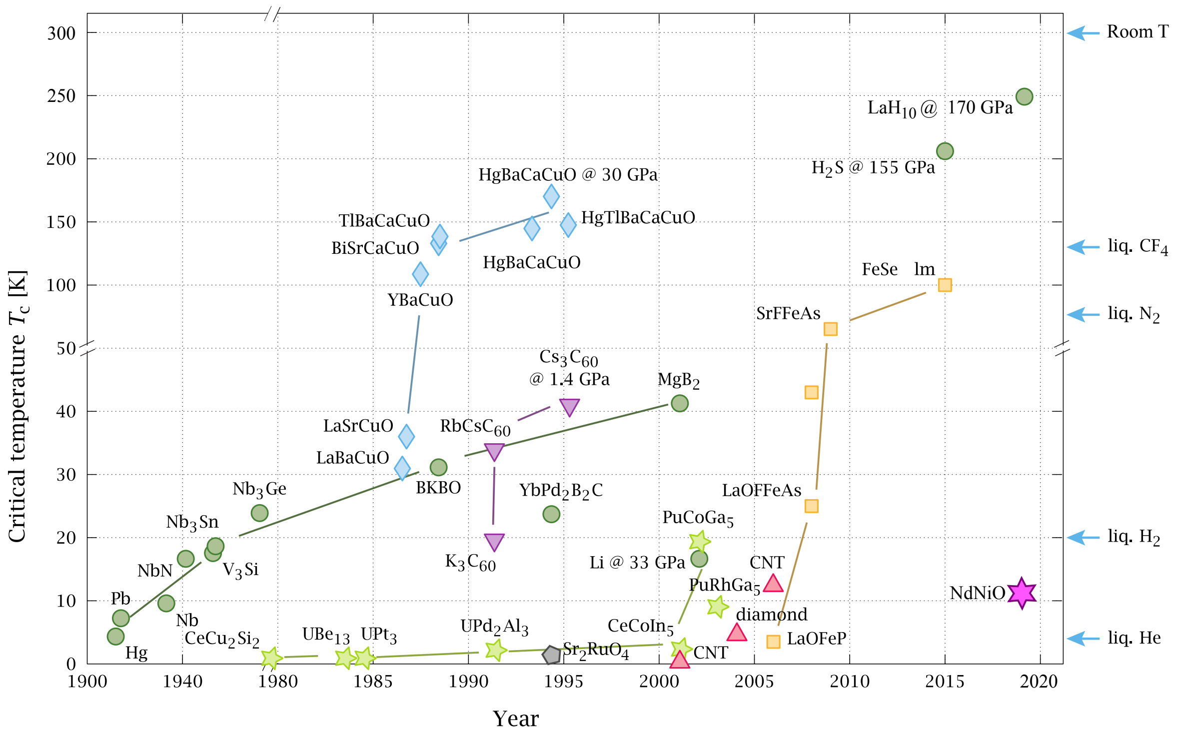

Figure 1.2: Timeline of superconductor discoveries. On the right, the liquid nitrogen temperature line separates high-temperature superconductors (HTS) from low-temperature superconductors (LTS). The graph shows cuprates as blue diamonds, iron-based superconductors as yellow squares, and other BCS superconductors, like magnesium diboride, as green circles.

1.3 YBCO: unit cell, oxygen doping and phase diagram

$YBa_2Cu_3O_{7-\delta}$ (YBCO) is one of the most studied HTS. Its crystal structure consists of three defect perovskite cells stacked on top of each other: one contains Yttrium in its center, while the other two contain Barium. The unit cell is represented in Figure 1.3. Looking from top and bottom towards the center, the unit cell consists of the following sequence of layers:

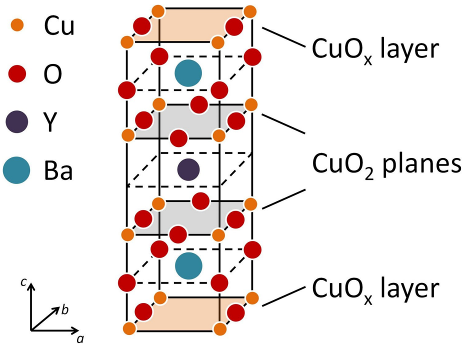

Figure 1.3: YBCO crystal structure

- One Cu – O chain layer, formed by Cu(1) atoms in square planar coordination, oriented along the crystallographic *b-axis*
- a BaO layer, which stabilize the structure
- a CuO_2 plane formed by Cu(2) atoms
- a layer formed by the Yttrium atom, which is the center of the unit cell

The Oxygen atoms in the chains play a central role in the doping which dramatically affects the superconducting properties of YBCO. Although the oxygen sites in the chains do not directly host charge carriers, they act as a charge reservoir that transfers holes to the CuO_2 planes (see Figure 1.4b) and determines the hole concentration p, defined as the number of holes per planar Cu atom.

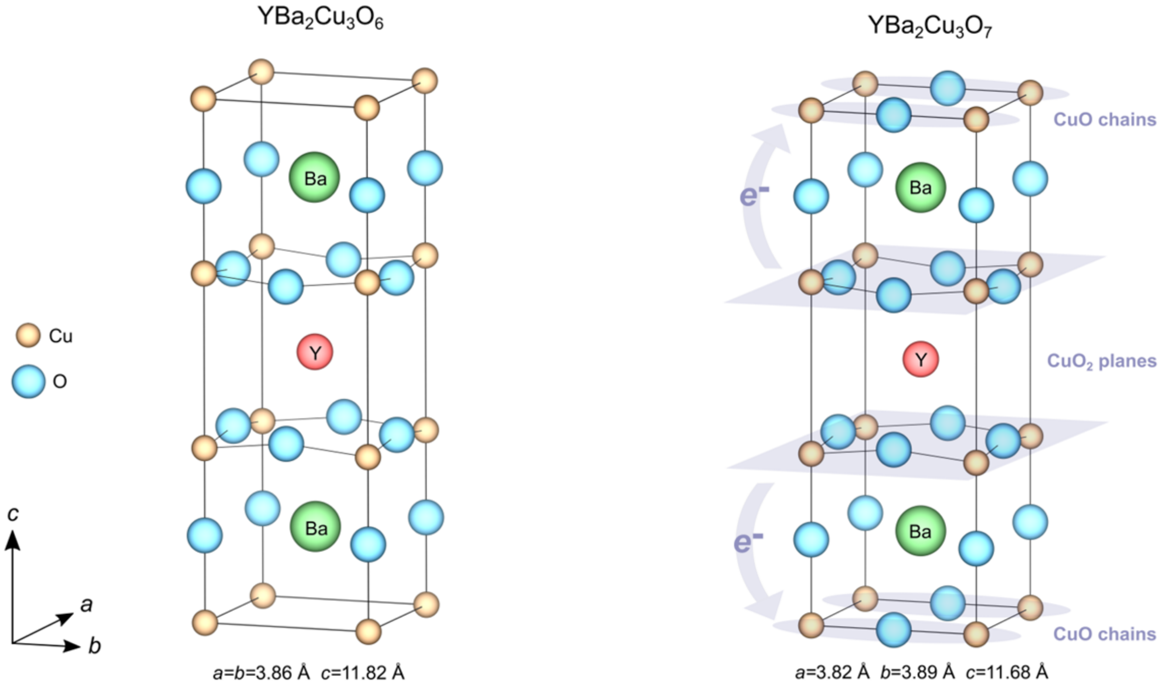

(a) (b)

Figure 1.4: YBCO crystal structure as function of δ. (a) tetragonal structure $\delta \sim 1$, (b) orthorhombic structure $\delta \sim 0$.

Fully oxygenated YBCO has $\delta \sim 0$ which corresponds to a hole concentration $p \sim 0.19$ slightly above the optimal doping (slightly overdoped). Here T_c is close to its maximum value $\sim 92\,\mathrm{K}$. The unit cell is orthorhombic with $a = 3.82\,\text{Å}$, $b = 3.89\,\text{Å}$ and $c = 11.69\,\text{Å}$ Figure 1.4b. As oxygen is removed (so δ increases) the hole concentration decreases and the material becomes underdoped ($p < 0.16$), T_c is gradually suppressed. As oxygen is further removed, δ approaches its maximum value $\delta \sim 1$ eventually turning the crystal from a superconductor into an antiferromagnetic insulator. Here $p \sim 0$ and the unit cell is tetragonal with $a = b = 3.86\,\text{Å}$ and $c = 11.82\,\text{Å}$ Figure 1.4a.

As doping is modified, the system transforms dramatically: due to strong electron-electron correlation and the non-trivial dependence on oxygen doping, superconductiv-

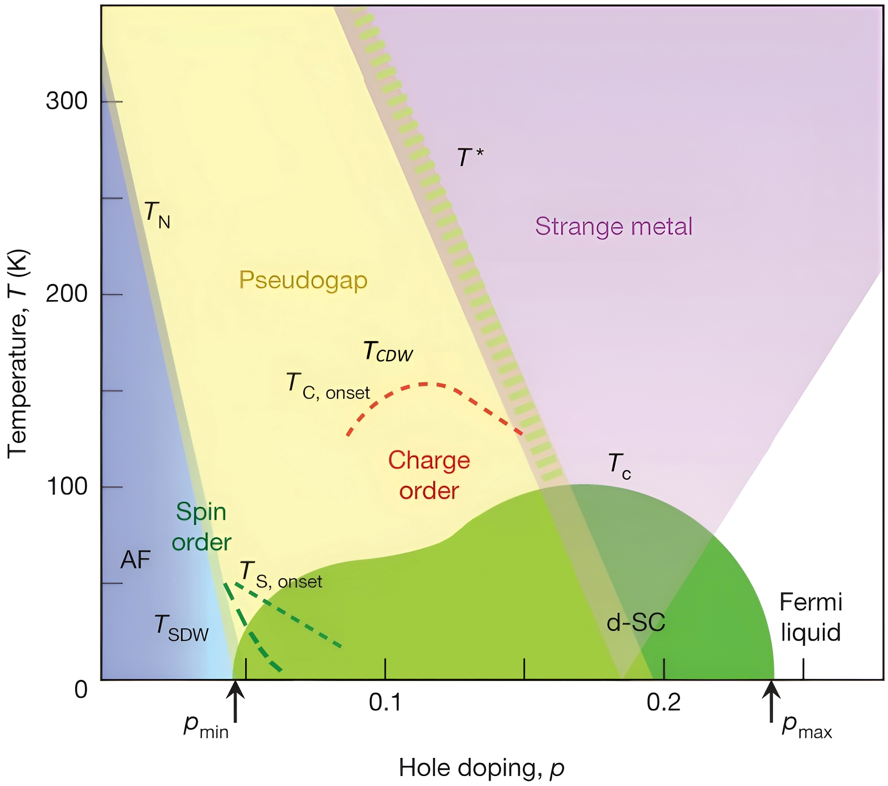

Figure 1.5: Temperature versus hole doping level for the copper oxides, indicating where various phases occur. Adapted from “Nature **518**, 179–186 (2015)” [11].

ity emerges alongside multiple other phases and orders creating an extremely rich and complex phase diagram, shown in Figure 1.5. This phase diagram is typically divided into three regions, namely the underdoped, optimally doped and overdoped regime:

- the *overdoped* region ($p > 0.16$) shows a suppression of superconductivity as hole doping increases and the normal state becomes progressively metallic. This metallic state is described by the Fermi liquid theory, where the electronic excitations at the Fermi level behaves as non-interacting quasiparticles. The strange-metal physics is specific to the CuO_2 planes. In this regime, corresponding to $\delta \approx 0$, the $Cu - O$ chains are fully oxygenated and provide an additional conduction channel parallel to that of the CuO_2 planes, at all temperatures. Their contribution, described again by the Fermi liquid theory, enhances the overall conductivity, masking the behavior of the planes.

- the *optimally doped* region ($p \approx 0.16$) is where the critical temperature reaches its maximum. The normal state exhibits non-conventional behavior, with resistivity linear in temperature. This phase is called strange metal and still has to be completely understood [12, 13, 14].

- the *underdoped* region ($p < 0.16$) is the richest part of the phase diagram. Here superconductivity is suppressed by decreasing hole concentration. The normal state is characterized by the emergence of the pseudogap phase, which persists at temperatures much greater than T_c. This electronic phase does not exhibit a true phase transition (passing through the crossover temperature T^*) but shows a partial depletion of the electronic density of states (from which its name arises). The pseudogap regime disappears moving towards optimal doping (see Figure 1.5), and its origin remains debated. In this region of the phase diagram, a landscape of intertwined orders emerges, such as charge density waves (CDW) and spin density waves (SDW), which together with the pseudogap may compete with superconductivity. CDW in particular are thought to be responsible for the suppression of superconductivity around $p = 0.125$ (the "1/8 anomaly") [15]: at this doping, the onset temperature of CDW reaches its maximum, as does the suppression of superconductivity. In the phase diagram, this strong competition manifests as a plateau in the parabolic dome.

- in the *strongly underdoped/undoped* region ($p < 0.05$), long-range antiferromagnetic order emerges. Although the system is insulating because of strong Coulomb repulsion, the electron spins remain active degrees of freedom. Through virtual hopping processes, constrained by the Pauli exclusion principle, a super-exchange interaction is generated between neighbouring spins, leading to a Néel-ordered antiferromagnetic phase.

Over the years, the phase diagram has been extensively explored through numerous experiments; nevertheless, although a qualitative understanding of the nature of superconductivity has been achieved, the full picture remains elusive. One major reason is the extreme complexity of the phase diagram: at optimal doping, the strange metal regime reaches its maximum extent (i.e., the resistivity remains linear over the broadest temperature range), while the superconductivity is also strongest (with the highest critical temperature at p_{opt}). The normal state thus appears intertwined with superconductivity, suggesting the need to decouple the two phases to study these systems in a less complex environment. The most straightforward approach would be to suppress superconductivity by applying a magnetic field above the critical field. In principle, this would suppress superconductivity while leaving the (non-magnetic) normal state intact. The issue with HTS systems is that type-II superconductors exhibit very high critical fields H_{c2}, making both transport and spectroscopy measurements extremely challenging. For example, in YBCO, $H_{c2} \approx 140\,\mathrm{T}$ at $T = 0\,\mathrm{K}$ and $p = p_{opt}$, a field strength accessible only in a few facilities worldwide, which also poses major logistical challenges. An alternative approach is chemical doping: introducing controlled defects into the crystal lattice can suppress superconductivity, either partially or completely, while leaving the normal state essentially unaffected.

1.4 Chemical doping: Zn-doped YBCO

Chemical substitution represents a powerful tool to study the interplay between superconductivity and the normal state in cuprate superconductors [16, 17]. Among the various dopants, zinc (Zn) substitution on the Cu(2) sites in the CuO_2 planes has emerged as one of the most studied and effective methods to suppress superconductivity while preserving the essential electronic structure of the host material [18, 19, 20].

Zn^{2+} ions, being isovalent with Cu^{2+}, do not alter the carrier concentration when substituted into the CuO_2 planes [18]. However, their $3d^{10}$ electronic configuration (closed shell) is in contrast with the $3d^9$ configuration of Cu^{2+} ions, which carry a spin-1/2 magnetic moment [21]. This difference makes Zn atoms act as non-magnetic impurities that locally disrupt the magnetic and electronic properties of the CuO_2 planes without changing the overall carrier concentration [17]. The effect of Zn substitution on superconductivity is dramatic: even small concentrations of Zn (typically a few percent) lead to a significant suppression of T_c [18, 16]. For instance, in $YBa_2\left(Cu_{1-x}Zn_x\right)_3O_{7-\delta}$, T_c decreases approximately linearly with Zn concentration at a rate of about $\approx 8-10\,\mathrm{K}$ per atomic percent of Zn [19, 16]. This strong suppression rate indicates that superconductivity in cuprates is particularly sensitive to disorder in the CuO_2 planes, much more so than conventional superconductors [17].

From a theoretical point of view, Zn impurities create localized states within the superconducting gap, leading to pair-breaking effects [22, 23]. Unlike magnetic impurities, which would cause spin-flip scattering and destroy Cooper pairs through the exchange interaction, non-magnetic impurities primarily affect superconductivity through potential scattering [24, 22]. This makes them ideal probes for studying the nature of the superconducting state without the additional complications introduced by magnetic interactions [17].

The local environment around Zn impurities has been extensively studied through various spectroscopic techniques. Nuclear magnetic resonance (NMR) studies reveal that Zn atoms induce significant electronic inhomogeneity in their vicinity, affecting the local density of states and magnetic properties of neighbouring Cu sites [21, 25]. This local perturbation extends over several lattice sites, creating "dead layers" around each Zn impurity, where superconductivity is locally suppressed [26, 25].

Importantly, while Zn doping effectively suppresses superconductivity, it appears to have minimal impact on other electronic phases present in the cuprate phase diagram [17, 27]. This property has made Zn-doped cuprates invaluable for disentangling the complex interplay between competing orders and superconductivity in these materials [17, 28].

However, one limitation of studying Zn-doped YBCO through oxygen content variation alone is the restricted accessible range of hole doping. As mentioned earlier, fully oxygenated YBCO ($\delta \sim 0$) corresponds to a hole concentration of $p \sim 0.19$, which is only slightly overdoped. Since Zn substitution does not alter the carrier concentration, the overdoped region of the phase diagram remains largely inaccessible through conventional oxygen doping.

To overcome this limitation and explore the overdoped regime, calcium (Ca) substitution has been employed as an additional hole-doping mechanism [29, 30]. Ca^{2+} ions can substitute for Y^{3+} ions in the yttrium sites due to their similar ionic radii, rather than the much larger Ba^{2+} sites [31, 32]. Since Ca has one less valence electron than Y, each Ca substitution effectively introduces one additional hole into the system. The compound $Y_{1-y}Ca_y\left(Cu_{1-x}Zn_x\right)_3O_{7-\delta}$ therefore allows for independent control of both the superconductivity suppression (through Zn content x) and the hole concentration (through Ca content y and oxygen stoichiometry δ) [33].

In this work, we use $YBa_2\left(Cu_{1-x}Zn_x\right)_3O_{7-\delta}$ to explore the phase diagram from $p \sim 0$ to $p \sim 0.19$ and $Y_{1-y}Ca_y\left(Cu_{1-x}Zn_x\right)_3O_{7-\delta}$ to access the overdoped regime.

2

Growth & Characterization of Zn-doped YBCO

The theoretical framework we established in the previous chapter provides the foundation for understanding superconductivity in cuprates, but transforming this knowledge into meaningful experimental insights requires something more. In order to reveal the subtle effects we seek to investigate, high-quality samples are mandatory. Creating superconducting samples suitable for fundamental research is far from trivial. As we learned, YBCO superconducting properties emerge from a delicate interplay of structural and electronic interactions that critically depend on the properly arrangement of atoms in the structure. Deviations from the ideal crystal structure can alter or suppress superconductivity making our task undoable. This sensitivity to structural details means that sample quality isn't just important: it's absolutely essential for obtaining reliable results. This chapter connects the theory with the practice, detailing how we grow and characterize zinc-doped YBCO samples with the accuracy needed for our research. The experimental activities described in this chapter were performed independently by the author; from substrate preparation to thin film deposition and the subsequent characterization measurements.

2.1 Substrate

Thin films serve as an ideal platform for exploring, enhancing, and precisely controlling the superconductive properties of a material system. The foundation of any successful thin film growth lies in choosing the right substrate. Although this might seem like a purely technical consideration, the substrate choice profoundly influences every aspect of the resulting film's properties. In a thin film, the substrate must fulfill two fundamental requirements:

- to provide the atomic template needed for the growth of the material.
- to give the mechanical support needed in the experimental setup.

In this framework, it is clear that the choice of the substrate is crucial, as strain influences the properties of the film, such as crystallographic orientation [34] and electronic structure [13, 35, 36]. Several factors must be taken into account when selecting the appropriate substrate. To minimize defects and promote epitaxial growth, a close lattice-parameter match between the substrate and the deposited film is imperative. The lattice mismatch is defined as

$$\delta^m = \frac{a_s - a_c}{a_s} \tag{2.1}$$

where a_s and a_c represent the in-plane lattice parameters of the substrate and the parental crystal of the film, respectively. The mismatch creates a strained film structure that could be tensile ($\delta^m > 0$) or compressive ($\delta^m < 0$). The effects of this strain are not uniform throughout the film. The strain effects are stronger close to the film-substrate interface and relax as the film becomes thicker, restoring their bulk-like structure.

Thermal considerations add another layer of complexity to the substrate selection. The thermal expansion coefficients of the substrate and film must be reasonably well matched to maintain control over the stresses during temperature cycling. Mismatched thermal expansion can create significant stress as samples are heated and cooled, potentially leading to cracking, delamination, or degraded superconducting properties. Think about a bimetallic strip: if the thermal expansion coefficients aren't properly matched a thin film on a substrate would experience the same kind of stresses.

In this work, we employ single-crystal (001)-oriented $SrTiO_3$ (STO) substrates. The STO crystal lattice is cubic, with lattice parameters $a = b = c = 3.905$ Å (see Figure 2.1). For c-axis oriented growth, STO offers a good lattice match with YBCO, resulting in a modest tensile strain of $\delta^m = +1.2\%$ in the tetragonal phase, $\delta^m_{avg} = +2.8\%$ in the orthorhombic. A consequence of using STO to grow YBCO is the formation of twinned films. Since STO is cubic while YBCO is orthorhombic, the in-plane anisotropy present in the crystal structure of the parent material is lost, and random exchange of a and b occurs in the film. In homogeneous twinned

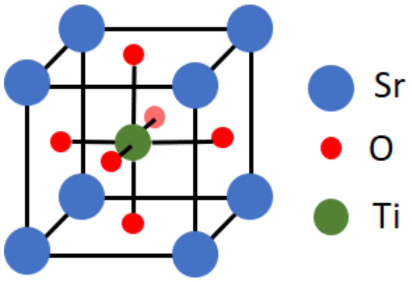

Figure 2.1: STO crystal structure, with lattice parameters $a = b = c = 3.905$ Å

films, the physical properties are the same in the two orthogonal in-plane direction, corresponding on an average value.

2.2 PLD: thin film deposition

Although selecting the right substrate provides the foundation for high-quality films, the deposition technique itself determines whether we can successfully translate our material requirements into reality. Among the various thin film growth methods available, pulsed laser deposition (PLD) stands out as particularly well-suited for complex oxides like YBCO, because of its unique ability to maintain stoichiometric transfer from target to substrate and for its flexibility. Figure 2.2a illustrates an essential diagram of a PLD system. The working principle of PLD is the following: a high-power pulsed laser is focused onto a target made of the parental material. The intense energy density at the target surface causes rapid ablation, creating the so-called "plasma plume" (see Figure 2.3), a dynamic mixture of atoms, molecules, and ions that travel towards the heated substrate facing the target. Here, the ablated material condenses on the substrate surface, forming a thin film. For each laser pulse, the material spreads across the surface and occupies vacancies in the lattice; a new layer begins only when the previous is complete; this results in epitaxial growth.

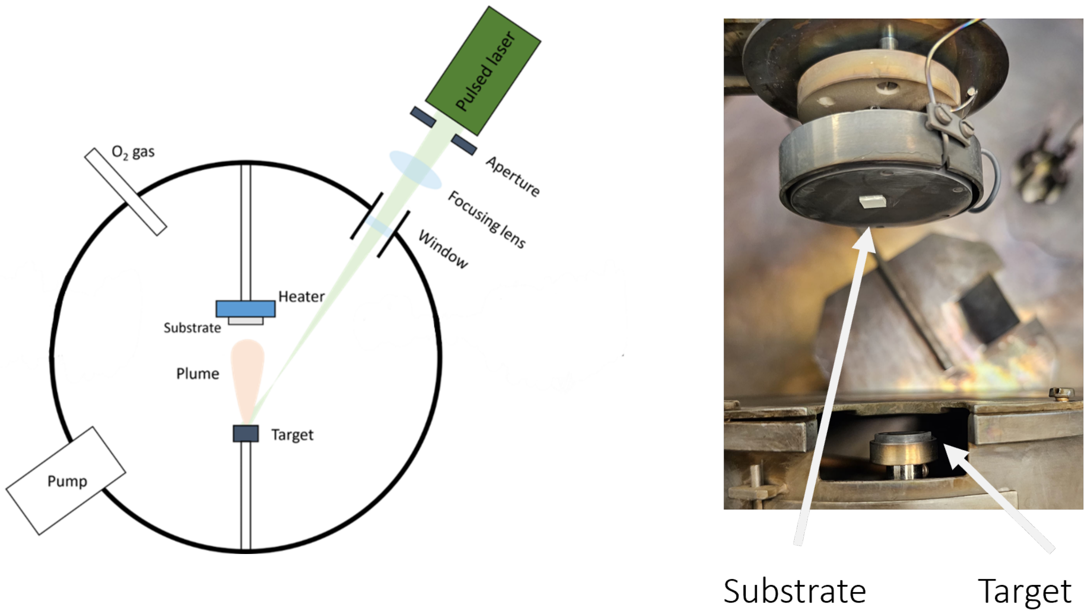

(a) (b)

Figure 2.2: PLD system. (a) display a schematic PLD diagram; (b) a picture of a real PLD chamber.

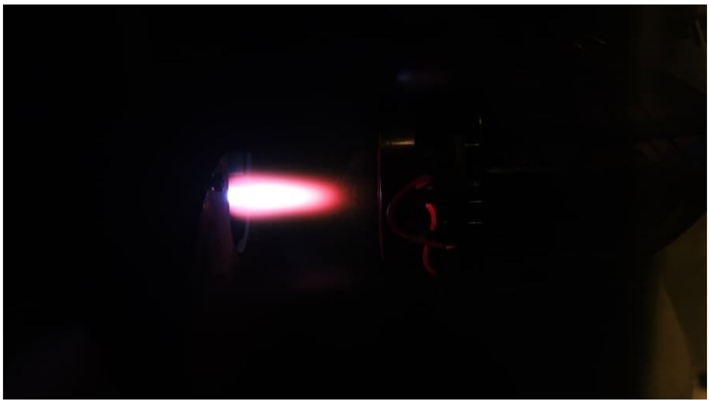

Figure 2.3: Picture of a "plasma plume" captured during a thin film deposition

However, growing YBCO presents unique challenges that go beyond simple material transfer. The most critical issue involves oxygen stoichiometry. Because of its volatility, oxygen is introduced into the chamber as a background gas to help achieve the correct stoichiometry in the film. Nevertheless, YBCO films typically grow in the tetragonal phase ($\delta > 0.6$) due to the high deposition temperature, $700 - 900\,^{\circ}\mathrm{C}$. To obtain the orthorhombic phase, the system is exposed to high oxygen pressure during cooldown: at elevated temperatures ($500 - 700\,^{\circ}\mathrm{C}$), oxygen diffuses easily into the film, filling the $\mathrm{Cu-O}$ chains and creating fully oxygenated YBCO.

For Zn-doped YBCO, the challenge of achieving the correct stoichiometry is significantly amplified. The chemical doping introduces an additional layer of complexity, making precise control over the elemental composition even more critical.

The deposition steps are as follows:

1. Substrates are carefully cleaned and checked under an optical microscope.

2. The substrate is mounted onto the heater at a distance d from the target, which has been pre-ablated previously (see Figure 2.4). To improve thermal conductivity the substrate is glued onto the heater using silver paste.

3. The deposition chamber is evacuated and pumped until reaching the base pressure P_{base}.

4. Pre-annealing occurs: the substrate is annealed at $T = T_{dep}$ (deposition temperature) under an oxygen pressure P_{dep} for the required time (see Figure 2.5)

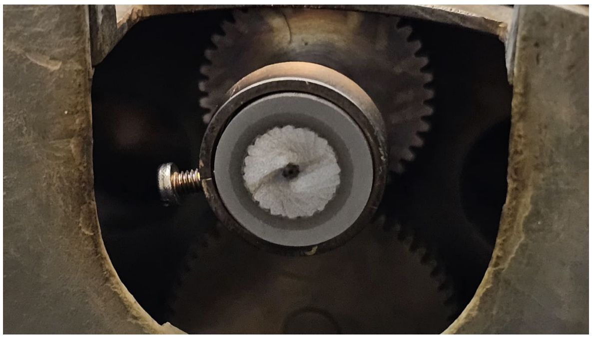

Figure 2.4: Zn-doped YBCO target pre-ablated.

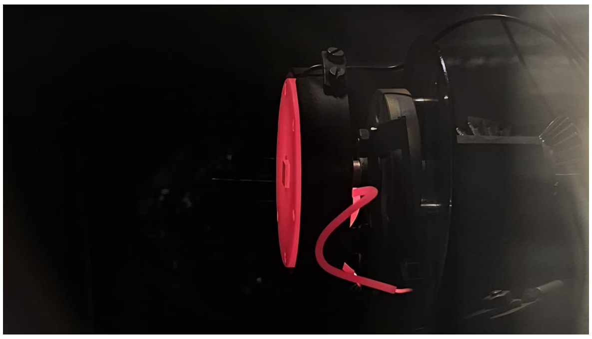

Figure 2.5: Picture of the heater at 800 °C at the end of the pre-annealing.

5. The laser ablates the target and deposition proceeds. The laser fluence E, repetition rate f, and number of pulses N, together with the background oxygen pressure P_{dep}, control the dynamics of the growth.

6. Post-annealing follows: the system is cooled down under an oxygen pressure P_{ann} close to atmospheric pressure.

Table 2.1 lists the parameters used for Zn-doped YBCO PLD deposition. The terminology here reflects the temporal sequence: *pre-annealing* refers to the substrate conditioning before growth, while *post-annealing* describes the oxygenation treatment during cooldown. More generally, “annealing” encompasses any procedure involving extended exposure to controlled temperature and oxygen pressure conditions, typically lasting several hours, designed to fine-tune the hole doping concentration. The annealing procedure and the control of the oxygen doping will be discussed in detail in Sec. 2.5. Film thickness relates directly to the number of laser pulses, with approximately 20 pulses producing 1 nm of deposited material. Consequently, the total deposition time is N/f. In this work, Zn-doped YBCO on STO is grown as c-axis oriented.

d	T_{dep}	P_{dep}	f	E	P_{ann}	cooling rate
50 mm	800 °C	0.6 mbar	6 Hz	1.2 J/cm^2	800 mbar	5 K/min

Table 2.1: Parameters used to deposit Zn-doped YBCO thin films by PLD (CALAS system).

2.3 Structural and morphologic characterization

Verifying the success of thin-film deposition requires a comprehensive analysis of both the material's crystal structure and its surface morphology. Structural characterization techniques are essential for determining key parameters such as lattice parameters and epitaxial quality. Moreover, morphological analysis provides critical insight into the surface features of the film, including its smoothness, homogeneity, and presence of defects or growth anomalies.

The structural properties were investigated by X-ray diffraction (XRD). As suggested by its name, the physics of XRD is based on the constructive interference of X-rays scattered by the periodic arrangement of atoms in the crystal. When X-rays meet the sample, waves scattered from different lattice planes interfere constructively only when the Bragg condition is satisfied:

$$n\lambda = 2d_{hk\ell}\sin\theta \tag{2.2}$$

where n is the diffraction order, λ the X-ray wavelength, $d_{hk\ell}$ the spacing between the (h, k, ℓ) lattice planes, and θ the Bragg angle. The interplanar spacing is related to the Miller indices (h, k, ℓ) and the unit cell parameters a, b, and c through:

$$\frac{1}{d_{hk\ell}^2} = \frac{h^2}{a^2} + \frac{k^2}{b^2} + \frac{\ell^2}{c^2}. \tag{2.3}$$

For c-axis oriented thin films, the most intense reflections correspond to the family of planes (00ℓ), where ℓ is an integer and $h = k = 0$. In this case the c-axis parameter is directly determined from the angular position of the Bragg peaks. Equation (2.3) with $h = k = 0$, leads to $d_{00\ell} = c/\ell$, combining this result with equation (2.2) it follows:

$$c = \ell\frac{\lambda}{2\sin\theta_\ell} \tag{2.4}$$

However, an interesting complication arises from the substrate choice: since the c-axis of STO is 3.905 Å, which is approximately one third of YBCO c-axis, we have that

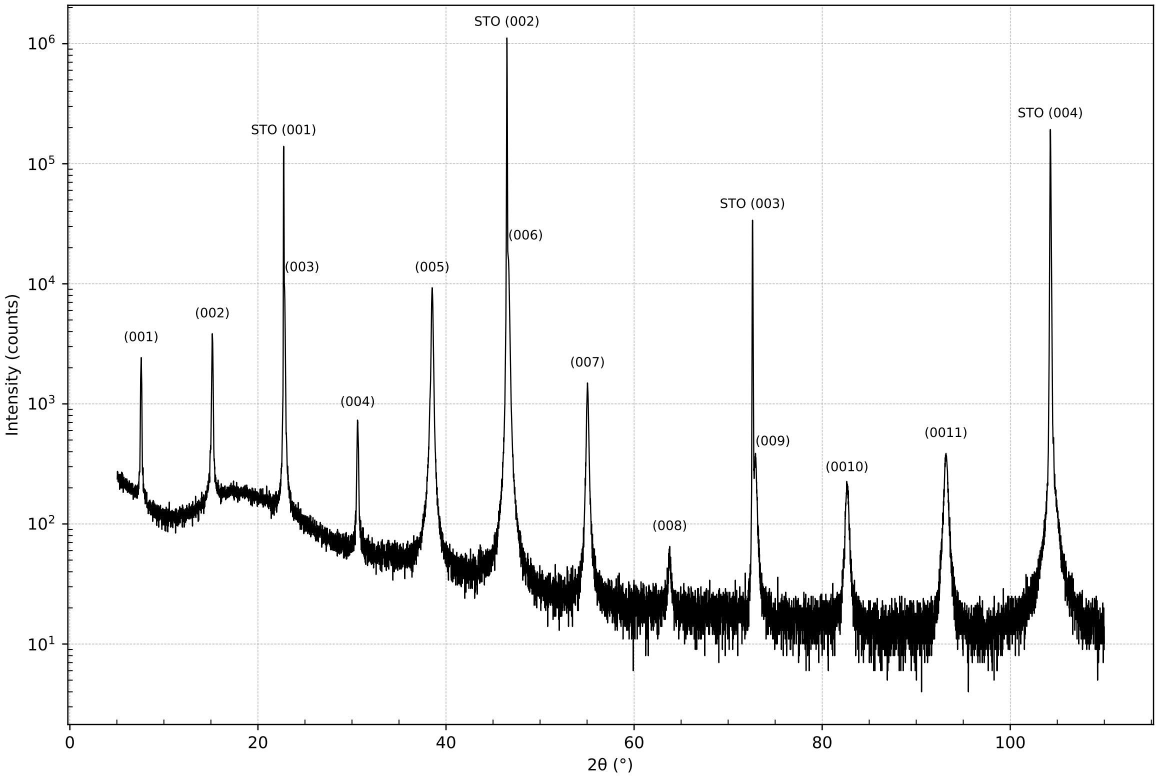

Figure 2.6: $2\theta - \omega$ scan for Zn-doped YBCO. (00ℓ) reflection of YBCO are presented together with the reflection of the substrate, STO(00ℓ).

for same angles the reflection from the film is superposed to the ones of the substrate, making this reflection almost impossible to be used. Looking again at equation (2.2) this happens for every n which is multiple of three.

In our measurements, symmetric $2\theta - \omega$ scans were performed from $\theta \sim 5°$ to $\theta \sim 120°$. Figure 2.6 shows a $2\theta - \omega$ scan of a Zn-doped YBCO thin film. The substrate reflections appear much more intense than those from the thin film. This is due to the different number of planes composing the crystal: the substrate is very thick, so the number of planes could be approximated to infinity, while the thin film typically consists of only 100 layers. This finite thickness manifests in both the peak amplitude (number of counts) and the Full Width at Half Maximum (FWHM) of the Bragg peaks; essentially representing the Fourier transform in reciprocal space. The sharp, narrow diffraction peaks we observe indicate high crystalline quality in our films. Additionally, the finite film thickness produces another distinctive feature: Laue oscillations, which appear as modulations in the intensity envelope around the Bragg peaks. These oscillations are most visible in the (001) reflection, as they become increasingly strongly suppressed at higher angles. Figure 2.7 provides a detailed view of the (001) reflection, which highlight these characteristic oscillations. Laue oscillations are directly related to the thickness of the sample, following this relation:

$$t = \frac{\lambda}{2\left(\sin\frac{\omega_n}{2} - \sin\frac{\omega_{n-1}}{2}\right)} \tag{2.5}$$

t is the thickness of the film and $\omega_n = 2\theta_n$ indicates the angle at which the maximums of the Laue oscillations occur. Therefore, we can extract the thickness of the film from the (001) reflection. Laue oscillations are very sensitive to the roughness of the film. This physical quantity is a measure of the fine-scale surface irregularities of a material, often characterized by the statistical deviation of its real profile from an ideal flat surface. Their presence serves as an indicator of surface smoothness. To determine the remaining lattice parameters, is required an asymmetric map 2θ–ω Vs ω involving the (038) and (308) reflection, which provide the strongest signal to determine a and b. Figure 2.8 shows a 2θ–ω Vs ω map of a Zn-doped YBCO thin film centered around the (038) and (308) reflections. Using again equation (2.3) and by using the c-axis parameter extracted from the symmetric scan, is possible to determine a and b:

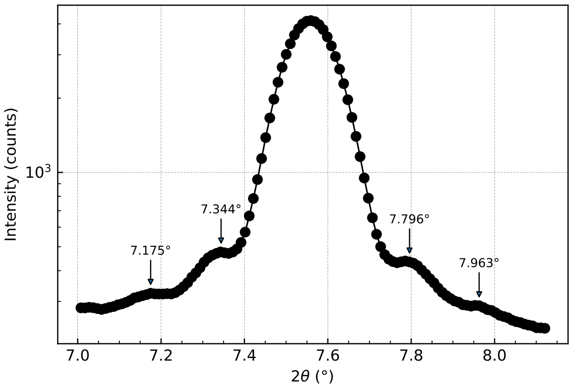

Figure 2.7: Laue oscillation around the 001 reflection.

$$a = \frac{3}{\sqrt{\frac{4\sin^2\theta_{308}}{\lambda^2} - \frac{64}{c^2}}} \qquad b = \frac{3}{\sqrt{\frac{4\sin^2\theta_{038}}{\lambda^2} - \frac{64}{c^2}}} \tag{2.6}$$

Surface Morphology of the films has been studied by Scanning Electron Microscopy (SEM) (Figure 2.9). The films are characterized by the tridimensional spiral-like growth of YBCO, which is directly related to c-axis domains. These are randomly oriented along the a and b-axis, as expected for twinned films. The surface is smooth and shows the presence of holes and some defects. The realization of high-quality thin films opens the possibility to develop nano-fabrication on Zn-doped YBCO thin films and further study the properties of the system at the nanoscale.

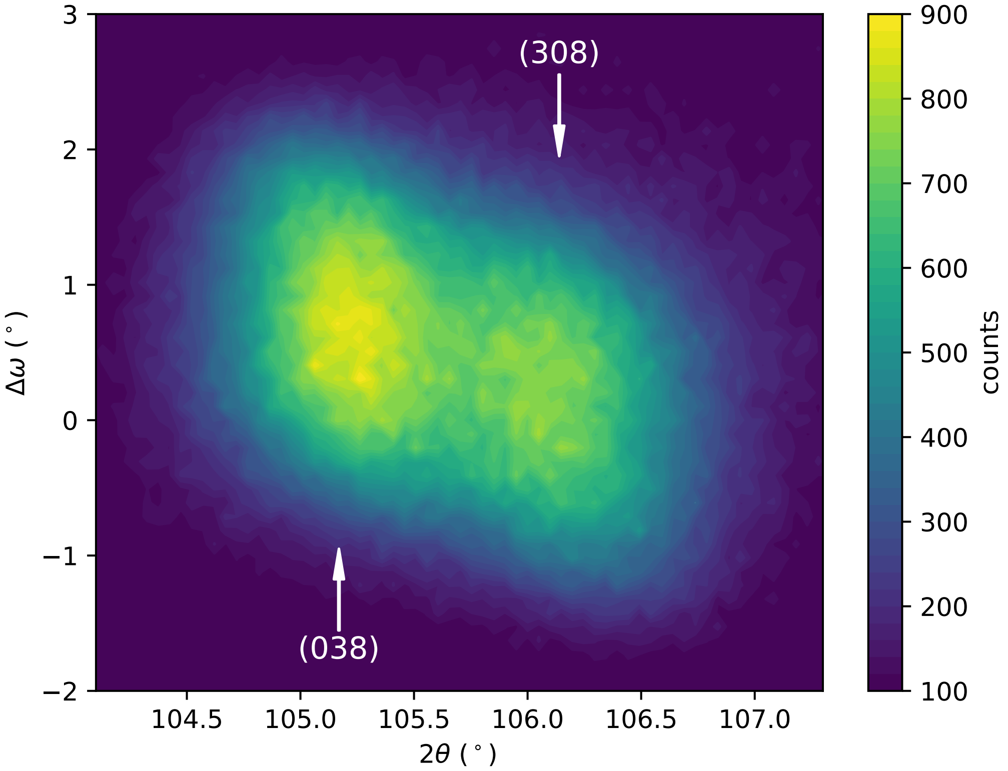

Figure 2.8: $2\theta-\omega$ Vs ω scan of (038) and (308) reflection, highlighted by the arrows.

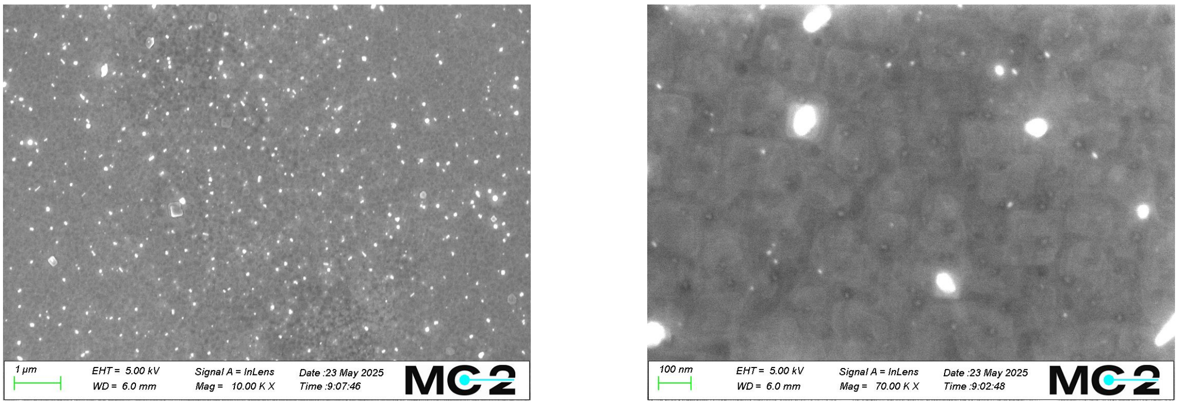

(a) (b)

Figure 2.9: SEM image of an 8% Zn-doped YBCO thin film. (a) low magnification image, showing the overall morphology. (b) High magnification image highlighting the spiral-like growth of YBCO.

2.4 Transport characterization

Transport measurements provide one of the most direct probes of the phase diagram in cuprates. The temperature dependence of the in-plane resistivity, $\rho_{ab}(T)$ (the ab subscript will be implied), responds to changes in carrier scattering, Fermi-surface reconstruction, gap openings and superconducting coherence; therefore, a careful analysis of $R(T)$ measurements could reconstruct the entire phase diagram. As presented in Chapter 1.3, each region of the phase diagram leaves its characteristic signature in the $R(T)$.

Let's examine how $\rho(T)$ evolves across different doping regimes, identifying the key temperatures that mark major crossovers and phase boundaries:

- In the *overdoped regime* ($p > 0.16$) ρ exhibits linear behavior down to a temperature known as the coherence temperature T_{coh}. Below this point, the resistivity has a quadratic behavior, $\rho(T) = a + bT^2$ characteristic of the Fermi liquid phase, with positive b. The concave upward behavior is the hallmark for the overdoped region [37]. T_{coh} is associated to the end of the strange metal and the recovery of quasiparticle picture of the excitation. In twinned films, the chains run along both in-plane directions, providing an additional metallic channel that masks the crossover of the CuO_2 planes, making the determination of T_{coh} more complicated. Figure 2.10a.

- In the *underdoped regime* ($p < 0.16$) ρ is linear down to T^*, known as the pseudogap temperature. here the resistivity is again quadratic in temperature, $\rho(T) = a + bT^2$ but b is negative. This is usually seen as a recovery of Fermi liquid transport in the underdoped region. The downward curvature of $\rho(T)$ below T^* is the hallmark for the underdoped regime. Figure 2.10c.

- In the *optimally doped regime* ($p \sim 0.16$), the linear resistivity regime extends over the widest temperature range of the entire phase diagram, persisting almost down to the superconducting transition. Here, the strange metal, the pseudogap and the superconductive phase merge at the optimal doping. T_L the temperature where the linearity is lost can be associated to T_{coh} or T^*. Distinguishing between the two becomes challenging due to the presence of superconducting fluctuations (SF) at the onset of the superconducting transition. The superconductive transition is described by T_c the maximum of the first derivative of $\rho(T)$. Figure 2.10b.

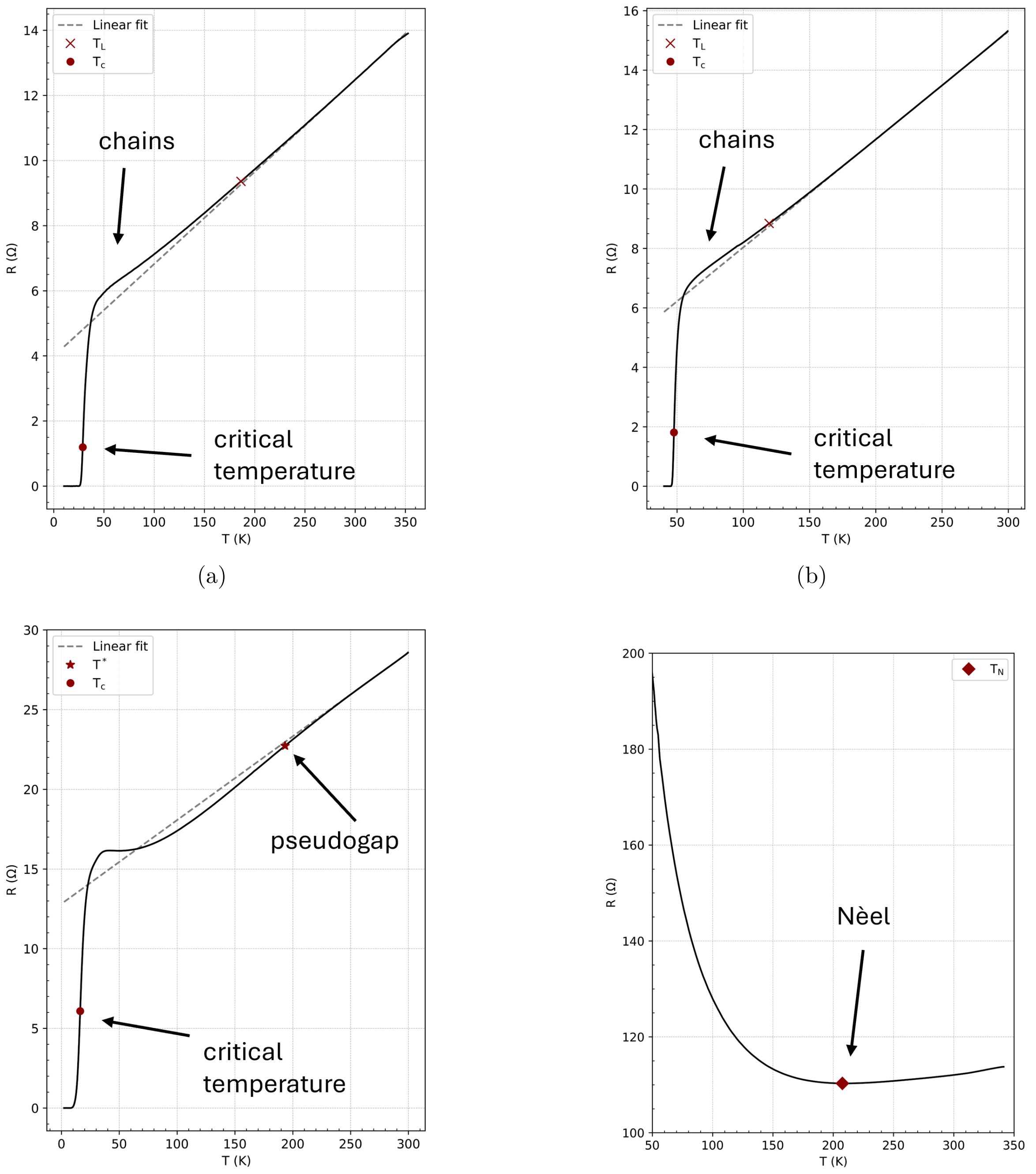

(a) (b)

(c) (d)

Figure 2.10: R(T) scan of Zn-doped YBCO for different hole doping. Panel (a) 5% Zn-doped CaYBCO, $p \approx 0.21$, Overdoped. Panel (b) 5% Zn-doped YBCO, $p \approx 0.16$, optimally doped. Panel (c) 5% Zn-doped, $p \approx 0.14$, Underdoped. Panel (d) 8% Zn-doped YBCO, $p \approx 0.09$, Strongly underdoped. In each panel are reported the different characteristic temperatures that can be extract from the R(T).

- in the *strongly underdoped regime* ($p < 0.05$) linear resistivity survives only at very high temperatures (T>300 K). Below this, the quadratic behavior emerges similar to the underdoped case, but without any superconducting transition. Instead, we observe a dramatic upturn in resistivity, leading to the antiferromagnetic insulating phase. The upturn consist in a very rapid growth that reaches values above several MΩ for $p \approx 0$. Although this phase is most definitively characterized by spectroscopic techniques, transport measurements can still identify it through the Néel temperature T_N, defined as the minimum in $\rho(T)$. Figure 2.10d.

Thin films are characterized by a Physical Property Measurement System (PPMS) which provides temperature control from 400 K and down to 2 K and magnetic field up to 14 T. The resistance of the films is measured in a Van der Pauw configuration, ensuring that we probe only the film's intrinsic properties without contributions from contact resistance or wiring.

For the reproducibility of the measure, we pattern four gold pads through cold sputtering, to ensure that the position of the bonding on the surface of the thin film is the same for all measurements, and the geometry is fixed. By measuring in two orthogonal Van der Pauw configurations, any anisotropy in the in-plane resistivity can be detected. Since YBCO grown on STO is twinned, this anisotropy should be negligible; significant deviations may indicate partial detwinning or inhomogeneity in the film.

The superconducting transition provides valuable information about film quality. The transition width, ΔT_c, is a sensitive indicator of film homogeneity: a sharp drop in resistivity over a narrow temperature interval indicates a uniform oxygen content and Zn distribution across the sample, while a broadened or multi-step transition suggests inhomogeneities, structural defects or local variations in doping concentration.

2.5 The annealing process

To systematically explore the phase diagram, we need a reliable and controlled method for adjusting the oxygen content in YBCO thin films. Ex-situ annealing in controlled atmospheres provides the standard approach for modifying δ in a reproducible way, allowing to access all the doping, from $\delta \sim 0$ to $\delta \sim 1$ [38, 39].

2.5.1 Oxygen doping

The crystal structure of YBCO consists of alternating CuO_2 planes, BaO layers, and $Cu-O$ chains along the b-axis, as discussed in Section 1.3. Oxygen atoms occupy well-defined chain sites (O(1)) and partially filled interstitial positions (O(5)), while the apical O(4) sites remain fully occupied throughout the doping range [40, 41]. The annealing process modifies δ by allowing oxygen diffusion from the external atmosphere into the $Cu - O$ chain layer, where oxygen atoms are ordered in a quasi–1D arrangement. At the microscopic level, oxygen incorporation is governed by:

- Surface exchange: oxygen molecules are dissociatively adsorbed on the crystal surface, with O^{2-} incorporation mediated by surface vacancies.

- Bulk diffusion: once incorporated, oxygen diffuses through the chain layer via thermally activated hopping between neighbouring sites, with a diffusion coefficient following an Arrhenius law:

  $$D(T) = D_0 \exp\left(-\frac{E_a}{k_B T}\right)$$

  where D_0 is the prefactor, E_a the activation energy and k_B the Boltzmann constant.

- Chain ordering: oxygen atoms preferentially occupy chain sites to minimize the total energy, leading to the formation of ordered chain segments (Ortho-I, Ortho-II, Ortho-III phases) depending on δ [42].

Oxygen stoichiometry directly determines hole doping p in the CuO_2 planes via charge transfer: each additional oxygen atom in the chains injects holes into the planes, modifying the transport and superconducting properties.

In this work, the annealing process is always done ex-situ [38, 39] due to limitations in the PLD system's oxygen flow control, which can only maintain stable and fixed pressure within a very narrow window. Like any other diffusive phenomena, the annealing process is extremely slow. The reaching of full equilibrium requires several hours at fixed and constant temperature and pressure. The annealings were all conducted at a temperature of $T_{ann} = 550\,°C$ for a duration of 10 hours, in a pressure range spanning between 6×10^{-5} mbar and 1×10^{2} mbar. Figure 2.11 shows how the critical temperature changes in function of the annealing pressure. As discussed so far, we have all the experimental setup to address an high-quality and controlled research of the phase diagram. The key information that is still missing is a way to determine the hole doping.

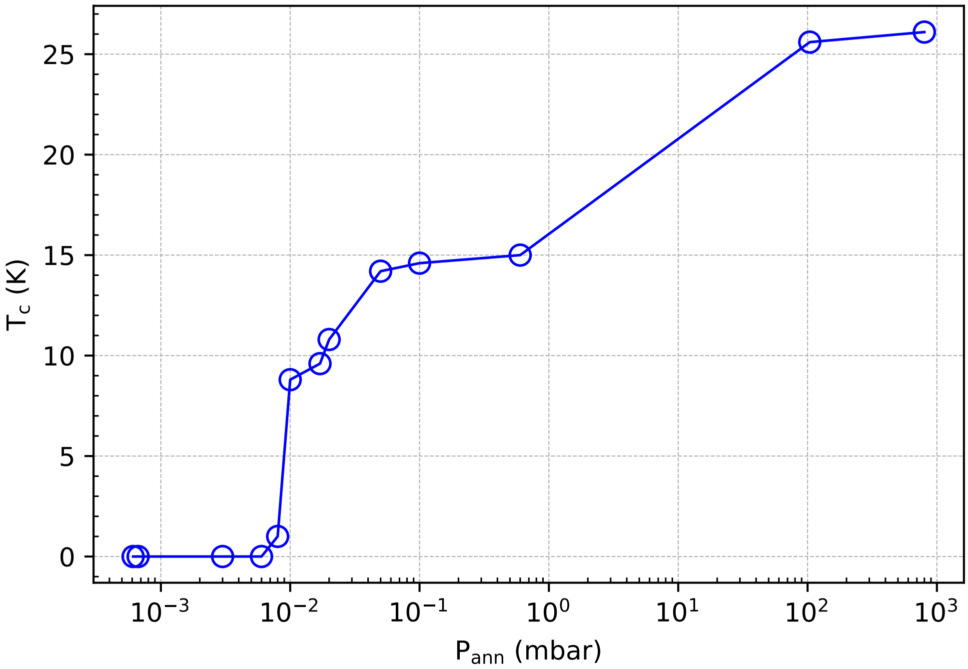

Figure 2.11: Critical temperature T_c in function of the annealing preassure P_{ann} for a 60 nm 8% Zn-doped YBCO thin film. The line is a guide to the eye.

2.5.2 Determination of the hole doping

In HTS bulk crystals, the hole doping can be calculated directly from oxygen content measured through chemical and thermo-gravimetric analyses [43]. For YBCO, because of the challenging crystal structure, this approach is challenging even for single crystals: we need to know not only the number of holes but also how these are distributed between CuO_2 planes and CO chains. For thin films, such direct chemical analysis becomes entirely impractical. The oxygen content is reflected not only in transport properties but also in the structural parameters measurable by X-ray diffraction (XRD). The *c*-axis lattice parameter decreases monotonically with increasing oxygen content [40, 41]. This contraction originates from the shortening of the Cu − O bond lengths in the apical direction due to increased hole density and stronger hybridization between the apical oxygen and the Cu in the chains. For YBCO single crystal, hole doping is usually calculated from the critical temperature T_c using the empiric relation:

$$1 - \frac{T_c}{T_c^{max}} = 82.6 \cdot (p - 0.16)^2 \tag{2.7}$$

This parabolic relation has proven reliable across numerous studies [38, 41], though it obviously cannot provide hole doping values for non-superconducting samples.

In YBCO single crystal, oxygen content δ and c-axis length have been showed to have the same functional dependence with T_c. This relation is exploited as a non-destructive method to estimate δ and, by extension, the hole doping p [41]. In epitaxial thin films, residual strain from the substrate can slightly shift the absolute c-axis value, but the relative trend with δ remains consistent with bulk crystals. Therefore, it is possible to establish a one-to-one relation between p and c.

The introduction of Zn and Ca into the lattice makes the determination of the hole doping even more difficult. For Zn-doped YBCO, since the Zn substitute for Cu in the CuO_2 planes it mainly affects the dynamics of the system and only negligibly its structural properties. Therefore, for Zn-doped YBCO, we can extract the doping from the knowledge of the c-axis. For sample with Ca doping the story is different: by substituting yttrium at the center of the structure, the force in the out-of-plane direction modify the structure at rest. Therefore, we cannot directly use the hole doping - c-axis relation. For these samples, we need to find a different experimental relation to determine the hole doping.

3

Nanofabrication of Zn-doped YBCO devices

The experimental investigation of structures at the nanoscale is essential to the study of high temperature superconductors. With *nanoscale* we refer to systems with typical dimensions on the order of nanometers to hundreds of nanometers. This length scale is fundamental in HTS material: the coherence length ξ and the London penetration depth λ_L fall within this range. It is precisely at these dimensions that several crucial physical phenomena governing superconducting behavior occur.

The answer to the question raised by nanoscale phenomena can only be obtained through the successful fabrication of nanostructures whose properties closely mirror those of their bulk counterparts. However, the realization of homogeneous nanostructures with pristine superconducting properties presents a significant challenge for HTS. These materials suffer from chemical instability, mainly due to oxygen out-diffusion, and exhibit extreme sensitivity to defects and disorder arising from their very short ξ (which is of the order of 1 nm). This issue is even more pronounced for underdoped structures, where oxygen loss can readily induce a transition from a superconducting to an insulating state.

In this chapter, we describe the process to fabricate nanowires and Hall bars from Zn-doped YBCO thin films. The experimental activities described in this chapter were performed under the supervision of a Ph.D student from the QmanD group.

3.1 The fabrication process

A widely adopted and effective approach for the fabrication of YBCO nanostructures, relies on electron-beam lithography using a carbon hard mask joint with argon ion milling. Over the past decade, our group at Chalmers has refined this technique to produce HTS nanowires with width as small as 50 nm, exhibiting record-high critical current densities approaching the theoretical depairing limit [44, 45, 46].

We present the steps of the fabrication process, which is entirely shown in Figure 3.1. For more details, in particular regarding the parameters and the chemicals used, we refer to Appendix A and to Refs. [47, 48, 49, 50].

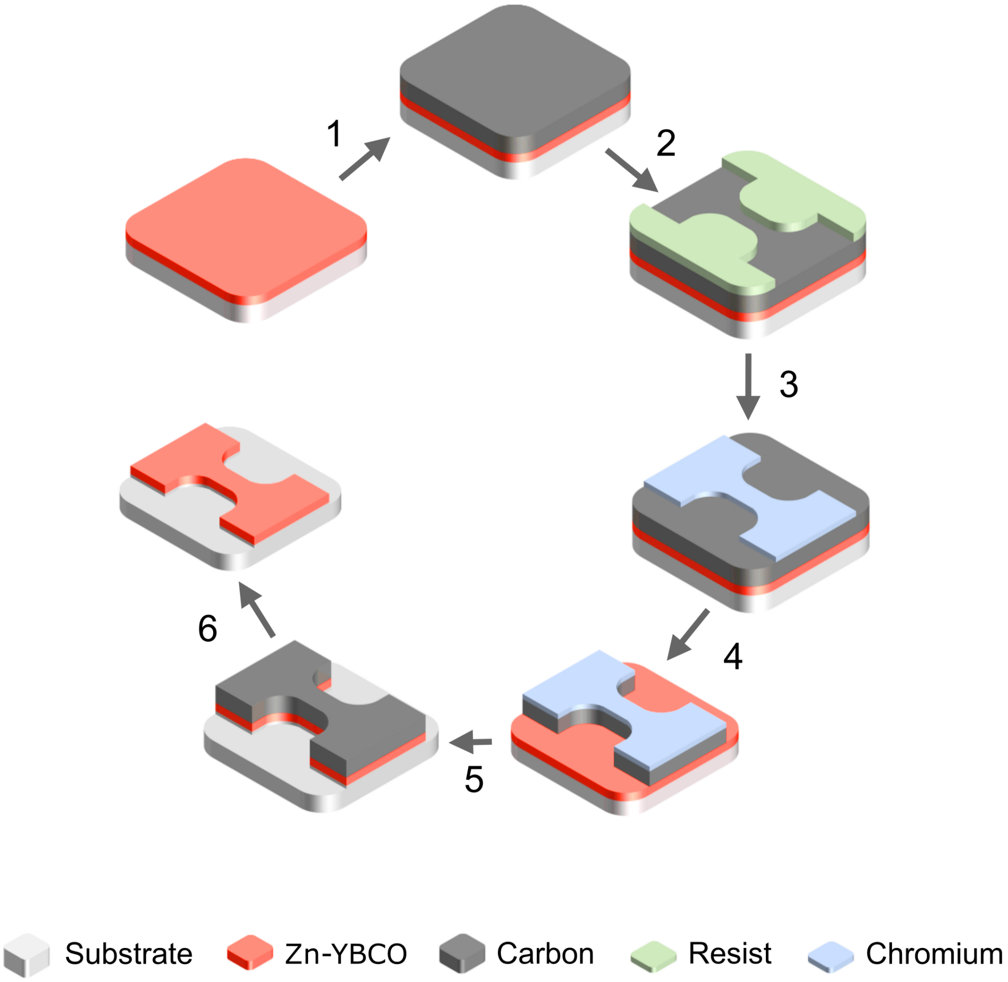

Figure 3.1: Diagram of the fabrication for Zn-doped YBCO nanowires.

The fabrication follows these steps:

0. the fabrication begins with the PLD deposition of a high-quality thin film, as described in Chapter 2. The Zn-doped YBCO thin film is 60 nm thick.

1. the Zn-doped YBCO film, soon after the deposition, is mounted in a mechanical mask and 60 nm of gold are cold sputtered ex-situ over the masked film. This step creates the gold stripes where the gold contacts will be defined in the further steps. (see Figure 3.2)

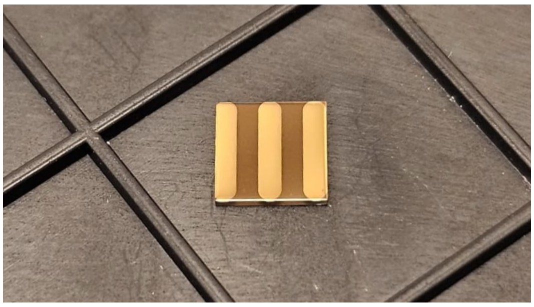

Figure 3.2: Zn-doped YBCO thin film after the gold sputtering.

2. 100 nm of carbon are deposited by PLD with an argon background environment. This layer is used as hard mask. The employment of the Carbon mask, makes for sharper, more defined walls of small structures. (Step 1 of Figure 3.1).

3. a two-layer resist is deposit by spin coating.

4. the device geometry is defined in the resist layers by Electron Beam Lithography (EBL) at 100 kV.

5. the resist is developed and the exposed areas are removed by the process. The sample is checked under optical microscope to confirm the pattern has been properly transferred to the underlying layer. (Step 2 of Figure 3.1)

6. 10 nm of chromium are evaporated on top and will act as a metal mask for the carbon.

7. the resist is lifted-off. To confirm the complete removal of the resist and to verify that the desired pattern has been successfully transferred to the underlying layer, without any cracks or other structural defects, the sample is checked under optical microscope. (Step 3 of Figure 3.1)

8. the carbon layer unprotected by the chromium is removed by Oxygen plasma Reacting Ion Etching (RIE). The sample is checked with a profiler to ensure that the RIE has etched all the material. (Step 4 of Figure 3.1)

9. Zn-YBCO, now selectively uncovered from carbon, is physically etched with Ion-Beam Etching (IBE). This process uses argon ions to etch mechanically the sample. Secondary-Ion Mass Spectrometry (SIMS) is used to check which atoms are etched throughout the process. For YBCO devices the process finishes when the barium is completely etched, therefore the signal of Ba in the SIMS goes to zero (see Figure 3.3). For IBE the etching is done very delicately (if compared to other nanofabrication recipes), using the lowest stable settings of the tool for the ion current, which directly affects the etching rate. The etching is done at an angle of 25° to minimize the re-deposition effects. The process is stopped when counts of Ba in the SIMS have gone to almost zero, meaning that the layer has been completely etched through. (Step 5 of Figure 3.1)

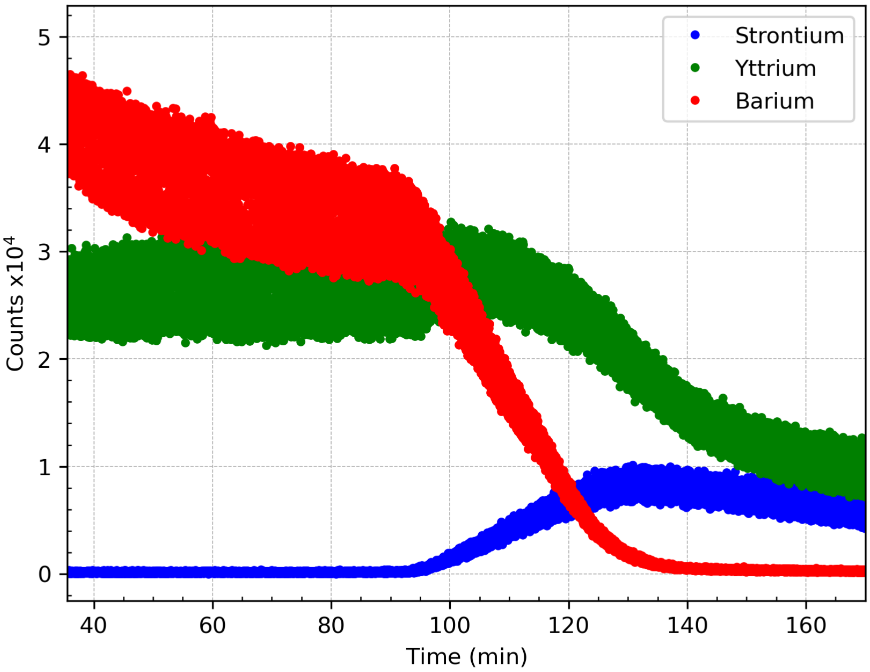

Figure 3.3: Atoms counts (see legend) Vs time during the IBE of the devices measured with the SIMS. Yttrium and Strontium are neighbour in the periodic table of elements therefore the signal is not as reliable as the one from Barium, to understand when the etching is completed. As Barium falls, Strontium rises: the ions start etching the substrate. Barium survives well above the starting point of Strontium etching: in the region where Zn-doped YBCO is covered by gold (where the contacts are located) the etching of Zn-doped YBCO is delayed because of the additional nanometers of gold that has to be etched first. Therefore, to get unshunted pads, is fundamental to wait until the Barium signal is zero.

10. after a check with the profiler, the sample undergoes again through Oxygen plasma RIE, to remove the remaining carbon, now fully uncovered from Chromium. This final step will unveil the final shape of the devices. (Step 6 of Figure 3.1)

We check one last time at the profiler the resulting step between YBCO and the substrate, as a means to verify that the fabrication process has gone correctly and all the carbon has been removed. Figure 3.4 and 3.5 shows the devices at the end of the Nanofabrication process. The most delicate part in the process is the IBE. This step (together with the others) has been engineered through the year by the group at Chalmers to ensure least amount of damage and reproducible results.

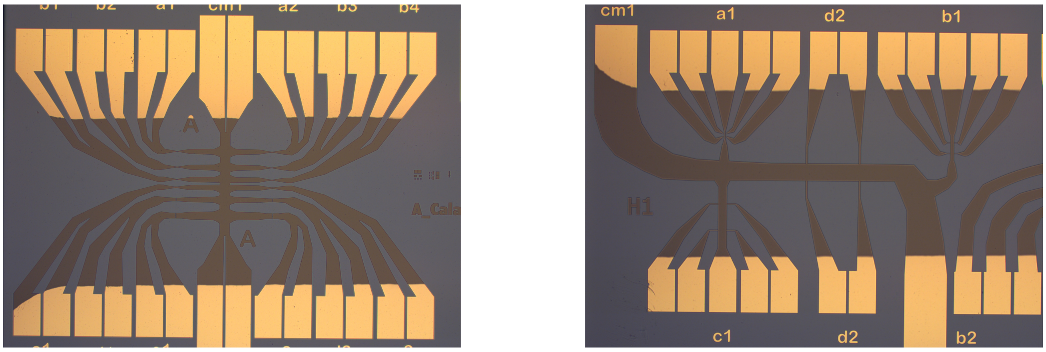

(a) (b)

Figure 3.4: Optical microscope image of two section of one of the chip fabricated. Figure (a) shows the nanowires section: the common electrode is visible in the center with multiple gold contacts enabling four-probe measurements. The individual connections for each nanowire are visible on the sides. Figure (b) shows the Hall bars section: the two common contacts, making an S-like pattern, are visible at the top left corner and near the bottom right; the current is driven through these two contacts. Additionally, for each Hall bar, four other very thin contacts, used as voltage probes, are disposed on the sides; these allow the measurement of ρ_{xx} and ρ_{xy}.

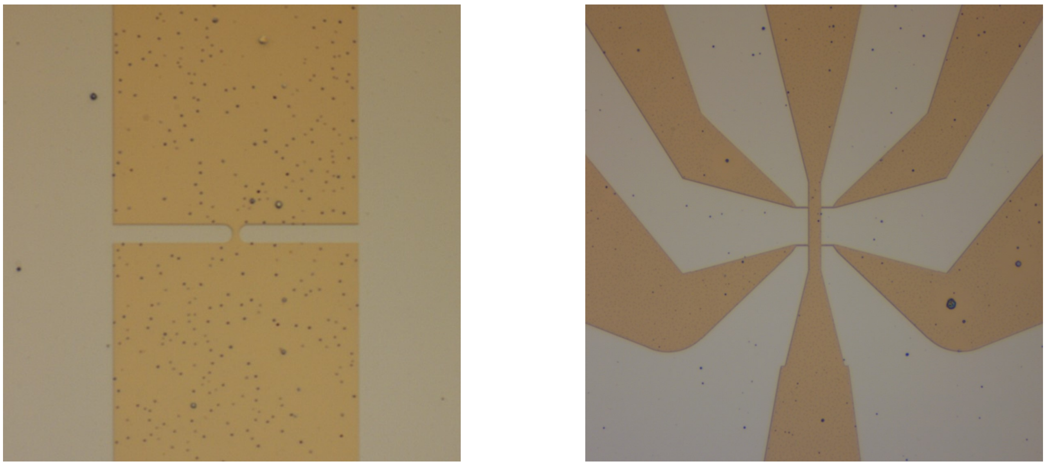

(a) (b)

Figure 3.5: Optical microscope images of two devices at different magnifications. Figure (a) shows a nanowire with a width of 500 nm between two electrodes. Figure (b) shows a Hall bar with a width of 5 µm.

3.2 Structural characterization of devices

The characterization of the main structures of the devices is done by SEM (see Figure 3.6a) during the fabrication process, when structures are defined in the chromium metal mask. With the electron probe, dimensions are checked to validate the real dimensions of the system. To do so, we fabricate at the center of the chip an island of "control devices" with the single goal of being measured at this stage, to prevent any damage to the actual devices from SEM measurement. By inspection of Figure 3.6b, the width and length of the structures are within 2-3% of the desired dimension.

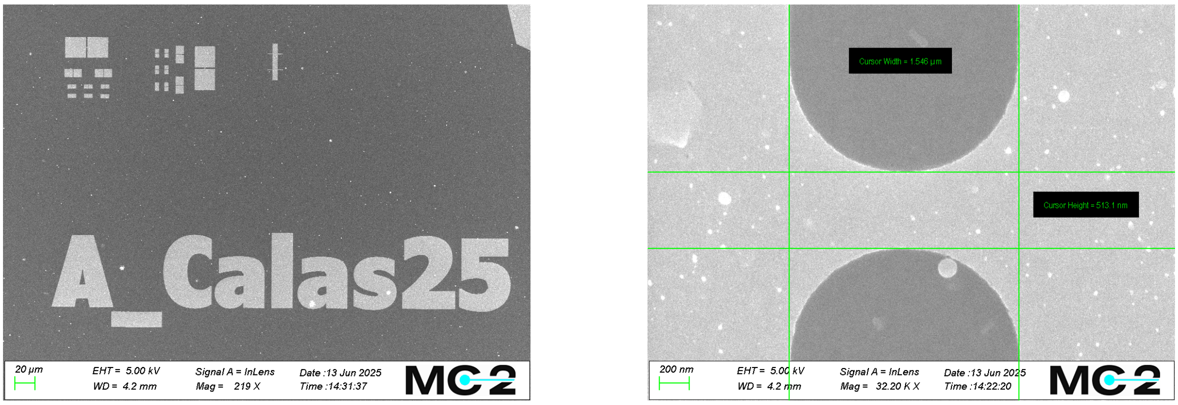

(a) (b)

Figure 3.6: (a) Island of "control devices" and device chip's name for identification. (b) SEM measure of device (Nanowire) dimensions; the desired width is 500 nm

4

Realization of Zn-doped YBCO Phase diagram

In this chapter, the reader is guided through the experimental work that forms the core of this thesis, building on the background established in Chapter 2.

To map the phase diagram comprehensively, we started from four different target compositions:

- $YBa_2\left(Cu_{0.95}Zn_{0.05}\right)_3O_{7-\delta}$ (5% Zn-YBCO)
- $YBa_2\left(Cu_{0.92}Zn_{0.08}\right)_3O_{7-\delta}$ (8% Zn-YBCO)
- $Y_{0.7}Ca_{0.3}\left(Cu_{0.95}Zn_{0.05}\right)_3O_{7-\delta}$ (5% Zn-CaYBCO)
- $Y_{0.7}Ca_{0.3}\left(Cu_{0.92}Zn_{0.08}\right)_3O_{7-\delta}$ (8% Zn-CaYBCO)

The two Zn concentrations lead to an expected reduction in the critical temperature of 40-45 K for the 5% samples and 64-72 K for the 8% samples, according to Ref. [20].

The inclusion of Ca in the YBCO lattice allows us to explore the strongly overdoped regime, whereas the Ca-free films enable investigation of the full doping range from undoped to slightly overdoped ($p = 0.19$).

Starting from a single deposited film for each target composition, the hole concentration was then modified iteratively using the following sequence: *characterization* (XRD and transport measurements) → *ex-situ annealing* → *further characterization.* By repeating this procedure for each doping level and for each of the four target compositions, we systematically tuned the hole concentration and mapped a large portion of the phase diagram.

4.1 XRD measurements

In order to extract the c-axis lattice parameter from the symmetric scan, it is fundamental to fix a reference in the XRD pattern. Since the (002) STO reflection is the strongest and lies at the center of the $2\theta-\omega$ scan, it is the most convenient choice. This ensures removal of any drift in the angular position of the peaks due to the offsets introduced in each measurement, and it is fundamental to compare c-axis measurements at different doping levels. Each scan is rigidly shifted so that the (002) STO reflection matches the reference tabulated value for this reflection, $2\theta_{STO}^{(002)} = 47.28°$. Peaks position in 2θ space is determined using the "peak parameter" tool of the XRD viewer software, provided directly by the company. The number of peaks available to calculate the c-axis depends on doping. As discussed in Chapter 2, due to the lattice matching between YBCO and STO, the (003ℓ) reflections of YBCO are very close to or beneath the (00ℓ) reflections of STO (ℓ integer), complicating the extraction of peaks positions for these reflections. As δ increases, the c-axis expands and some of these YBCO reflections separate sufficiently from STO to be resolved. Figure 4.1 shows representative scans around the scan center at different doping levels: from $p \approx 0.18$ to $p \approx 0.08$ the (006) reflection is hidden beneath the (002) STO reflection. For $p < 0.08$, the two peaks are resolved. The same occurs in the overdoped regime, where the (006) reflection lies on the right side of the (002) STO (not shown in the image). The gold pads create another undesired reflection in the diffraction scan, the (111) Au. This peak is located at an angle 2θ close to the (005) YBCO reflection, for which the same problem discussed above for the (003ℓ) reflections occurs. From each reflection, I calculated the c-axis parameter using equation (2.4), then took the average with the standard deviation as experimental uncertainty. The resulting c-axis values from the symmetric scan together with the hole doping p for 5% and 8% Zn are collected in Table 4.1.

The in-plane lattice parameters are determined from the asymmetric scan: starting from the $2\theta - \omega$ maps (see Figure 2.8), I integrate over ω to form a 1D profile in 2θ. This data set is then fitted using the model:

$$y = a_1 \mathrm{e}^{-(x-b_1)^2/c^2} + a_2 \mathrm{e}^{-(x-b_2)^2/c^2} + d_1 x + d_2$$

where $x = 2\theta$ and y is the intensity (total counts). The two peaks are modeled as Gaussians with the same σ on a linear background. An example is shown in Figure 4.2, where both data and fit are displayed after background subtraction. The fit yields b_1 and b_2, from which the lattice parameters a and b are calculated using Equation (2.6).

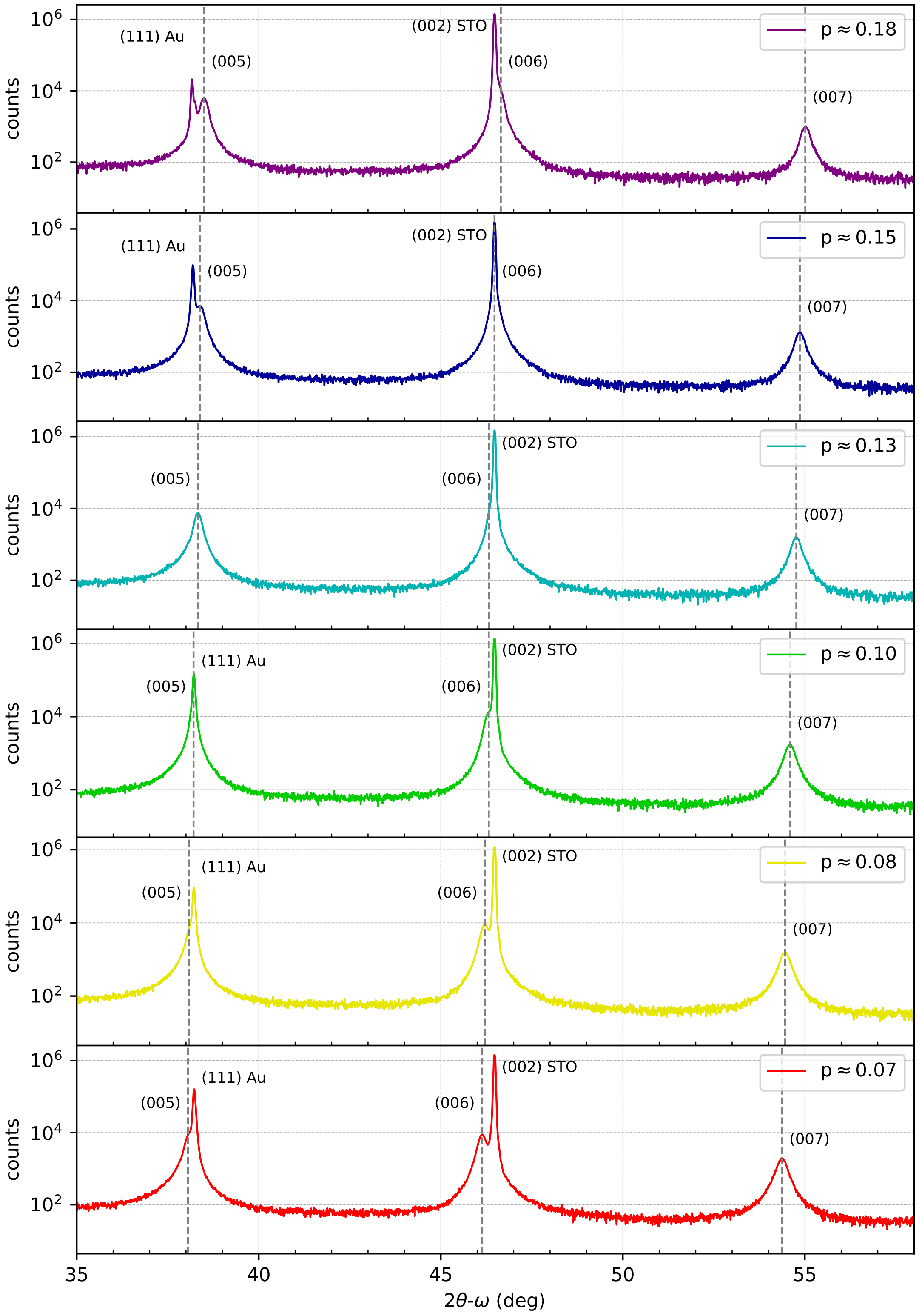

Figure 4.1: $2\theta - \omega$ XRD scans of 5% Zn-doped YBCO sample from 35° to 58° at different hole doping concentration. All graph are centered around the (002) reflection of STO which is at 47.28°. The vertical lines represent the position of the (005), (006) and (007) reflections of YBCO. With decreasing p the YBCO reflections shift to lower angles, i.e. the c-axis increases.

p	c (Å)
0.180	11.675(3)
0.177	11.678(2)
0.169	11.686(6)
0.158	11.697(3)
0.152	11.703(1)
0.145	11.711(4)
0.140	11.716(1)
0.137	11.720(2)
0.135	11.722(4)
0.130	11.728(6)
0.120	11.739(4)
0.113	11.748(1)
0.104	11.758(4)
0.079	11.789(6)
0.067	11.802(6)

(a) *5% Zn-doped YBCO*

p	c (Å)
0.189	11.668(4)
0.187	11.670(3)
0.160	11.693(6)
0.158	11.695(4)
0.154	11.699(3)
0.147	11.706(6)
0.143	11.710(1)
0.140	11.713(4)
0.138	11.716(6)
0.131	11.723(7)
0.125	11.729(8)
0.120	11.735(5)
0.088	11.772(5)
0.066	11.798(3)
0.063	11.802(2)

(b) *8% Zn-doped YBCO*

Table 4.1: c-axis and hole doping for the two zinc concentrations. Numbers in parentheses are statistical standard deviations of the last significant digit.

As oxygen is removed by annealing, the (308) and (038) peaks move towards each other and the unit cell passes from the orthorhombic to the tetragonal phase. In Figure 4.3 the in-plane lattice parameters are plotted as a function of the hole doping. The graph can be divided into three areas[1]:

- from $p \approx 0.18$ to $p \approx 0.14$ the unit cell is orthorhombic with $a = 3.8440(2)$ Å and $b = 3.8872(2)$ Å
- from $p \approx 0.14$ to $p \approx 0.10$ the unit cell makes the transition from the orthorhombic to the tetragonal
- below $p \approx 0.10$ the unit cell is tetragonal with $a = b = 3.8680(7)$ Å

Comparing our results with those obtained for bulk pristine YBCO [40], we find that the transition to the tetragonal structure in pure YBCO occurs at $\delta \approx 0.65$, corresponding to a hole doping of $p \approx 0.05$. This value is lower than what we observe, $p \approx 0.10$. Since the structural transition depends only on the oxygen content δ and not directly on the hole doping (which instead governs transport properties), we can

---

[1] Numbers in parentheses are statistical standard deviations of the last significant digit

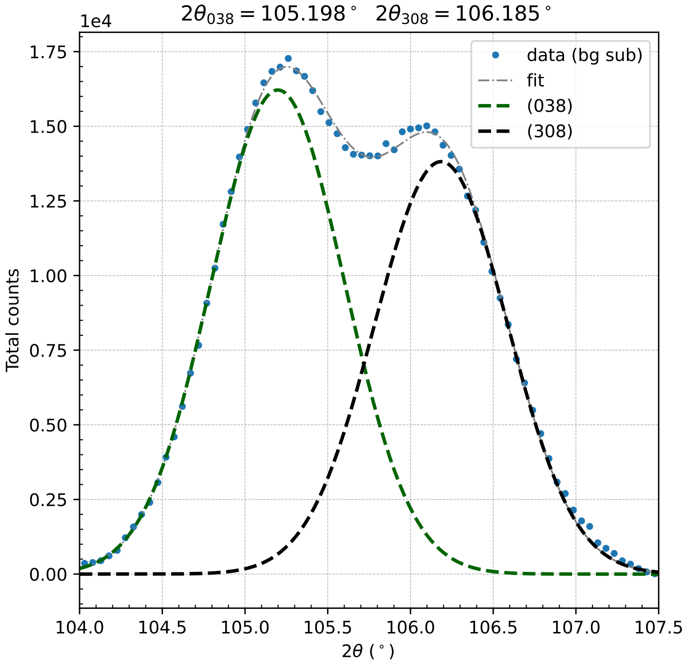

Figure 4.2: Example of fit for the determination of the position of the (308) (038) reflections. The data processed here are the same of Figure 2.8. The data (blue dots) are plotted with the linear background subtracted. The green and black dotted lines are the two Gaussian peaks extracted from the fit (gray dotted line).

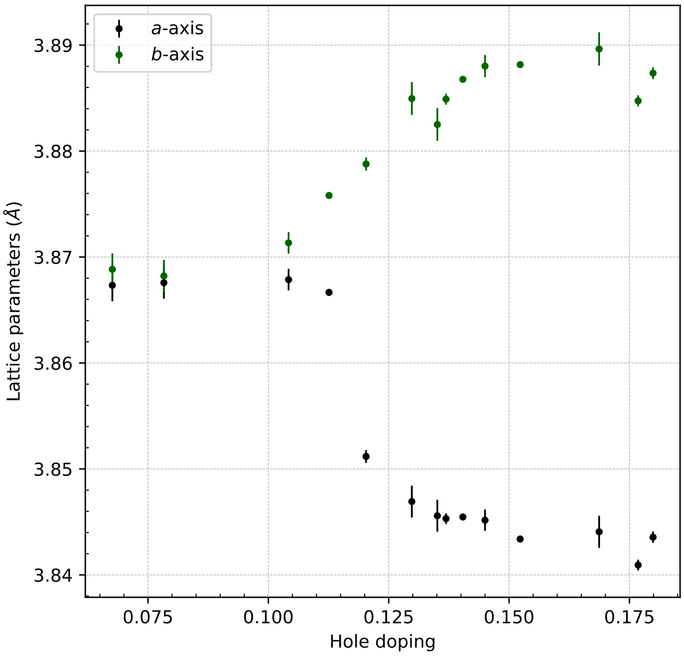

Figure 4.3: in-plane lattice parameters vs hole doping for 5% Zn-doped YBCO. a-axis black dots, b-axis green dots. The unit cell is orthorhombic for $p > 0.14$ and tetragonal for $p < 0.10$. For $0.10 < p < 0.14$ the unit cell changes from orthorhombic to tetragonal.

conclude that, for the same δ, Zn-doped YBCO exhibits a higher effective hole doping. This can be explained by the substitution of Cu with Zn in the CuO_2 planes: while the number of oxygen atoms (and hence the total number of holes) remains fixed, the reduction of copper sites increases the number of holes per Cu atom.

Regarding the in-plane lattice parameters, we find that the b-axis in the orthorhombic phase is comparable to the value reported for pristine YBCO, whereas the a-axis is about 1% larger than the bulk value ($a = 3.8227(1)$ Å at $\delta = 0.07$). This difference can be attributed to strain induced by the substrate: since the STO lattice parameter is 3.905 Å, the a-axis is subjected to a stronger tensile strain than the b-axis, which is only weakly affected. A similar effect is observed in the tetragonal phase, where the in-plane lattice parameter is about 0.1% larger than the pristine values ($a = b = 3.8600(1)$ Å). The strain effect gradually diminishes as the lattice parameters of YBCO approach those of STO.

When comparing our a-axis values in the orthorhombic phase directly with YBCO thin films grown on STO [38], we find very good agreement. This reinforces the conclusion that Zn substitution does not significantly alter the lattice structure, and that deviations from bulk YBCO are instead related to substrate-induced strain.

Table 4.2 summarizes the data presented in Figure 4.3, together with the c-axis values from Table 4.1a, providing a complete lattice characterization as a function of hole doping for 5% Zn-doped YBCO.

p	a (Å)	b (Å)	c (Å)
0.180	3.8436(5)	3.8874(6)	11.675(3)
0.177	3.8410(5)	3.8847(5)	11.678(2)
0.169	3.844(1)	3.890(2)	11.686(6)
0.152	3.8434(2)	3.8882(3)	11.703(1)
0.145	3.845(1)	3.888(1)	11.711(4)
0.140	3.8455(3)	3.8868(3)	11.716(1)
0.137	3.8453(5)	3.8849(5)	11.720(2)
0.135	3.846(1)	3.882(1)	11.722(4)
0.130	3.847(1)	3.885(2)	11.728(6)
0.120	3.8512(6)	3.8788(6)	11.739(4)
0.113	3.8667(2)	3.8758(3)	11.748(1)
0.104	3.868(1)	3.871(1)	11.758(4)
0.079	3.868(1)	3.868(1)	11.789(6)
0.067	3.867(1)	3.869(1)	11.802(6)

Table 4.2: Lattice parameters for 5% Zn-doped YBCO in function of hole doping. Numbers in parentheses are statistical standard deviations of the last significant digit.

4.2 Transport measurements

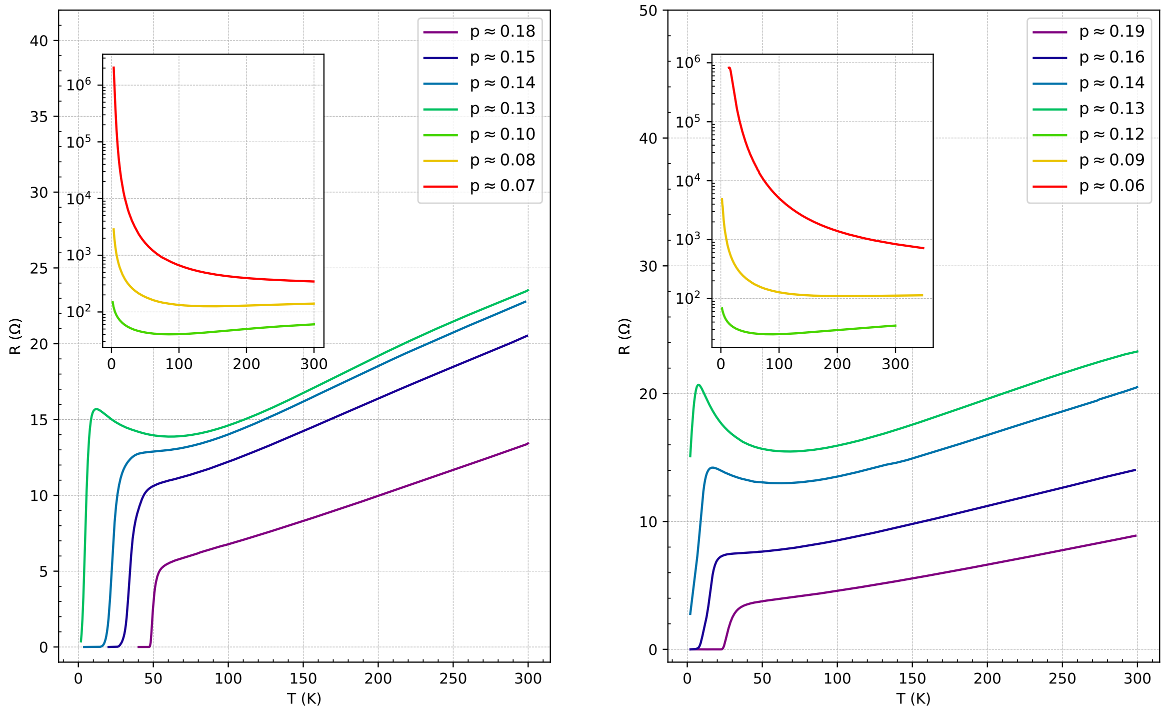

(a) *5% Zn-doped YBCO*

(b) *8% Zn-doped YBCO*

Figure 4.4: Resistance vs temperature $R(T)$ in function of the hole doping for the two zinc concentrations. The main graphs shows the $R(T)$ from the slightly overdoped to the underdoped; in the insets the insulating region.

The resistance of thin films was measured as a function of temperature in the range 300 K–2 K for most measurements. Figure 4.4 shows the $R(T)$ curves for the two Zn concentrations as a function of hole doping. As the post-annealing pressure decreases, both the critical temperature T_c (see Figure 2.11) and the hole doping are reduced. With decreasing doping, the $R(T)$ evolves from the optimally doped behavior (purple) to the antiferromagnetic insulating regime (red): the temperature interval where resistance is linear narrows and shifts to higher temperatures. In the underdoped regime, an upward curvature appears just above the superconducting transition. This curvature becomes more pronounced as doping is reduced, causing resistance to increase rapidly. Once superconductivity is completely suppressed, the upturn steepens further and the resistance rises abruptly.

For 8% Zn-doped films, the insulating regime is reached at higher hole doping compared to 5% samples. Thanks to the patterned gold pads, the geometry is fixed,

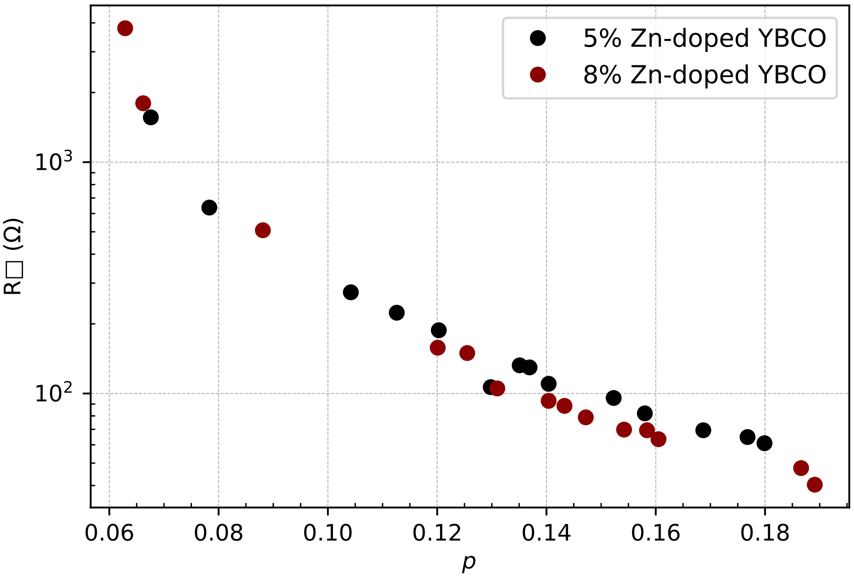

Figure 4.5: Sheet resistance vs hole doping for the two Zn concentrations.

making it possible to directly compare the sheet resistance, defined as $R_\square = R\pi/\log(2)$ at 300 K, as a function of hole doping. Oxygen reduction leads to a marked increase in $R_\square$, from a few tens of ohms in the underdoped regime up to several hundreds of ohms in the insulating region. Figure 4.5 reports the sheet resistance for both Zn concentrations as a function of hole doping. As hole doping decreases, $R_\square$ grows steadily from high doping to $p \approx 0.10$, then increases more rapidly at lower doping. In Figure 4.6 we compare the superconducting transition for the two zinc concentrations in the slightly overdoped regime ($\delta \approx 0$). The superconducting transition in 8% is located at a lower temperature compared to 5%. The critical temperatures are 49.1 K and 26.1 K for 5% and 8%, respectively. Compared with the critical temperature of pure bulk YBCO (92 K), we measure a reduction of ≈ 47% for 5% and ≈ 72% for 8%, which is in the range of reduction expected for these levels of zinc doping. The transition appears broader in 8%: from the derivative, we obtain $\Delta T_c = 2.5\,\mathrm{K}$ for 5% and $\Delta T_c = 6\,\mathrm{K}$ for 8%, by taking the FWHM of the peaks. The larger broadening at higher Zn concentration can be ascribed to the increase in the number of scattering centers for Cooper pairs. This enhanced disorder makes the superconducting properties more inhomogeneous, naturally resulting in a wider transition.

To develop the phase diagram, we need to extract from the $R(T)$ the critical temperature T_c, the pseudogap temperature T^* and the Nèel temperature T_N. These characteristic temperatures have been defined in Section 2.4. T^* is a crossover temperature; therefore, we need to define a criterion to determine where the linearity in the

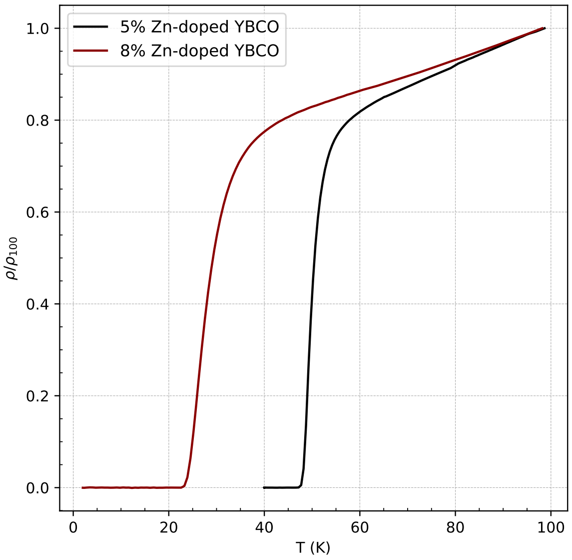

Figure 4.6: Comparison of the $R(T)$ at the fully oxygenated level ($\delta \approx 0$) for the two zinc doping concentration. The resistivity is normalized to its value at 100 K

$R(T)$ is lost. Following the work done in the past by the "QManD" group at Chalmers, I used the so-called 1% criterion: the pseudogap temperature is identified as the temperature at which the measured resistance deviates by 1% from the value predicted by the high-temperature linear fit of $R(T)$; in formula: $\Delta R\% = (R - R_l)/R_l$ where R_l is the resistance value from the linear fit. Figure 4.7 presents how I extract T^* from the $R(T)$.

The critical temperature and the Nèel temperature are transition temperatures and, hence, are well defined:

- T_c is the maximum of the first derivative, corresponding to the temperature where the highest slope is achieved. This definition of the critical temperature is often called in the literature "average critical temperature", $\overline{T}_c$ or T_c^{av}
- T_N is the minimum of $R(T)$ and can be extracted directly from the $R(T)$ or as the zero of its first derivative.

As an example for the extraction of T_c from the $R(T)$ we complete the characterization of 8% Zn-doped YBCO at $p \approx 0.16$. Figure 4.8 presents the complete $R(T)$, with the high temperature linear fit and the two characteristic temperatures, and its derivative, for the determination of T_c. To extract T_N we characterize the $R(T)$ of 8% Zn-doped YBCO at $p \approx 0.09$ which is in the insulating region. Figure 4.9 shows the upturn in resistance after the minimum, which is the Nèel temperature. Table 4.3 summarizes the results of transport characterization for the two concentrations of zinc.

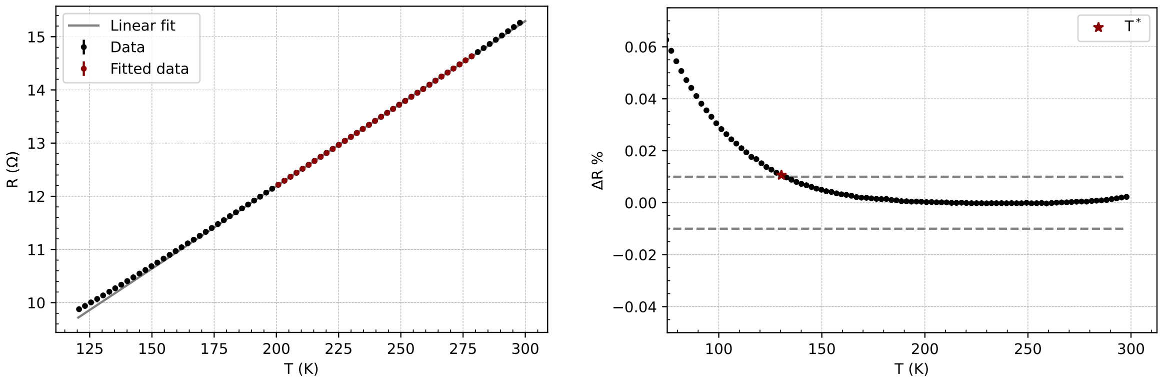

(a)

(b)

Figure 4.7: Pseudogap characterization for 8% Zn-doped YBCO $R(T)$ with $p \approx 0.16$. (a) High-temperature linear fit. The first data points (from 280 K to 300 K) are discarded due to the instability of the system at the end of the acquisition. Error bars are smaller than the symbols. (b) Black dots show $\Delta R\%$, which is defined in the text; dotted gray lines represent the 1% criterion; red star marks the pseudogap temperature, $T^* = 130\,\mathrm{K}$

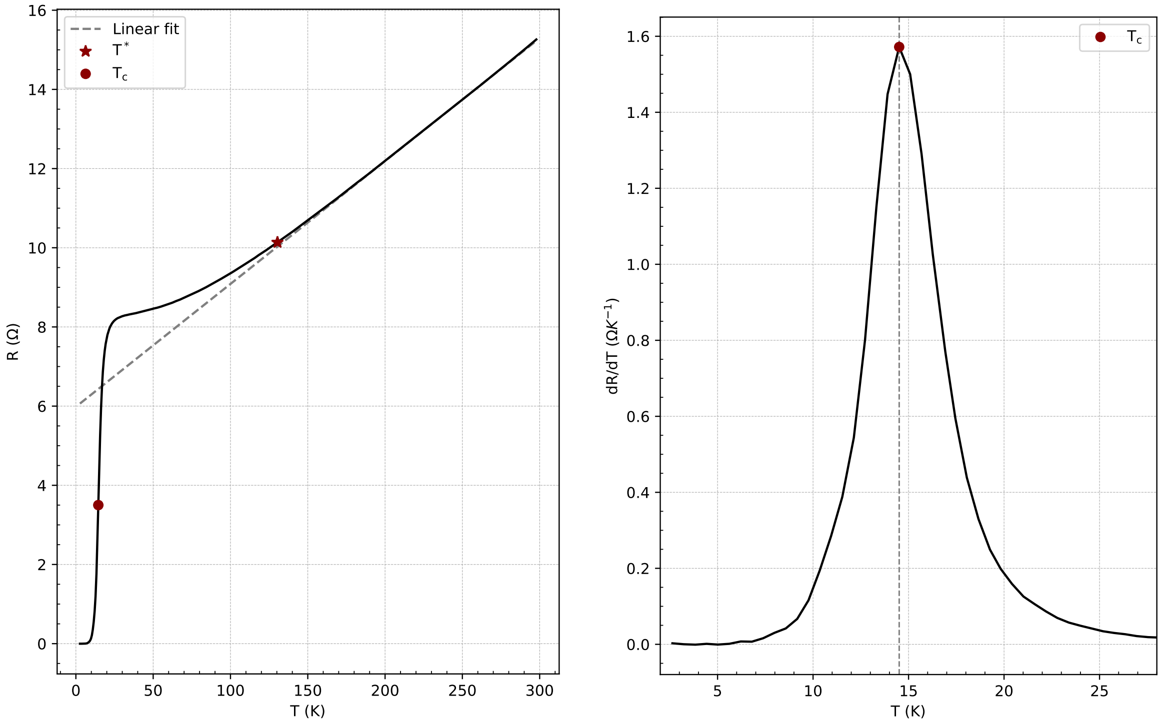

(a)

(b)

Figure 4.8: $R(T)$ for 8% Zn-doped YBCO at $p \approx 0.16$. Panel (a) shows the complete $R(T)$ (black line), high temperature linear fit (gray dotted line), T_c (red dot) and T^* (red star). Panel (b) shows the derivative of $R(T)$ and its maximum value (red dot). The gray vertical line marks the peak at $T_c = 14.6\,\mathrm{K}$

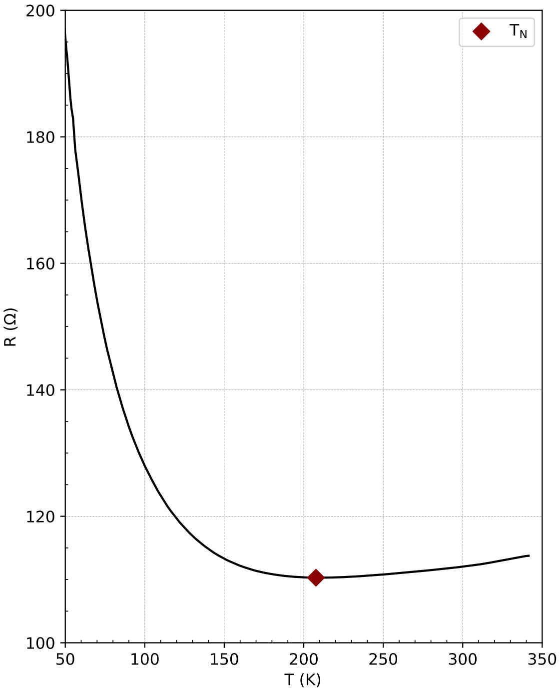

Figure 4.9: $R(T)$ of 8% Zn-doped YBCO at $p \approx 0.09$. Red diamond represent the Nèel temperature. $T_N = 210\,\mathrm{K}$

p	$R_{300K}(\Omega)$	T_c(K)	T^*(K)	T_N(K)
0.180	13.4	49.2		
0.177	14.3	49.1		
0.169	15.3	47.7	119.5	
0.158	18.1	43.3	130.0	
0.152	21.1	34.2	179.0	
0.140	24.3	22.2	187.2	
0.137	28.6	16.2	193.4	50.2
0.135	29.2	9.6	198.1	53.6
0.130	23.5	4.1	210.8	61.3
0.120	41.4		224.5	71.3
0.113	49.3			76.8
0.104	60.4			86.2
0.079	140.4			148.9
0.067	344.6			>300

(a) *5% Zn-doped YBCO*

p	$R_{300K}(\Omega)$	T_c(K)	T^*(K)	T_N(K)
0.189	8.9	26.1		
0.187	10.5	25.6		
0.160	14.0	15.0	128.9	
0.158	15.3	14.6	130.4	
0.154	15.4	14.2	126.7	
0.147	17.4	10.8	160.7	
0.143	19.5	9.6		
0.140	20.5	8.8		
0.131	23.2	2.0		68.0
0.125	33.0			87.0
0.120	34.8			87.0
0.088	112.0			210.0
0.066	396.6			>350
0.063	836.7			>350

(b) *8% Zn-doped YBCO*

Table 4.3: Transport characterization for the two zinc concentrations.

4.3 Hole doping

As discussed in Section 2.5.2, hole doping is determined using the empirical relation given by Equation (2.7), which is valid for pure YBCO. To start the analysis, we first collected data from ref. [38]. In that study, YBCO thin films were grown on both STO (100) (the same substrate used in this work) and MgO (110). The latter substrate has a rectangular in-plane lattice, with the long side measuring 5.96 Å and the short side equal to that of MgO (100), i.e. 4.21 Å. This difference induces a significant strain in YBCO films. As a result, the difference in substrate employment is directly reflected in both the c-axis lattice parameter and the critical temperature, which exhibit slightly different values at equal oxygen content. The data collected for pure YBCO are summarized in Table 4.4.

T_c (K)	c (Å)
86.9	11.731(9)
85.9	11.754(7)
80.6	11.76(1)
76.3	11.756(10)
60.1	11.78(1)
52.5	11.79(1)
49.9	11.794(6)
42.5	11.811(6)
37.7	11.820(6)
33.1	11.829(9)
23.7	11.839(6)
0.0	11.86(1)

(a) *YBCO on MgO*

T_c (K)	c (Å)
87.8	11.680(5)
88.9	11.693(8)
87.6	11.712(5)
83.5	11.724(1)
71.9	11.726(1)
67.6	11.735(4)
60.2	11.740(5)
52.7	11.757(8)
52.3	11.76(1)
48.3	11.77(1)
36.0	11.786(4)
29.2	11.80(2)

(b) *YBCO on STO*

Table 4.4: Data for YBCO grown on STO and MgO from ref. [38].

To construct a single dataset, it is necessary to correct for the offsets in T_c and the c-axis lattice parameter. This normalization is achieved by performing an initial parabolic fit to the data from each substrate, carefully excluding the points in the vicinity of the "1/8 anomaly". Based on the fit results, a global translation along both axes is applied to the MgO dataset to align it with the STO data.

This procedure yields a unified dataset for pure YBCO. A final parabolic fit is then performed on the merged data to extract the parameters required to implement Equation (2.7): the maximum critical temperature ($T_{c,\text{max}}$) and the corresponding c-axis lattice parameter (c_{max}). Figure 4.10 shows the raw data, the merged dataset, and the corresponding fits, while Table 4.5 summarizes the fit results.

The empirical relation presented in Equation (2.7) is now employed to calculate the hole doping level p. For data points close to the "1/8 anomaly", the calculated doping is below the value predicted by the parabolic model. This discrepancy is attributed to

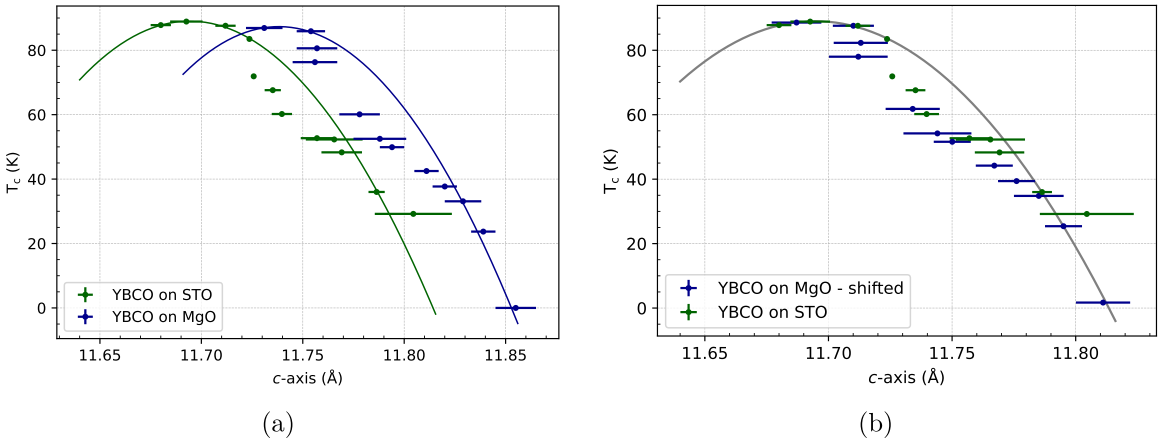

Figure 4.10: (a) Plot of raw data (Table 4.4). Solid lines represent the parabolic fit to the data. Data points around the "1/8 anomaly", for which the critical temperature is reduced due to the presence of CDW, are removed from the fits. (b) Plot of merged data after the translation of MgO data to STO. The gray line represent the parabolic fit. Data points around the "1/8 anomaly", are again removed from the fit.

Substrate	$c_{\max}$ (Å)	$T_c^{\max}$ (K)
MgO	11.738(4)	87.3(6)
STO	11.694(1)	89.0(3)
MgO+STO	11.694(1)	89.0(2)

Table 4.5: Fit result for pure YBCO. Numbers in parentheses are statistical standard deviations of the last significant digit.

the presence of charge density waves (CDW), which compete with superconductivity and suppress T_c.

We now perform the p Vs c-axis fit, following the model proposed in ref. [38]:

$$y = ax + b \times 10^9 x^6 \tag{4.1}$$

where y represents the hole doping and x is defined as $x = 1 - c/c_0$. The term c_0, representing the c-axis parameter at zero doping, is treated as a free parameter in the fit. From the fit results: $c_0 = 11.872(6)$Å. Figure 4.11 displays both the data and the fit. We now have a relation for $p(c)$ that is valid in the entire oxygen content range for YBCO on STO. Finally, we can calculate the hole doping for the Zn-doped YBCO samples.

As discussed in Section 2.5.2, samples containing Ca require a different approach. For 5% Zn-doped YBCO, the T_c Vs c-axis parabolic relation holds like in pure YBCO (see Figure 4.12). Therefore, it is possible to infer the "equivalent c-axis", defined

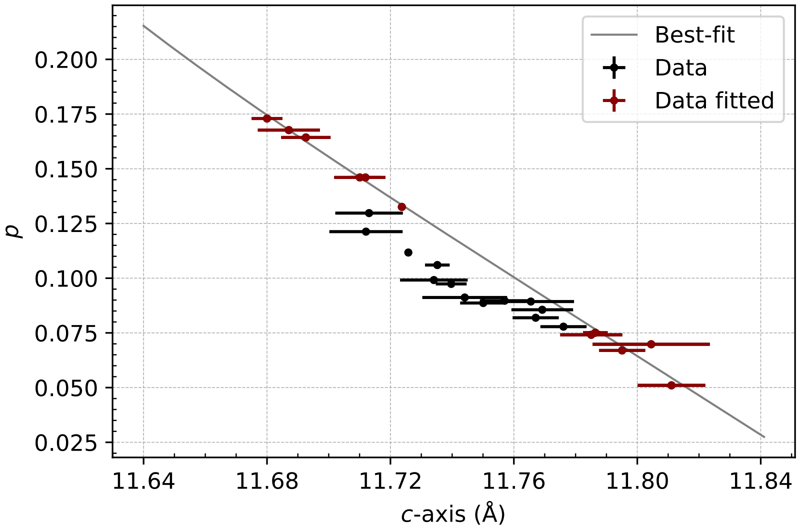

Figure 4.11: Hole doping Vs c-axis for pure YBCO. The fit (gray line) is performed in the region far from the "1/8 anomaly". Fitted data are shown in red.

as the c-axis value that a 5% Zn-doped YBCO film would require to reproduce the measured T_c in the overdoped region of the superconducting dome. Through c-axis^{eq}, we can employ the $p(c)$ relation previously found and extract the hole doping for 5% Zn-doped CaYBCO. The characterization of the data collected for 5% Zn-doped CaYBCO is presented in Table 4.6a.

For 8% Zn-doped YBCO the T_c vs c-axis parabolic relation does not hold within our dataset, preventing direct application of this method to determine hole doping in 8% Zn-doped CaYBCO. Instead, we can exploit the work done with 5% Zn-doped CaYBCO and find a relation between the measured c-axis and c-axis^{eq}. Assuming linearity between these quantities, we perform a linear fit to infer c-axis^{eq} for 8% Zn-doped CaYBCO, then apply the $p(c)$ relation to extract hole doping values. Table 4.6b summarizes the characterization for 8% Zn-doped CaYBCO.

p	T_c (K)	c (Å)
0.222	11.4	11.704(8)
0.209	29.2	11.795(8)
0.176	51.3	11.807(6)

(a) *5% Zn-doped CaYBCO*

p	T_c (K)	c (Å)
0.222	5.7	11.709(4)
0.218	7.3	11.721(5)
0.200	11.4	11.780(5)
0.196	13.3	11.785(3)

(b) *8% Zn-doped CaYBCO*

Table 4.6: Complete characterization of Zn-doped CaYBCO, for both zinc concentration. Numbers in parentheses are statistical standard deviations of the last significant digit.

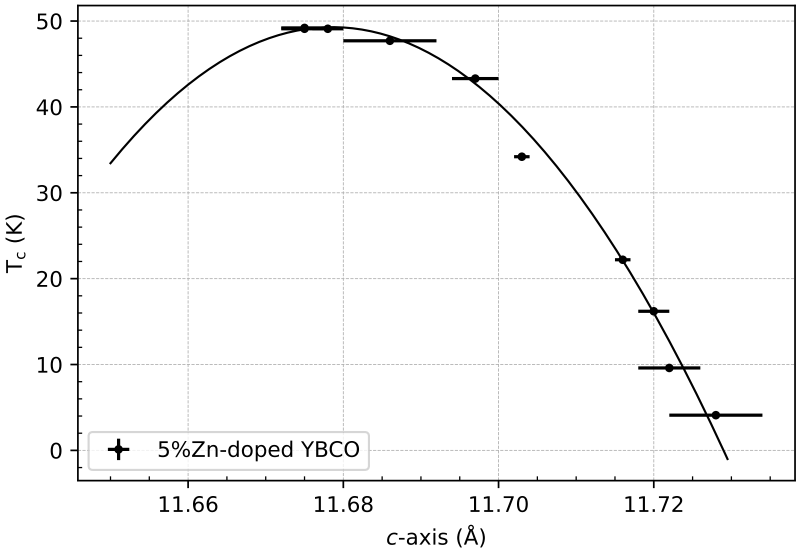

Figure 4.12: T_c Vs c-axis for 5% Zn-doped YBCO data. The gray line is the parabolic fit.

4.4 Phase diagram

All the work carried out so far converges in the realization of the phase diagram for the two Zn concentrations of YBCO, shown in Figure 4.13. We now compare how the different regions of the phase diagram evolve upon Zn substitution, starting from the pristine material.

The antiferromagnetic (AF) insulating region, located below $p = 0.05$ in pure YBCO, expands into the area left by the shrinking superconducting dome. This expansion is further enhanced by increasing the Zn content from 5% to 8%. The strengthening of AF order, concurrent with the suppression of superconductivity, supports the picture of a competing relationship between these two phases. The substitution of Cu^{2+} ($3d^9$, $S = \frac{1}{2}$) with spinless Zn^{2+} ($3d^{10}$) modifies the spin configuration in the CuO_2 planes, enhancing short-range antiferromagnetic correlations. As a result, the apparent strengthening of the insulating order could simply reflect the effect of chemical substitution, rather than a direct interplay with superconductivity.

The pseudogap crossover region remains essentially unchanged and appears to be unaffected by increasing Zn content. The slope for both Zn concentrations is comparable to that of the pristine material.

The superconducting dome is, as expected, the region where the most pronounced changes occur. First, $T_c^{\max}$ is suppressed, as already discussed at the beginning of this chapter. For 5% Zn-doped YBCO, the critical temperature decreases by approximately

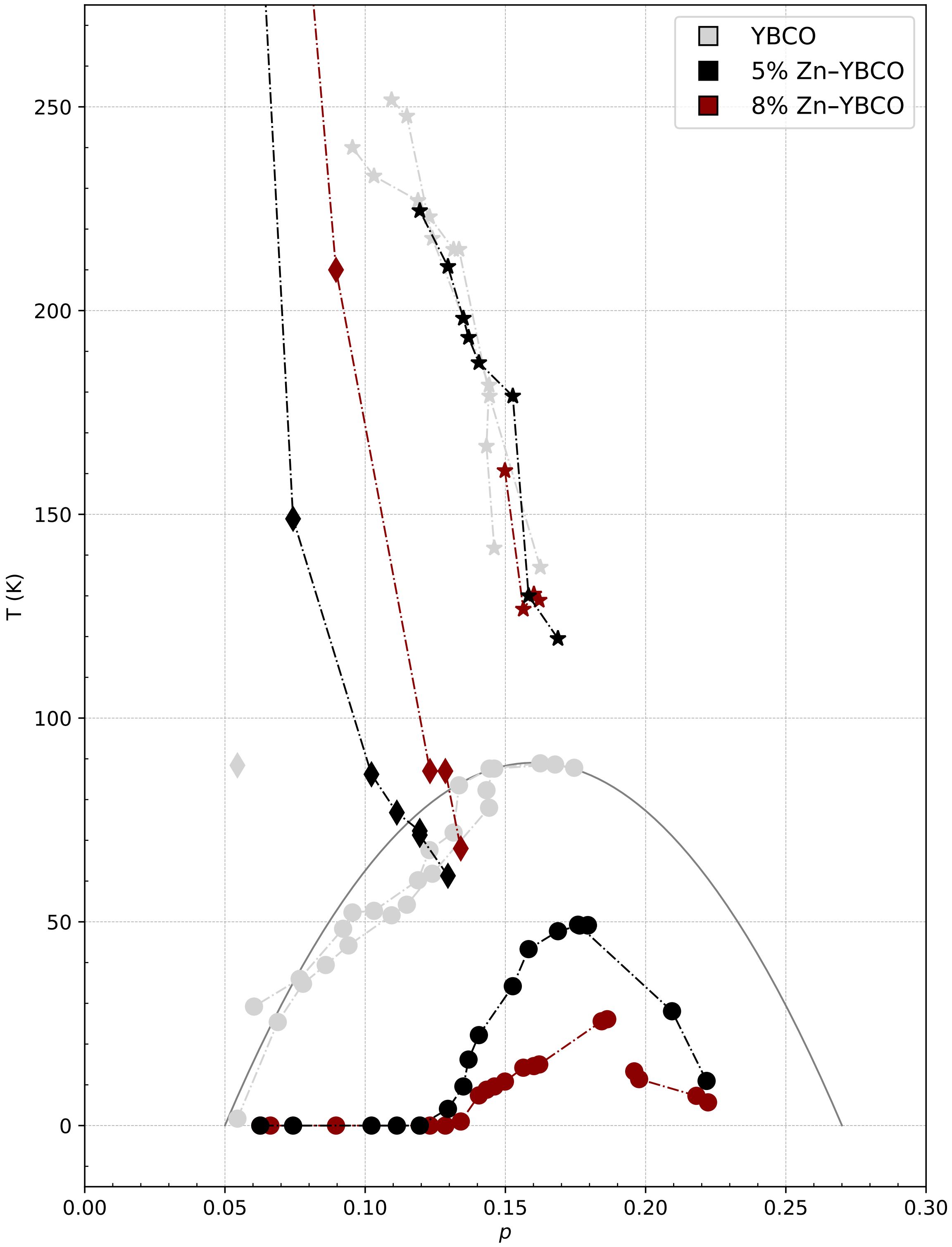

Figure 4.13: Phase diagram of Zn-doped YBCO. Dotted lines serve as a guide to the eye, while the grey solid line represents the best-fit parabolic dome for pristine YBCO. Circles indicate T_c, stars denote T^*, and diamonds correspond to T_N.

40 K, reaching a reduction of about 63 K for 8%, corresponding to T_c suppression of 44% and 70%, respectively (with reference to YBCO thin films on STO). These values are consistent with those reported in the literature. The introduction of Zn in the CuO_2 planes does not appear to lower T_c uniformly across all doping: in fact, the doping at which superconductivity vanishes, moves inwards, shrinking the superconducting region in p space. Zn substitution also modifies the optimal doping: in pure YBCO, $p_{\mathrm{opt}} = 0.16$, while from the parabolic fit of the 5% Zn-doped data we obtain $c_{\mathrm{max}} = 11.679\,\text{Å}$, corresponding to $p_{\mathrm{opt}}^{5\%} = 0.176$. Such a shift in optimal doping has also been reported in other works [51].

A crucial observation is that zinc, acting as a strong scatterer for Cooper pairs in the CuO_2 planes, acts selectively on superconductivity, leaving unaffected the pseudogap regime. One possible interpretation is that the pseudogap originates from pairing physics (pre-formed pairs, phase fluctuations) but does not involve long-range phase coherence. In this scenario, Zn impurities suppress phase coherence, thereby lowering T_c, while the pseudogap remains unaffected. Conversely, the pseudogap may correspond to a distinct electronic order that competes with superconductivity but arises from a different microscopic mechanism that does not rely on phase coherence. Although our data cannot unambiguously distinguish between these two interpretations, they clearly indicate that the pseudogap and superconductivity respond in fundamentally different ways to Zn substitution.

5

Transport characterization of Zn-doped YBCO Nanowires

Zn-doped YBCO provides a robust platform for investigating nanoscale phenomena. Once the phase diagram is established, size-dependent transport properties can be explored across different doping levels using nanodevices. We fabricated four thin-film chips, each with a thickness of $t = 60\,\mathrm{nm}$: two slightly overdoped (5% and 8% Zn) and two underdoped (5% and 8% Zn). The overdoped films correspond to hole concentrations of $p \approx 0.18$–0.19, while the underdoped films have $p \approx 0.14$. These values were determined from "twin" samples grown under identical deposition and annealing conditions as those used for the films intended for nanofabrication.

On each chip, both nanowires and Hall bars were patterned. In this chapter, we focus on the nanowires, using the widest Hall bars only as a reference for the post-fabrication thin-film resistance. The nanowires were designed with widths of 800 nm, 500 nm, 200 nm, 100 nm, and 60 nm, while their length l was fixed to maintain an aspect ratio of approximately 3:1 (see Figure 3.6b).

In the following, we will focus only on the 5% and 8% slightly overdoped nanowires. The reason for this choice is that at $p \approx 0.14$ the superconducting transition is too broad to allow reliable characterization. Specifically, for the 8% Zn-doped underdoped film shown in Figure 5.1b, superconductivity was observed only at $T = 2\,\mathrm{K}$, which is also the lowest temperature accessible by the PPMS. Since the zero resistance critical temperature of a nanowire is typically lower than that of the unpatterned film, characterization of nanowires at this doping level is not feasible. Similarly, in 5% Zn-doped YBCO at $p \approx 0.14$, the combination of underdoping, fabrication process, and superconductor–nanowire–superconductor geometry resulted in a finite resistance that persisted down to the lowest temperatures.

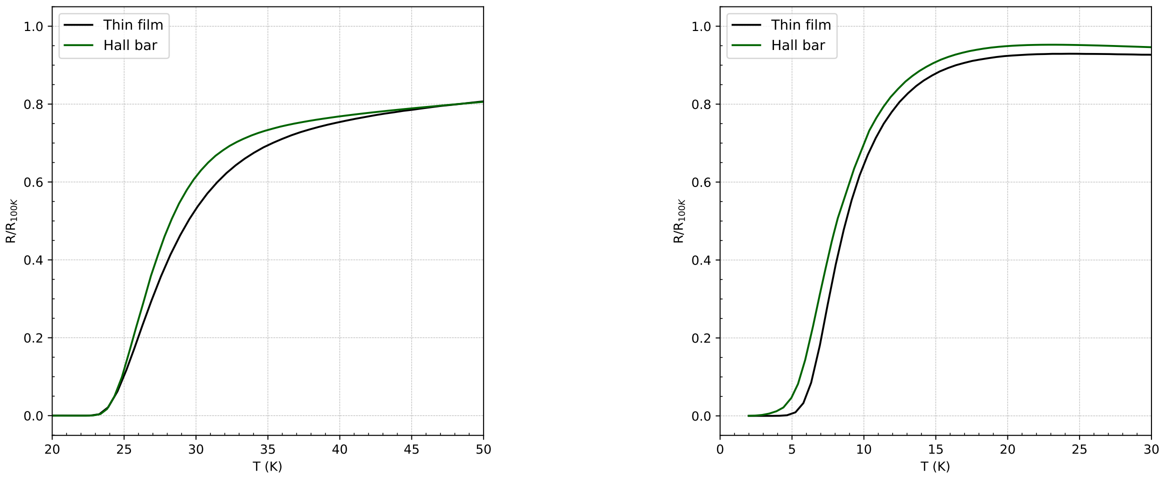

(a) *8% Zn-doped YBCO* $p \approx 0.19$

(b) *8% Zn-doped YBCO* $p \approx 0.14$

Figure 5.1: Comparison between the resistance of the film before (thin film) and after (Hall bar) fabrication. Resistance is normalize with its value at 100 K. The fabrication lowers T_c and makes the transition broader.

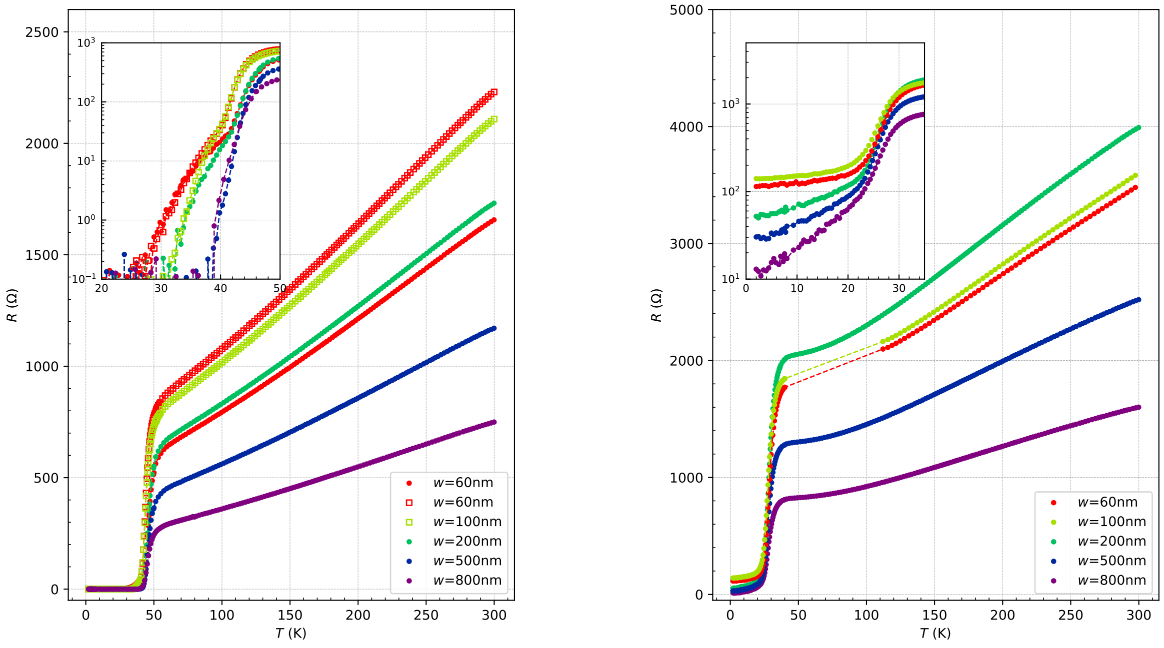

(a) $p \approx 0.18$

(b) $p \approx 0.14$

Figure 5.2: 5% Zn-doped YBCO nanowire R(T). The inset in each panel shows the behavior of the tail (y-axis is in log). (a) Wires with nominally the same width present similar values of T_c and normal state resistance. R_N (the value of the resistance where the tail began), on the other hand, is similar for both section. All the wires are superconductive. (b) the region between 50 K and 100 K is missing for the 60 nm and 100 nm wires due to a software issue on the acquisition program. No wire is superconductive.

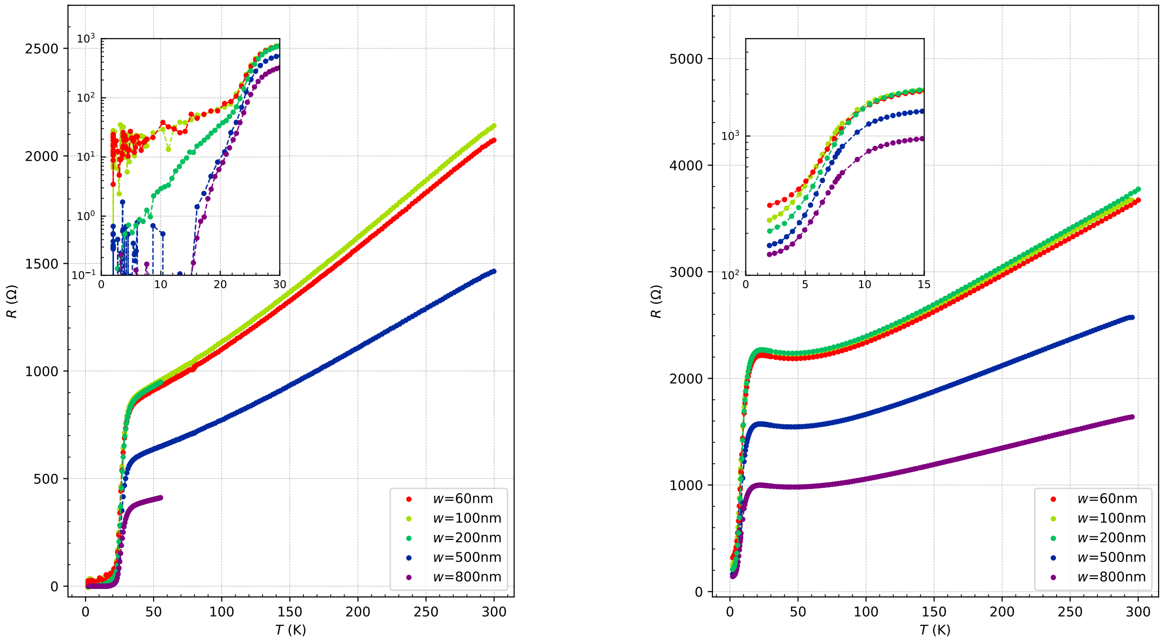

(a) $p \approx 0.19$ (b) $p \approx 0.14$

Figure 5.3: 8% Zn-doped YBCO nanowire R(T). The inset in each panel shows the behavior of the tail (y-axis is in log). (a) the normal state part at higher temperatures for the wires with 200 nm and 800 nm width has not been acquired. The 60 nm and 100 nm wires are not superconductive, the 200 nm wire reaches the superconducting state only at 2 K while the 500 nm and 800 nm are superconducting. (b) No wire is superconductive.

5.1 Resistance vs Temperature

The resistance of the nanowires was measured in the range 300 K–2 K (in almost all cases) as was done in the previous paragraph for the Hall bars. The fabrication design (see Figure 3.4a) enabled us to measure the transport properties of nanowires using four point probe configuration. In the four-probe configuration, which we needed to exclude any additional contributions from the contact resistance, the measured resistance includes not only that of the nanowire but also the contribution from the micrometric electrodes connecting the nanowire to the probes. In good approximation, the electrodes behave similarly to the bare thin film, while the nanowire in between exhibits confinement effects that modify the transport properties. Therefore, the total resistance reflects a series combination of the electrode resistance and the size-dependent resistance of the nanowire itself.

Figure 5.2 and 5.3 show the complete characterization of the nanowire resistance as a function of temperature. Figure 5.4 compares the normalized resistive transitions of

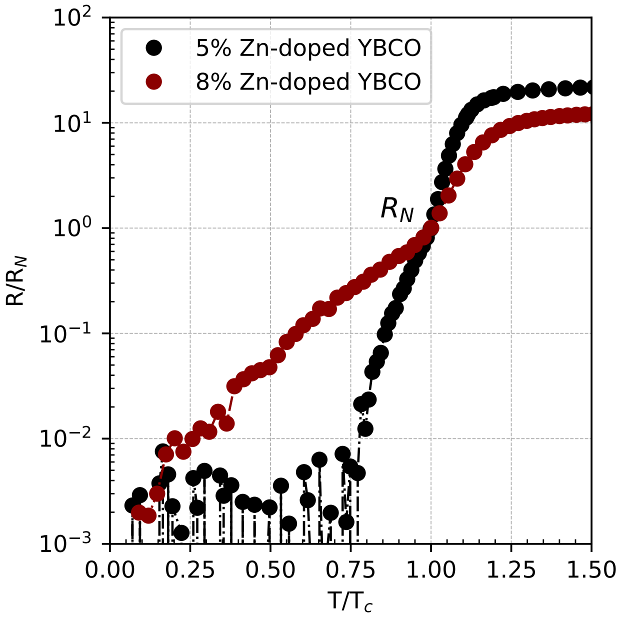

Figure 5.4: Comparison of the normalized resistive transitions for 200 nm wide nanowires with 5% and 8% Zn doping. The plot shows the broadening of the tail for the higher Zn concentration.

200 nm wide nanowires from the 5% and 8% slightly overdoped chips. The transition width increases with Zn concentration: the 8% nanowire shows a broader transition than the 5%.

In the following, we will focus on all nanowires from the 5% slightly overdoped chip and on the two widest nanowires (500 nm and 800 nm) from the 8% slightly overdoped chip, as these provide the most reliable transport data. In the insets of the figures, the superconducting transition of the nanowires appears broadened at lower temperatures, a feature that becomes particularly evident when plotted on a logarithmic scale. This broadening exhibits a behavior distinct from that of the thin films or the micrometric electrodes. It arises from two main factors: the entry of Abrikosov vortices into the nanowires and possible damage or degradation of the nanostructure induced by the patterning process. In the following section, we briefly introduce the theory of vortex entry, while in Section 5.2.1 we address the effects of nanostructure degradation within the framework of Bardeen's theory.

5.1.1 Theory of vortex slips in 3D nanowire

In superconducting nanostructures, the superconducting transition is often broadened by thermal fluctuations events. The microscopic mechanism responsible for this broadening depends on the effective dimensionality of the system. In wires ($w \gg \xi$) the dominant source of dissipation below T_c is the thermally activated crossing of Abrikosov vortices. A vortex nucleates at the sample edge, overcomes the Bean–Livingston surface barrier, and moves across the strip under the Lorentz force exerted by the bias current. Each crossing corresponds to a 2π slip of the superconducting phase and generates a voltage pulse; the stochastic sum of many such events produces the characteristic resistive broadening observed in the $R(T)$ curves of nanowires [52], which is at the origin of the lower zero resistance critical temperature.

The probability of a vortex entry event is controlled by the energy barrier, which depends strongly on the device geometry and on the intrinsic superconducting parameters, namely the coherence length ξ and the London penetration depth λ_L. Building on the theoretical framework proposed by Bulaevskii *et al.* [53], the expression for the resistance associated with vortex crossings was later refined by Arpaia *et al.* [52] and is given by:

$$R_v(T) = 7.1 R_\square \frac{l\xi(T)}{w^2} \left(\frac{\epsilon(T)}{k_B T}\right)^{\frac{3}{2}} \exp\left(-\frac{\epsilon(T)}{k_B T} \log \frac{1.47w}{\pi\xi(T)}\right) \tag{5.1}$$

where

$$\epsilon(T) = \frac{\Phi_0^2 t}{4\pi\mu_0\lambda_L^2(T)} \qquad \lambda_L(T) = \frac{\lambda_0}{\sqrt{1-(T/T_c)^2}} \qquad \xi(T) = \frac{\xi_0}{\sqrt{1-(T/T_c)^2}}$$

and $R_\square$ is the sheet resistance in the normal state and Φ_0 is the flux quantum.

5.1.2 Vortex entry Fit

As preliminary analysis we focus our attention on the 500 nm wide nanowires from the two zinc concentrations. To use Equation (5.1) as fit model, we exploit the $R(T)$ of 100 µm wide Hall bar to extract T_c and $R_\square$. Since the Hall bar has a ratio of 1:3, the sheet resistance is the resistance measured in the longitudinal direction divided by 3. From the structural characterization 3.6b we measure the dimensions (width and length) of the wire, which are in good agreement with the dimensions of the drawing in the Autocad mask. To establish where the nanowire transition begins, we decide to exploit again the $R(T)$ of the Hall bar: assuming that the electrodes have the same $R(T)$ as the Hall bar, the superconducting transition of the electrode ends at the temperature $T_{c,0}$ (the highest temperature where the resistance is zero). Extracting this parameter from the $R(T)$ we performed the vortex entry fit for the data under $T_{c,0}$.

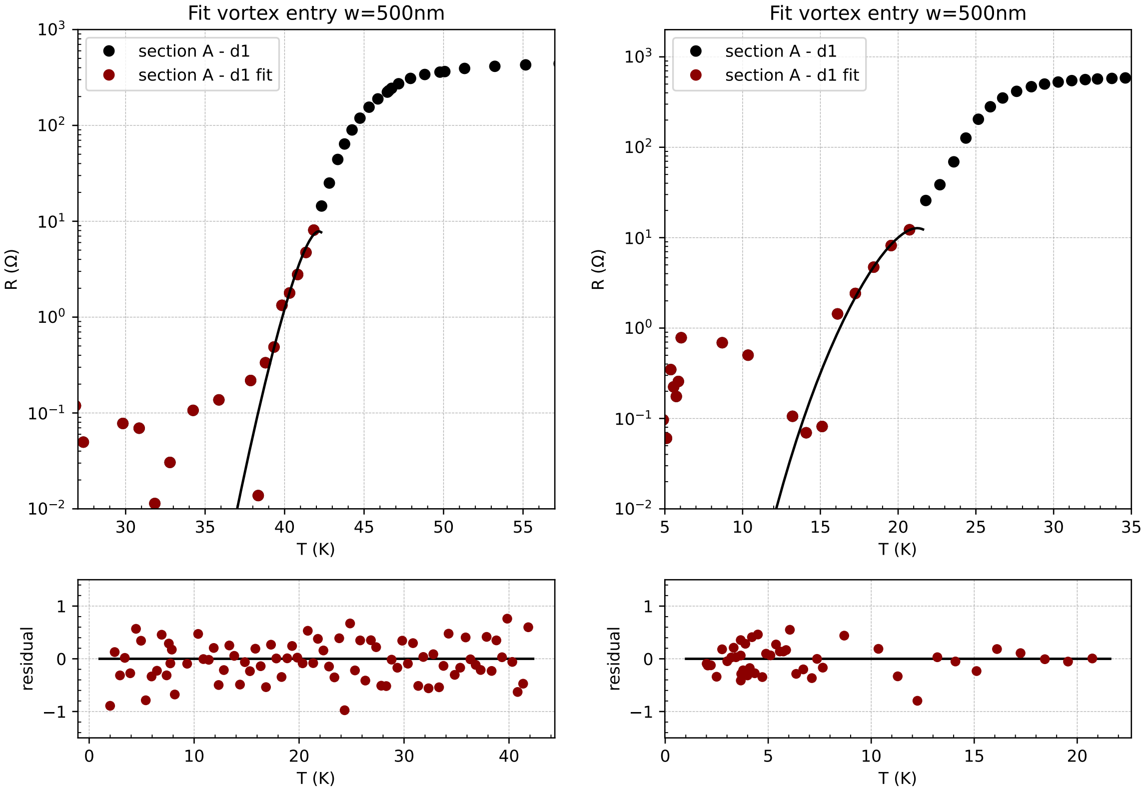

(a) *5% Zn-doped YBCO* (b) *8% Zn-doped YBCO*

Figure 5.5: Vortex-entry fits for 500 nm wide nanowires. Black dots show the experimental data, red dots indicate the fitted region, and solid black lines represent the fits. In the panel below are reported the residula from the fits. (a) 5% Zn-doped YBCO: $T_c = 43.0\,\mathrm{K}$, $R_\square = 20\,\Omega$ and $T_{c,0} = 41.7\,\mathrm{K}$. (b) 8% Zn-doped YBCO: $T_c = 23.0\,\mathrm{K}$, $R_\square = 28.3\,\Omega$ and $T_{c,0} = 21.6\,\mathrm{K}$.

Initial fits using the nominal nanowire dimensions systematically overestimated the superconducting properties of Zn-doped YBCO, yielding unphysically large values for the coherence length and penetration depth. This discrepancy indicates that the nanowires experienced partial degradation during the fabrication process. To account for this damage, we introduce effective dimensions smaller than the nominal values in the fit procedure. Specifically, we consider $w_{\mathrm{eff}} = 200\,\mathrm{nm}$ and $t_{\mathrm{eff}} = 30\,\mathrm{nm}$ for the 5% Zn-doped nanowire, and $w_{\mathrm{eff}} = 150\,\mathrm{nm}$ and $t_{\mathrm{eff}} = 25\,\mathrm{nm}$ for the 8%, reflecting the slightly higher damage level in the latter.

The nanowires length $l = 500\,\mathrm{nm}$, is not affected by damage. An additional form of degradation affecting our nanostructures is oxygen out-diffusion, which lowers T_c compared to the thin-film-like Hall bars. To account for this effect, we apply a uniform reduction of 2 K to the critical temperature for both zinc concentrations.

Figure 5.5 shows the vortex entry fits for 500 nm wide nanowires at both zinc concentrations. The model provides good agreement with the experimental data. The extracted fit parameters are summarized in Table 5.1. We observe that both the coherence length ξ_0 and the London penetration depth λ_0 increase with zinc concentration, consistent with previous reports in the literature [54, 55]. The increase with Zn concentration in the characteristic superconducting length scales accounts for the broader resistive transition observed in the 8% nanowire (Figure 5.4).

material	p	ξ_0 (nm)	λ_0 (µm)
5% Zn-doped YBCO	0.180	4.6(3)	1.0(1)
8% Zn-doped YBCO	0.189	6(1)	2.2(5)

Table 5.1: Fit result for the Vortex entry theory on 500 nm wide nanowires considering damage. Number in parenthesis is the statistical error resulting from the fit.

Nevertheless, due to the phenomenological nature of our damage correction and the inherent uncertainties in estimating effective dimensions, these values should be interpreted with caution. The substantial broadening of the superconducting transition observed in the nanowires likely arises from a combination of intrinsic effects due to Zn substitution and extrinsic degradation introduced during nanopatterning. Disentangling these two contributions would require a more systematic study with controlled damage levels, which is beyond the scope of this work.

5.2 Current-Voltage characteristics

The electrical transport properties of nanowires were then measured using external electronics, still keeping a four point probe configuration. In the Current – Voltage characteristics (IVC) we apply a current through the nanowire and electrode series and measure the resulting voltage drop across them. Figure 5.6 shows a Current – Voltage characteristics. The IVC for a YBCO nanowire has two states: in the zero voltage state the wire is superconducting, $R = \frac{\mathrm{d}V}{\mathrm{d}I} = 0$, while in the finite voltage state the wire is in its normal state, and $R = \frac{\mathrm{d}V}{\mathrm{d}I}$ is finite. The critical current, I_c, defines the transition between these two states and is the highest current that the superconductor can sustain without breaking out of superconductivity.

Since the nanowire acts as a constriction that locally suppresses the superconducting properties of the thin film, investigating I_c and the IVC in general can provide valuable insight into the transport properties of the nanowire itself. Moreover, in the transition from one state to the other the system may exhibit voltage steps called volt-

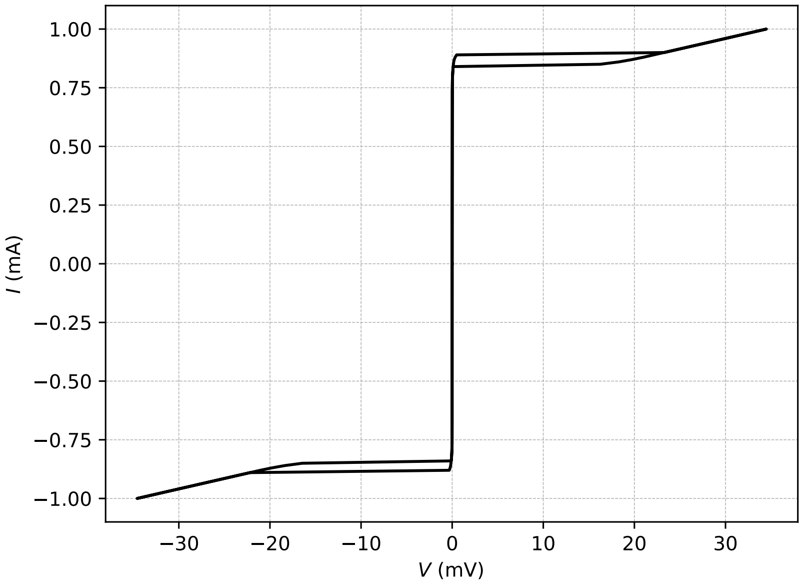

Figure 5.6: Example of a IVC for a 200 nm wide 5% Zn-doped YBCO nanowire. Between the two state of the nanowire there is a voltage switch of $\Delta V \approx 20\,\mathrm{mV}$. hysteresis effects are also present.

age switches: the nanostructure close to the critical current I_c is suddenly driven out of the superconducting state, in a non-continuous way. Together with the switches we observe a large hysteresis in the IVC characterization curve. These switches are well described in the literature of cuprates [37, 46, 56] and attributed to hot-spots. For our Zn-YBCO nanowires, however, it is not yet clear whether the origin of this behavior is the same.

From the IVC, we can measure I_c and by knowing the cross section of the wire, which is essentially $A_w = tw$, we can calculate the critical current density $J_c = I_c/A_w$. To extract I_c we use the 5 µV criterion: I_c is defined as the current that passes through the nanowire when the tension across the structure is 5 µV. Because of the hysteresis, we take the path with the higher current in the IVC.

Figure 5.7 shows the IVC measured from the 5% Zn-doped chip, at 2 K. The critical current does not vary significantly with nanowire width, implying that patterning-induced damage, which would be expected to be most severe in the narrowest nanowires, is minimal.

Figure 5.8a shows J_c (extracted from the IVC of Figure 5.7), measured at 2 K as a function of the width for 5% Zn-doped YBCO nanowires. The data in the plot are reported in Table 5.2. Figure 5.8b shows a comparison between J_c measured at 2 K as a function of the width for the two zinc concentrations. In 8% Zn-doped YBCO the critical current density is about one order of magnitude less that in 5%.

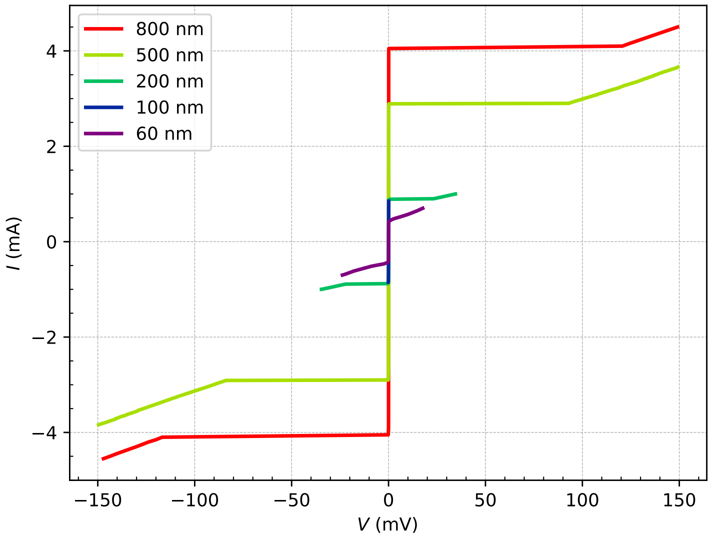

Figure 5.7: IVCs at 2 K as a function of nanowires width for 5% Zn-doped YBCO. The J_c extracted from each wire is reported in Table 5.2

w (nm)	$J_c \times 10^6$ (A cm^2)
60	9.55
100	9.96
200	6.23
500	8.77
800	8.12

Table 5.2: J_c at 2 K as a function of nanowires width for 5% Zn-doped YBCO.

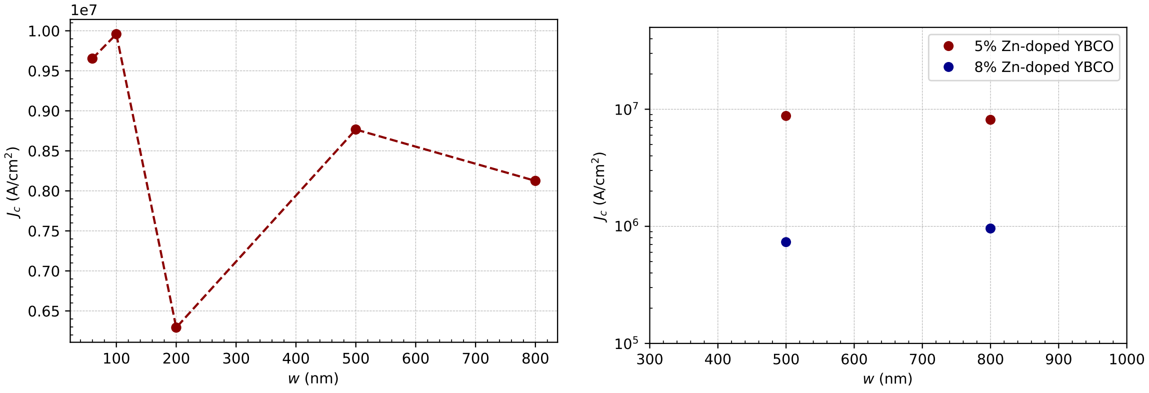

(a)

(b)

Figure 5.8: (a) critical current density J_c measured at 2 K as a function of the width for 5% Zn-doped YBCO nanowires at $p \approx 0.18$. For each width we measure only one nanowire, we have not done any statistics of J_c. (b) comparison between J_c measured at 2 K as a function of the width for the two zinc concentration.

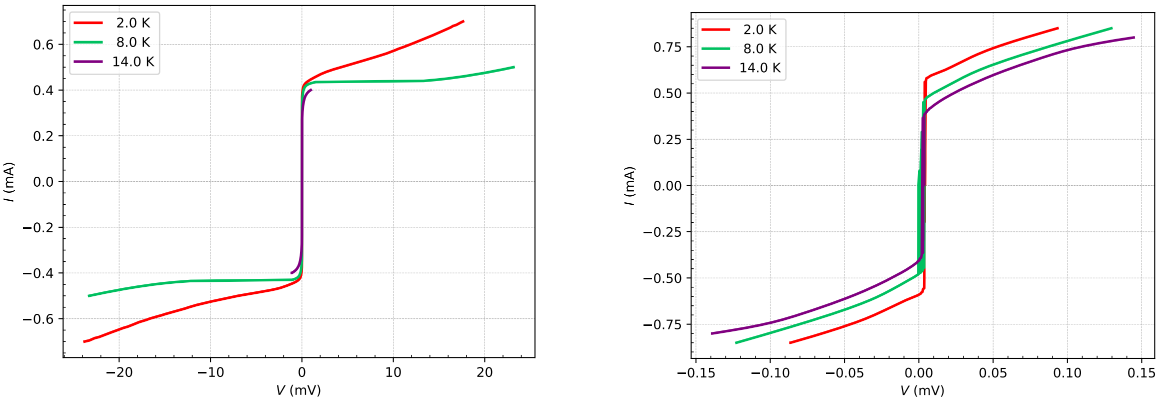

(a) $w = 60\,\mathrm{nm}$ (b) $w = 100\,\mathrm{nm}$

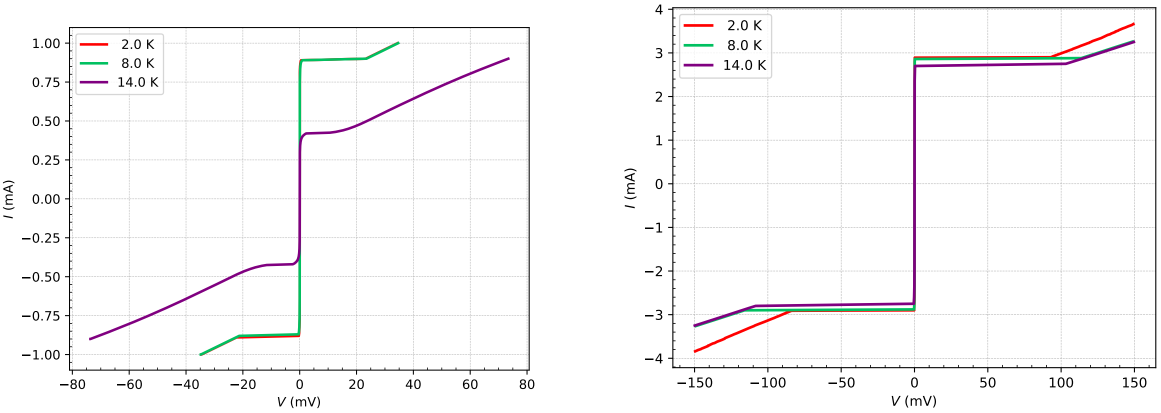

(c) $w = 200\,\mathrm{nm}$ (d) $w = 500\,\mathrm{nm}$

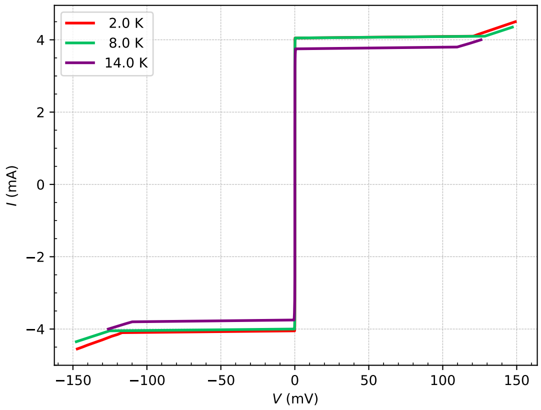

(e) $w = 800\,\mathrm{nm}$

Figure 5.9: Comparison of IVCs as a function of temperature at fixed width for 5% Zn-doped YBCO nanowires. Each panel shows how the critical current behave as a function of temperature. The critical current increase as temperature decrease for each width. In panel is present some noise from the measurement system in the measure at 8 K

In Figure 5.9 we compare the IVC at fixed width as a function of temperature for 5% Zn-doped YBCO. As expected for a superconductive device, the critical current grows as the temperature is decreased. In the widest wires, where the voltage switches are present, we observe that the general trend for ΔV as a function of temperature is the same as the critical current.

5.2.1 Bardeen fit as a probe of nanopatterning damage

A way to assess the quality of HTS nanostructures is to analyze the temperature dependence of the critical current density $J_c(T)$. Within the Ginzburg–Landau (GL) framework, the maximum supercurrent in a homogeneous superconductor is limited by the depairing current density. In the dirty limit ($\ell < \xi$), Bardeen derived a universal temperature dependence for $J_c(T)$ [57, 58, 45]:

$$J_c(T) = J_c(0)\left[1 - \left(\frac{T}{T_c}\right)^2\right]^{3/2} \tag{5.2}$$

where $J_c(0)$ is the zero-temperature extrapolation and T_c is the critical temperature.

Although originally formulated for conventional superconductors, Equation (5.2) has been shown to accurately describe the $J_c(T)$ of well-preserved YBCO nanowires, provided that nanopatterning does not introduce significant damage [59]. In practice, agreement with the Bardeen scaling across a broad temperature range indicates nearly pristine superconducting behavior at the nanoscale; conversely, systematic deviations (e.g. a faster suppression of J_c vs. T) are symptomatic of local inhomogeneities, edge damage, or granular weak links produced during fabrication.

In this work, we use the Bardeen fit on the 800 nm-wide nanowires to quantify the amount of degradation induced by patterning. This geometry, being closest to the thin-film limit, provides the most conservative estimate of processing damage. To perform the Bardeen fit, we need to collect J_c in a wide temperature range. Figure 5.10 shows the IVC collected to execute the fit for both zinc concentrations. We extracted J_c, reported in Table 5.3.

Figure 5.11 shows the bardeen fit for both Zn concentration. The fit results indicate that neither of our nanowires can be fully described by the Bardeen expression for J_c, although the discrepancy is relatively small. The trend is similar for both wires. Since the chips were fabricated together, we can assume that the amount of damage present in the wires is comparable.

$J_c \times 10^6$ (A cm^2)	T (K)
0	38.0
0.09	36.0
0.49	34.0
0.82	32.0
1.18	30.0
1.54	28.0
1.92	26.0
2.40	24.0
2.71	22.0
3.75	18.0
4.58	14.0
5.62	10.0
6.35	6.0

(a) *5% Zn-doped YBCO*

$J_c \times 10^5$ (A cm^2)	T (K)
0	20.0
0.017	18.0
0.08	16.0
0.20	14.0
0.33	12.0
0.49	10.0
0.61	8.0
0.75	6.0
0.85	4.0
0.96	2.0

(b) *8% Zn-doped YBCO*

Table 5.3: Characterization of the critical current density of 800 nm wide nanowires as a function of temperature

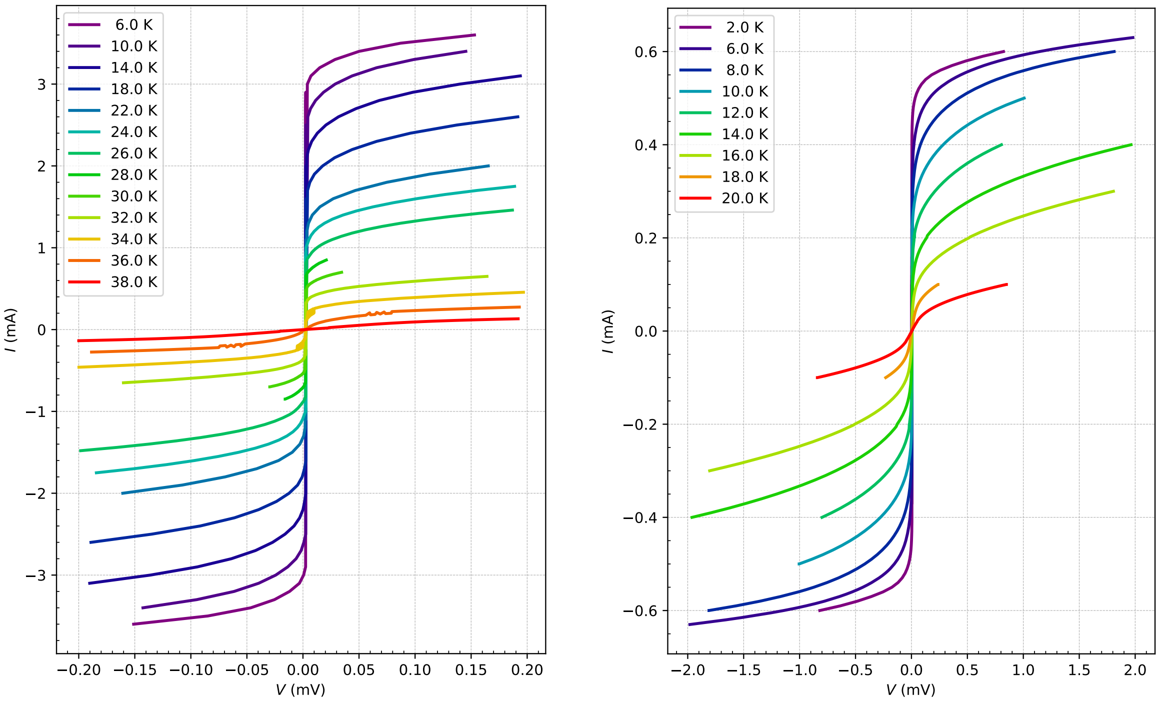

(a) *5% Zn-doped YBCO*

(b) *8% Zn-doped YBCO*

Figure 5.10: IVC as a function of temperature for the 800 nm wide nanowires. Extracted J_c are reported in Table 5.3

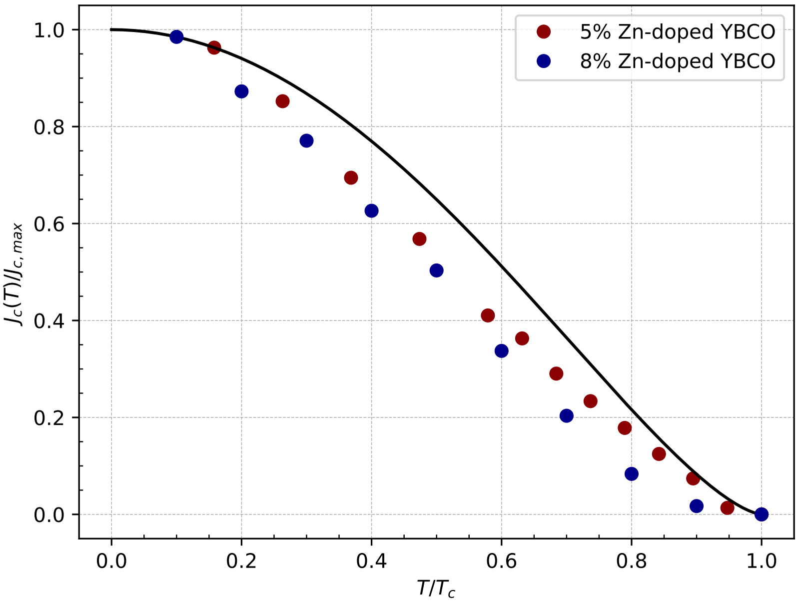

Figure 5.11: Normalized critical current density $J_c(T)/J_{c,max}$ measured under T_c. The data are reported in Table 5.3. Red dots, 5% Zn-doped YBCO, blue dots 8% Zn-doped YBCO, solid black line represent the normalized Bardeen expression. T_c is equal to 38 K and 20 K for 5% and 8% respectively, while the lower temperature measured (which correspond to $J_{c,max}$) is 6 K and 2 K, for 5% and 8% respectively.

6

Summary and outlook

The main achievement of this thesis has been the systematic optimization and characterization of Zn-doped YBCO thin films, deposited on STO substrates, spanning a wide doping range, in order to establish a material platform for the study of the normal state in cuprates. We have successfully deposited high-quality thin films with two different zinc concentrations (5% and 8%), and characterized them across the underdoped and overdoped regimes. The analysis of transport data, supported by XRD measurements, has allowed us to reconstruct the phase diagrams and to evaluate the effect of Zn substitution. Our results reveal a pronounced suppression of the superconducting transition temperature, an expansion of the insulating region, and a relative robustness of the pseudogap, confirming Zn as an effective probe to disentangle the complex interplay of orders in cuprates.

In the second part of the thesis, the investigation was extended to the nanoscale. Nanowires and Hall bars were successfully fabricated using the techniques optimized within the QManD group at Chalmers. To the best of our knowledge, this is the first time that such nanostructures have been realized from Zn-doped YBCO. Despite some fabrication-induced degradation, evidenced by broader superconducting transitions and reduced effective dimensions, transport characterization was successfully performed. Preliminary measurements confirmed the role of Zn as a strong suppressor of superconductivity: comparing the two zinc concentrations, we observed a reduction of the critical current and an increase of both the coherence length and the London penetration depth, consistent with enhanced pair-breaking scattering.

This work naturally opens up several compelling directions for future research:

- Perform systematic magneto-transport measurements on Zn-doped YBCO thin films.
- Apply advanced spectroscopic techniques, such as RIXS, ARPES, or STM, to directly probe the impact of Zn impurities on charge order and low-energy exci-

tations.

- Extend the magneto-transport characterization to Zn-doped YBCO Hall bars.
- Further optimize the fabrication process for Zn-doped YBCO nanostructures and carry out a systematic study of their transport properties.
- Fabricate and investigate capped Zn-doped YBCO nanowires, aiming to reduce nanostructure degradation and to probe the characteristic superconducting length scales of this material.

In conclusion, this thesis has shown that Zn-doped YBCO can serve as a reliable and versatile platform to investigate the normal state of cuprates. Through the combined effort of thin-film growth, transport measurements, and the first fabrication of nanostructures in this material, we have gained a clearer picture of how Zn affects superconductivity. These results not only confirm the role of Zn as an efficient suppressor of superconductivity, but also open the way to future experiments designed to unravel the mechanisms at the origin of high-temperature superconductivity.

Appendices

Fabrication process parameters A

Following the steps presented in Chapter 3 we add here more detailed information about the nanofabrication procedure, including chemicals.

Resist coating

A bilayer resist was employed in order to facilitate a reliable lift-off process:

- Bottom layer: MMA (8.5 MAA EL4).
- Top layer: ARP 6200.13 (1:1 dilution).

Both layers were spin-coated at 6000 rpm (acceleration 1000 rpm/s, 90 s total). The sample was subsequently soft-baked at 95–96°C for 5 minutes. This temperature are compatible to preserve YBCO properties

Lithography and development

The device patterns were exposed using electron beam lithography at 100 kV. After exposure, the two layers were sequentially developed:

- Top resist: o-xylene (97%) for $\sim$ 35 s, rinse in IPA, dry with N_2 gun for 10 s.
- Bottom resist: MIBK:IPA = 1:3 for $\sim$ 33 s, rinse in IPA, dry with N_2 gun for 10 s.

Hard mask deposition and lift-off

A 10 nm chromium layer was deposited in the Lesker 1 e-beam evaporator at 0.2 Å/s. Lift-off was performed in Remover 1165: 15 minutes immersion at 75°C, then ultrasonic at (∼70% power, <1 min). A final rinse in IPA under ultrasonic agitation completed the lift-off.

Carbon mask patterning

The carbon layer is etched by oxygen RIE:

- Power: 50 W
- Pressure: 100 mTorr
- Duration: 25 minutes

Profilometer measurements verified the etching depth.

Ion beam etching of YBCO

The underlying YBCO (and Au contacts) were defined by Ar^+ ion beam etching (IBE).

- Stage cooled with LN_2
- Etching angle: 25°
- Stage rotation: 5 rpm
- Monitoring: Secondary Ion Mass Spectroscopy (SIMS), with the etching stopped when the Ba signal vanished (indicating full removal of YBCO).

Profilometry was used to check the total etched thickness (C + Au + YBCO, with slight overetch into the STO substrate).

Final cleaning

The residual carbon on top of the nanostructures was removed by a two-step low-power RIE process in oxygen:

- 50 W, 100 mTorr, 3 min.
- 15 W, 100 mTorr, 60 min.

Acknowledgments

First of all, I would like to express my deepest gratitude to my supervisors, Riccardo Arpaia and Floriana Lombardi, for believing in me and making all this possible. Floriana, I am truly grateful for welcoming me into your research group. The energy and passion you brought to our discussions were fundamental to this work. You helped me discover my value as a researcher and motivated me to contribute to advancing our understanding of nature. Thank you for your scientific guidance over these past months. Riccardo, my deepest appreciation goes to you. You have been the pillar of this work. I am grateful for your daily guidance and unwavering support throughout the thesis process. Your advice and insights have been an invaluable source of knowledge and motivation to always strive for excellence. I appreciate your encouragement during the most critical moments, for providing me with a roof over my head, and for making my stay in Sweden possible. I will never forget the month we spent together as roommates; I couldn't have asked for anything better. You are the supervisor everyone would hope to have, and I am fortunate that our paths crossed.

I would like to acknowledge Alexei Kalaboukhov for his help and valuable advice on PLD, XRD, and PPMS; with you around, I always felt more confident. My appreciation extends to my colleagues: Kyril, Karn, Klinti, Alessia, Núria, Oscar, and Martina. I value the scientific discussions and moments (some of them a little crazy) we shared in the lab. I cherish the conversations in the kitchen, the ping-pong games, and the opportunity to enjoy Göteborg together. My time here would not have been the same without you.

Alessia, I owe much of this work to you: I sincerely appreciate all your help, sometimes silent yet ever-present, and for supervising me in the laboratory. Part of this work was only possible because of your contribution. My heartfelt recognition goes to my entire family. Mom, Dad, I am grateful to you for never imposing anything on me. I appreciate your unwavering pride in me and for always being by my side, whatever choices I have made over the years.

My recognition extends to my second family. Alessandro, Matteo, Mirco: perhaps an entire thesis would not be enough to explain how essential you are to my life. You are the family I have chosen, and if I have reached this point today, substantial credit belongs to you. I appreciate your patience and support, no matter what happens. You have always been there every time I have fallen, and if I can continue walking, it is only because, wherever I go, I always have you by my side.

To Alice, Tancredi, Giulia, and Azzurra, for always being there despite the distance. Geographical distance has never meant true distance: I appreciate every word of support and for reminding me, in moments of discouragement, that I could do it.

To all the people I have met during my time at university: I value the long study sessions together, made a little easier by coffee breaks and aperitifs. Thank you for the legendary evenings in Pisa and for putting me up when I needed it.

Mariachiara, my special appreciation goes to you. You were the light that illuminated my path when it was darkest. Without you, these last few years would not have been the same.

This work represents the closing of a circle for me, a long journey in which I have never walked alone. For this, I am deeply grateful.

Angelo Balistreri, Göteborg, November 2025

Bibliography

[1] Lord Kelvin. "XXIX. Aepinus atomized". In: *The London, Edinburgh, and Dublin Philosophical Magazine and Journal of Science* 3.15 (1902), pp. 257–283. DOI: 10.1080/14786440209462764.

[2] James Dewar and J. A. Fleming. "On the Electrical Resistivity of Pure Mercury at the Temperature of Liquid Air". In: *Proceedings of the Royal Society of London* 60 (1896), pp. 76–81.

[3] Heike Kamerlingh Onnes. "Further experiments with liquid helium. C. On the change of electric resistance of pure metals at very low temperatures etc. IV. The resistance of gold and pure mercury at helium temperatures". In: *Comm. 120b* (Apr. 1911). Same as: Versl. Kon. Akad. Wetenschappen, Amsterdam, Deel XIX, p. 1479.

[4] W. Meissner and R. Ochsenfeld. "Ein neuer Effekt bei Eintritt der Supraleitfähigkeit". In: *Naturwissenschaften* 21.44 (1933), pp. 787–788. DOI: 10.1007/BF01504252.

[5] F. London and H. London. "The electromagnetic equations of the supraconductor". In: *Proceedings of the Royal Society of London. Series A - Mathematical and Physical Sciences* 149.866 (1935), pp. 71–88. DOI: 10.1098/rspa.1935.0048.

[6] V. L. Ginzburg and L. D. Landau. "On the Theory of superconductivity". In: *Zh. Eksp. Teor. Fiz.* 20 (1950). Ed. by D. ter Haar, pp. 1064–1082. DOI: 10.1016/b978-0-08-010586-4.50078-x.

[7] A.A. Abrikosov. "The magnetic properties of superconducting alloys". In: *Journal of Physics and Chemistry of Solids* 2.3 (1957), pp. 199–208. ISSN: 0022-3697. DOI: https://doi.org/10.1016/0022-3697(57)90083-5.

[8] Emanuel Maxwell. "Isotope Effect in the Superconductivity of Mercury". In: *Phys. Rev.* 78 (4 May 1950), pp. 477–477. DOI: 10.1103/PhysRev.78.477.

[9] J. Bardeen, L. N. Cooper, and J. R. Schrieffer. “Theory of Superconductivity”. In: *Phys. Rev.* 108 (5 Dec. 1957), pp. 1175–1204. DOI: `10.1103/PhysRev.108.1175`.

[10] J. G. Bednorz and K. A. Müller. “Possible high T_c superconductivity in the Ba–La–Cu–O system”. In: *Zeitschrift für Physik B Condensed Matter* 64.2 (1986), pp. 189–193. DOI: `10.1007/BF01303701`.

[11] B. Keimer et al. “From quantum matter to high-temperature superconductivity in copper oxides”. In: *Nature* 518.7538 (2015), pp. 179–186. DOI: `10.1038/nature14165`.

[12] Götz Seibold et al. “Strange metal behaviour from charge density fluctuations in cuprates”. In: *Commun. Phys.* 4.1 (2021), p. 7. DOI: `10.1038/s42005-020-00505-z`.

[13] Eric Wahlberg et al. “Restored strange metal phase through suppression of charge density waves in underdoped $YBa_2Cu_3O_{7-\delta}$”. In: *Science* 373.6562 (2021), pp. 1506–1510. DOI: `10.1126/science.abc8372`.

[14] Riccardo Arpaia et al. “Signature of quantum criticality in cuprates by charge density fluctuations”. In: *Nat. Commun.* 14.1 (2023), p. 7198. DOI: `10.1038/s41467-023-42961-5`.

[15] Eric Wahlberg et al. “Boosting superconductivity: how nanofaceted surfaces transform the ground state of ultrathin $YBa_2Cu_3O_{7-\delta}$ thin films”. In: *arXiv preprint arXiv:2502.03986* (2025). DOI: `10.48550/arXiv.2502.03986`.

[16] J. L. Tallon et al. “Generic superconducting phase behavior in high-T_c cuprates: T_c variation with hole concentration in $YBa_2Cu_3O_{7-\delta}$”. In: *Physical Review B* 51 (1995).

[17] Henri Alloul, Takeshi Ohno, and Philippe Mendels. “^{89}Y NMR evidence for a Fermi-liquid behavior in $YBa_2Cu_3O_{6+x}$”. In: *Physical Review Letters* 63 (1989).

[18] Gang Xiao et al. “Variation of the superconducting properties of $YBa_2Cu_{3-x}Zn_xO_{7-\delta}$ with Zn concentration”. In: *Physical Review B* 38 (1988).

[19] Y. Fukuzumi et al. “Universal suppression of the magnetic susceptibility of cuprate superconductors by Zn substitution”. In: *Physical Review Letters* 76 (1996).

[20] S. Zagoulaev, P. Monod, and J. Jégoudez. “Magnetic and transport properties of Zn-doped $YBa_2Cu_3O_7$ in the normal state”. In: *Phys. Rev. B* 52 (14 Oct. 1995), pp. 10474–10487. DOI: `10.1103/PhysRevB.52.10474`.

[21] A. V. Mahajan et al. “^{89}Y NMR probe of Zn induced local moments in $\mathrm{YBa_2Cu_{2.97}Zn_{0.03}O_7}$”. In: *Physical Review Letters* 72 (1994).

[22] A. V. Balatsky, I. Vekhter, and Jian-Xin Zhu. “Impurity-induced states in conventional and unconventional superconductors”. In: *Reviews of Modern Physics* 78 (2006).

[23] M. I. Salkola, A. V. Balatsky, and J. R. Schrieffer. “Spectral properties of quasiparticle excitations induced by magnetic moments in superconductors”. In: *Physical Review B* 55 (1997).

[24] P. J. Hirschfeld and N. Goldenfeld. “Consequences of resonant impurity scattering in anisotropic superconductors: Thermal and spin relaxation properties”. In: *Physical Review B* 37 (1988).

[25] M.-H. Julien et al. “^{63}Cu NQR and NMR study of the effect of Zn doping in $\mathrm{YBa_2Cu_3O_{6.63}}$”. In: *Physical Review B* 63 (2001).

[26] B. Nachumi et al. “Muon spin relaxation studies of Zn-substitution effects in $\mathrm{YBa_2Cu_3O}_x$”. In: *Physical Review Letters* 77 (1996).

[27] G.-q. Zheng et al. “From d-wave to s-wave pairing in the cuprate superconductor $\mathrm{Bi_2Sr_2CaCu_2O}_{8+\delta}$ by Ni and Zn substitution”. In: *Physical Review Letters* 81 (1998).

[28] S. A. Kivelson, E. Fradkin, and V. J. Emery. “How to detect fluctuating stripes in the high-temperature superconductors”. In: *Reviews of Modern Physics* 67 (2003).

[29] J. J. Neumeier et al. “Hole filling and hole creation in $\mathrm{Y}_{1-x}\mathrm{Ca}_x\mathrm{Ba_2Cu_3O}_{7-\delta}$”. In: *Physical Review B* 39 (1989).

[30] J. L. Tallon et al. “Ca doping of $\mathrm{YBa_2Cu_3O}_{7-\delta}$: A study by Cu NQR”. In: *Physical Review B* 51 (1995).

[31] R. D. Shannon. “Revised effective ionic radii and systematic studies of interatomic distances in halides and chalcogenides”. In: *Acta Crystallographica Section A* 32 (1976).

[32] C. Gledel, J.-F. Marucco, and B. Touzelin. “Thermodynamics study of Y1-xCaxBa2Cu3Oz”. In: *Physica C: Superconductivity* 165.5 (1990), pp. 437–443. ISSN: 0921-4534. DOI: `https://doi.org/10.1016/0921-4534(90)90378-R`.

[33] C. Bernhard et al. “Magnetic penetration depth and condensate density of cuprate high-Tc superconductors determined by muon-spin-rotation experiments”. In: *Physical Review B* 59 (1999).

[34] Reza Baghdadi et al. “Study of in-plane electrical transport anisotropy of a-axis oriented $YBa_2Cu_3O_{7-\delta}$ nanodevices”. In: *Phys. Rev. B* 95.18 (2017), p. 184505. DOI: 10.1103/PhysRevB.95.184505.

[35] Riccardo Arpaia et al. “Untwinned $YBa_2Cu_3O_{7-\delta}$ thin films on MgO substrates: A platform to study strain effects on the local orders in cuprates”. In: *Phys. Rev. Materials* 3.11 (2019), p. 114804. DOI: 10.1103/PhysRevMaterials.3.114804.

[36] Giovanni Mirarchi et al. “Tuning the ground state of cuprate superconducting thin films by nanofaceted substrates”. In: *Commun. Mater.* 5.1 (2024), p. 146. DOI: 10.1038/s43246-024-00582-5.

[37] Riccardo Arpaia et al. “Transport properties of ultrathin $YBa_2Cu_3O_{7-\delta}$ nanowires: A route to single-photon detection”. In: *Phys. Rev. B* 96.6 (2017), p. 064525. DOI: 10.1103/PhysRevB.96.064525.

[38] Riccardo Arpaia et al. “Probing the phase diagram of cuprates with $YBa_2Cu_3O_{7-\delta}$ thin films and nanowires”. In: *Phys. Rev. Mater.* 2 (2 Feb. 2018), p. 024804. DOI: 10.1103/PhysRevMaterials.2.024804.

[39] Riccardo Arpaia et al. “Engineering underdoped CuO_2 nanoribbons in nm-thick a-axis $YBa_2Cu_3O_{7-\delta}$ films”. In: *Phys. Rev. Mater.* 8 (4 Apr. 2024), p. 044803. DOI: 10.1103/PhysRevMaterials.8.044803.

[40] J. D. Jorgensen et al. “Structural properties of oxygen-deficient $YBa_2Cu_3O_{7-\delta}$”. In: *Phys. Rev. B* 41 (4 Feb. 1990), pp. 1863–1877. DOI: 10.1103/PhysRevB.41.1863.

[41] Ruixing Liang, D. A. Bonn, and W. N. Hardy. “Evaluation of CuO_2 plane hole doping in $YBa_2Cu_3O_{6+x}$ single crystals”. In: *Phys. Rev. B* 73 (18 May 2006), p. 180505. DOI: 10.1103/PhysRevB.73.180505.

[42] T. Frello et al. “Superconductivity in an anomalously tetragonal $YBa_2Cu_3O_{6.62}$ single crystal: A possible singularity in the structural phase diagram”. In: *Phys. Rev. B* 67 (2 Jan. 2003), p. 024509. DOI: 10.1103/PhysRevB.67.024509.

[43] R Liang et al. “Preparation and characterization of homogeneous YBCO single crystals with doping level near the SC-AFM boundary”. In: *Physica C: Superconductivity* 383.1 (2002), pp. 1–7. ISSN: 0921-4534. DOI: https://doi.org/10.1016/S0921-4534(02)01269-8.

[44] S Nawaz et al. “Microwave response of superconducting $YBa_2Cu_3O_{7-\delta}$ nanowire bridges sustaining the critical depairing current: evidence of Josephson-like behavior”. In: *Phys. Rev. Lett.* 110.16 (2013), p. 167004. DOI: 10.1103/PhysRevLett.110.167004.

[45] S. Nawaz et al. “Approaching the theoretical depairing current in $YBa_2Cu_3O_{7-x}$ nanowires”. In: *Physica C* 495 (2013), pp. 33–38. DOI: 10.1016/j.physc.2013.07.011.

[46] S Charpentier et al. “Hot spot formation in electron-doped PCCO nanobridges”. In: *Phys. Rev. B* 94.6 (2016), 060503(R). DOI: 10.1103/PhysRevB.94.060503.

[47] Reza Baghdadi et al. “Toward $YBa_2Cu_3O_{7-\delta}$ Nanoscale Structures for Hybrid Devices”. In: *IEEE Trans. Appl. Supercond.* 25.3 (2014), p. 1100104. DOI: 10.1109/TASC.2014.2362991.

[48] Reza Baghdadi et al. “Fabricating nanogaps in $YBa_2Cu_3O_{7-\delta}$ for hybrid proximity-based Josephson junctions”. In: *Phys. Rev. Applied* 4.1 (2015), p. 014022. DOI: 10.1103/PhysRevApplied.4.014022.

[49] R Arpaia et al. “Improved noise performance of ultrathin YBCO Dayem bridge nanoSQUIDs”. In: *Supercond. Sci. Technol.* 30.1 (2016), p. 014008. DOI: 10.1088/0953-2048/30/1/014008.

[50] Eric Andersson et al. “Fabrication and electrical transport characterization of high quality underdoped $YBa_2Cu_3O_{7-\delta}$ nanowires”. In: *Supercond. Sci. Technol.* 33.6 (2020), p. 064002. DOI: 10.1088/1361-6668/ab807e.

[51] S H Naqib. “The effect of Zn substitution on the suppression of Tc of $Y_{1-x}Ca_xBa_2(Cu_{1-y}Zn_y)_3O_{7-\delta}$ superconductors: the pseudogap and the systematic shift of the optimum hole content”. In: *Superconductor Science and Technology* 20.10 (Aug. 2007), p. 964. DOI: 10.1088/0953-2048/20/10/012.

[52] R Arpaia et al. “Resistive state triggered by vortex entry in $YBa_2Cu_3O_{7-\delta}$ nanostructures”. In: *Physica C* 506 (2014), pp. 165–168. DOI: 10.1016/j.physc.2014.06.002.

[53] L. N. Bulaevskii et al. “Vortex-induced dissipation in narrow current-biased thin-film superconducting strips”. In: *Phys. Rev. B* 83 (14 Apr. 2011), p. 144526. DOI: `10.1103/PhysRevB.83.144526`.

[54] I. Kokanovi ć, J. R. Cooper, and M. Matusiak. “Nernst Effect Measurements of Epitaxial $Y_{0.95}Ca_{0.05}Ba_2(Cu_{1-x}Zn_x)_3O_y$ and $Y_{0.9}Ca_{0.1}Ba_2Cu_3O_y$ Superconducting Films”. In: *Phys. Rev. Lett.* 102 (18 May 2009), p. 187002. DOI: `10.1103/PhysRevLett.102.187002`.

[55] C. Panagopoulos et al. “Effects of Zn doping on the anisotropic penetration depth of $YBa_2Cu_3O_7$”. In: *Phys. Rev. B* 54 (18 Nov. 1996), R12721–R12724. DOI: `10.1103/PhysRevB.54.R12721`.

[56] M Ejrnaes et al. “Observation of dark pulses in 10 nm thick YBCO nanostrips presenting hysteretic current voltage characteristics”. In: *Supercond. Sci. Technol.* 30.12 (2017), 12LT02. DOI: `10.1088/1361-6668/aa94b9`.

[57] J. Bardeen. “Critical Fields and Currents in Superconductors”. In: *Rev. Mod. Phys.* 34.4 (1962), pp. 667–681. DOI: `10.1103/RevModPhys.34.667`.

[58] Michael Tinkham. *Introduction to Superconductivity.* 2nd ed. Mineola, NY: Dover, 2004. ISBN: 978-0486435039.

[59] G Papari et al. “High critical current density and scaling of phase-slip processes in YBaCuO nanowires”. In: *Supercond. Sci. Technol.* 25.3 (2012), p. 035011.

Department of Microtechnology and Nanoscience
CHALMERS UNIVERSITY OF TECHNOLOGY
Göteborg, Sweden
www.chalmers.se